The Dissertation Committee for Shutao Qiao certifies that this is the approved version of the following dissertation:

Fluid-Induced Large Deformation at Soft Material Interfaces with Blisters and Craters

Committee:

Nanshu Lu, Supervisor

Gregory J. Rodin

Kenneth M. Liechti

Rui Huang

Roger T. Bonnecaze

Fluid-Induced Large Deformation at Soft Material Interfaces with Blisters and Craters

by

Shutao Qiao

Dissertation

Presented to the Faculty of the Graduate School of
The University of Texas at Austin
in Partial Fulfillment
of the Requirements
for the Degree of

Doctor of Philosophy

The University of Texas at Austin
May 2018

Dedicated to my parents and my wife.

Acknowledgements

Many thanks are owed to a lot of people for the completion of this dissertation. Foremost, I would like to express my gratitude to my advisor, Dr. Nanshu Lu, whose helpful guidance and supports lead me to where I stand today. Dr. Lu's enthusiasm about the unknown world and unshakable faith to make the world better inspired me since I joined her group. This work would be impossible without her inspiration and mentorship.

I would like to thank Professors Gregory J. Rodin, Kenneth M. Liechti, Rui Huang and Roger T. Bonnecaze for serving on my dissertation committee and raising questions in my proposal that make the present work better. Thank you all for suggesting perspective ideas on this work. Special thanks go to Prof. Rodin who offered countless help to my research. Thank you for your patience with my ignorance. I thoroughly enjoy the time you taught me how to be a good writer. My sincere thanks to Dr. David Henann from Brown University and Dr. Anand Jagota from Leigh University, who kindly shared their original codes.

I appreciate the opportunities to take classes from Dr. Gregory J. Rodin, Dr. Mark E. Mear, Dr. Leszek F. Demkowicz, Dr. Kenneth M. Liechti, Dr. Rui Huang, Dr. Stelios Kyriakides, Dr. Chad M. Landis and Dr. Clint Dawson. Their vast knowledge in and devotion to their own fields set good examples for me on how to be an excellent researcher.

During my time as a member of Dr. Lu's group, I witness the growth of this group and am honored to work with the group members. This group is young but full of talented, kind and selfless researchers who endeavor to scientific excellence. The cultural diversity, as well as the unique academic environment in this group made my Ph.D. life a fantastic experience.

I want to thank all my friends in Austin, in particular, Dr. Shixuan Yang, Dr. Dongjie Jiang, Dr. Sundeep Palvadi, Dr. Zheng Wang, Dr. Shideh Kabiri Ameri, Mr. Yalin Yu, Mr. Liu Wang, Mr. Taewoo Ha, Mr. Siyi Liu, Ms. Ping Zhou and Mr. Vu Tran. I benefited a lot from discussions and debates with them. They all taught me a lot both inside and outside the lab. I appreciate their companionship and enjoy the good time we spent together.

This work is dedicated to my parents and my wife. Without their encouragement, I would never have completed this work. I want to thank them for their endless love and support. I love you all.

I cannot list all the people who have helped me in achieving what I have today. I am deeply grateful to have you all in my life.

Financial support for this dissertation from US NSF Grants CMMI-1301335, CMMI-1663551, and US NSF NASCENT ERC (1160494) is highly appreciated.

Fluid-Induced Large Deformation at Soft Material Interfaces with Blisters and Craters

Shutao Qiao, Ph.D.
The University of Texas at Austin, 2018

Supervisor: Nanshu Lu

This dissertation focuses on fluid-induced large deformation at interfaces where at least one material is soft, i.e. materials with low Young's modulus and capable of large deformation. Soft materials are finding important applications in many emerging fields such as soft electronics, soft robotics, and bio-integrated devices. Most often, soft materials have to form interfaces with other materials where fluids may present. Such interfacial fluids may affect attachment in negative or positive ways but so far, theoretical studies are rare due to the difficulties associated with large deformation and elasto-capillary effects. Regarding the dynamics of fluid flow as a sequence of static equilibrium states, it becomes sufficient to analyze problems in the context of solid mechanics. This dissertation provides nonlinear solutions to such classes of problems through two examples – interfacial blisters and craters. When a soft membrane covers a flat surface, interfacial blisters inflated by increasing amount of interfacial fluids may cause detachment between the membrane and the substrate. I formulated a nonlinear membrane theory to characterize the bulging and bulging-induced delamination process of the soft membrane. Elasto-capillary effects are considered due to their significance at small-scales. Solutions for both rigid and soft substrates are obtained. For rigid substrates, a variety of boundary conditions is modeled. In the second example, the crater problem is inspired by emerging experimental evidence that enhanced adhesion has been measured when a soft material with surface craters is pressed against a rigid surface. I established a nonlinear elasticity framework to model suction forces generated by the loading and unloading process. Both ideal gas and incompressible fluids have been considered. This framework has been validated by experiments and has been applied to optimize the design of craters. The nonlinear theoretical frameworks established in this dissertation offer methodologies to model and understand other soft material interfaces with interfacial fluids.

Table of Contents

List of Tables

List of Figures

Chapter 1 Introduction

This chapter introduces soft materials and the interfaces they form. Mechanics of such interfaces have been studied widely but when there is interfacial fluid, the fluid-solid interaction is much less understood. The goal of this dissertation is to understand the large deformation associated with interfacial fluid and how it affect attachment at the interface. The difficulty comes from the nonlinear analysis and the elasto-capillary effects.

1.1 SOFT MATERIAL INTERFACES

Soft material interfaces are interfaces where one side or both sides are made of soft matters. In recent years, soft material interfaces have drawn attentions from many researchers, and various studies are being carried out. For example, the study of interface adhesion between two soft polymers [1], and the analysis of interface instabilities of two bonded soft materials [2]. Mechanical analyses of soft material interfaces are critical as they reveal foundamental mechanicsms and provide important guidance for designing principles in soft robotics and bio-integrated electronics, e.g., bio-signal sensing [3-7], drug delivery [8, 9], human-machine interaction [10-12], and so on.

The aforementioned examples of soft material interfaces only involve flat interfaces. However, in recent studies, non-flat interfaces caused by interface fluids may play an important role. In this dissertation, we focus on two classes of fluid-induced non-flat soft material interfaces: soft blisters where both the blister layer and substrate are soft materials, and dry adhesives enabled by cratered surfaces on soft matrices. Here we'd like to introduce soft blisters and cratered surfaces through thin film electronics. It's worth noting that, as general mechanical models, the corresponding studies are not limited to thin film electronics.

Soft blisters:

Most thin film electronics are made into thin layers so that they are flexible enough to form conformal contact with target surfaces, leading to strong bonding. The intimate contact is essential as thin film electronics can only function well when appropriately attached to target surfaces. For both in-vivo and epidermal thin film devices, better adhesion also produces, lower interface impedance, higher signal-to-noise ratio [4, 13-15], and higher efficiency in heat transfer [16, 17], sweat monitoring [18, 19] and drug delivery [8]. Thin film electronics may lose contact with target surfaces when the contact is only partially conformed [15]. The film thickness is found to be a key factor determining whether conformal contact could be formed, and efforts have been made to develop models improving the conformal contact [20-23].

Thin film electronics are designed and fabricated on lifeless substrates in laboratories, and are eventually transferred to biological surfaces, e.g. skins. As the largest organ of the integumentary system, skin has complicated structure that may induce unexpected failure to the device function. In particular, sweat may get into epidermal-electronics/skin interface and initiate blisters that delaminate certain part of the device from skin. The local delamination causes impairment in bio-signal monitoring, mass/heat transferring, and also distorts the thin film device which induces deviations in strain sensing. Furthermore, blisters could propagate as the inner pressure increases, which may lead to peeling off — a complete dysfunction of the device. For in-vivo thin film devices, other body fluid, e.g. blood, would also cause similar blisters. These blisters are called body fluid induced blisters. A full understanding of body fluid induced blisters is not only useful for avoiding global dysfunction in bio-integrated thin film devices, but also essential to explore novel functionalities that make use of blisters. Due to the softness and high stretchability of thin film electronics, body fluid induced blisters could undergo significant deformation, so that geometric and material nonlinearities should be taken into account in modeling. This model is also applicable to blister tests measuring the adhesion of thin films to their substrates, where the thin film is soft and the interface adhesion is strong such that delamination may occur at large central deflection.

Cratered surfaces:

To secure the intimate contact between thin film electronics and substrates, chemical glues are applied to the film/substrate interface. However, adhesion strength provided by chemical adhesives are usually considerably strong, so that when removing the bio-integrated device, one has to damage the device, and possibly the bio-tissue, which causes user-experience degradation, breaks the device reusability, and therefore, induces extra cost.

Gecko-inspired and octopus-inspired reusable adhesives are able to stick and unstick repeatedly, and the temporary bonds formed by them can be removed without damaging or leaving any residues on the adherend, which are ideal for designing reusable thin film electronics. Compared to gecko-inspired adhesives, octopus-inspired reusable adhesives can be easily fabricated in large scale with low cost. Besides, octopus-inspired adhesives exhibit load-dependency which is intrinsically different from gecko-inspired adhesives [24]. Recently, octopus-inspired adhesives have attracted researchers due to its efficiency in manufacturing, strong and reusable adhesion, load-dependency, and robust performance in both dry and wet environment [25]. Epidermal electronics incorporated with octopus-inspired adhesives, in the form of cratered surfaces, have shown impressive reusability, and potentials in various applications [9]. However, fundamental understanding of the mechanical behavior of cratered surfaces is rather limited.

1.2 OBJECTIVES

There are two objectives for this dissertation. The first is to study the fluid-induced blisters, and predict the deflection profiles as well as delamination propagation. Without losing generality, we effectively modeled the thin elastic blister layer as a thin membrane using a nonlinear membrane theory presented in Chapter 3. The criterion of delamination propagation of fluid-induced blistering was studied to avoid global dysfunction of thin film electronics. In Chapter 4, we looked into blisters on soft substrate which is one step closer to the large scope of this problem (e.g. epidermal electronics on skins, in-vivo thin film devices on organs), and implemented a numerical approach to solve the corresponding nonlinear boundary value problem. We validated the numerical approach by comparing numerical results and experimental measurements of droplets wetting soft substrates in Chapter 5, which represents the situation that the blister layer has zero stiffness.

The second is to investigate the suction effect in cratered surfaces to help researchers design better suction-enabled reusable. In Chapters 7 and 8, we established a theoretical framework to analyze isolated craters in both ambient condition and underwater condition, obtained nonlinear solutions to preload-dependent suction forces, and validated our solutions by experiments. In Chapter 9, we explored double-chamber craters, and implemented the numerical approach developed in Chapters 7 and 8 to study the fluid exchange and suction force in double-chamber craters. The study is critical to understand the fundamental mechanics of cratered surfaces, and to optimize the design of cratered surfaces, including selection of material properties, crater shape, and preload.

Chapter 2 Background and Motivations for Blisters

This chapter discusses the background and motivations for analyzing blisters at soft materials interfaces. Taking bio-integrated electronics as an example, when they are laminated on bio-tissues such as the skin or the heart, body fluids such as sweat or blood may inject into the interface between the tissue and the electronic membrane, which may degrade the bio-electronics interface. If the soft electronic membrane starts to bulge when inflated by the interfacial fluid, the induced mechanical strain may cause failure to the electronic devices. Quantitative understandings of the evolution of the blisters is therefore crucial for failure prediction and can also help with device design.

2.1 BACKGROUND

Blisters are often undesired in applications of thin film electronics, as it induces delamination that impairs bio-signal monitoring, and mass/heat transferring, and also deflects the thin film causing deviations in strain sensing [16, 17, 26]. Further delamination propagation may lead to peeling off which terminates the functionality of the adhering device.

In general, blisters may appear under two circumstances in a bi-layer system. The first is when a film adhered is subject to an in-plane compressive strain relative to the substrate. Such a strain may result from a differential compression induced by thermal heating, or by growth, in a system where a mismatch between the film and the substrate exists. Detailed introductions can be found in the dissertation by Mei [27] and literature from Evans and Hutchinson [28], Ortiz and Gioia [29], and so on. The second is when the film adhered is pressurized locally by fluid (gas or liquid) between the film and the substrate. The study of pressure-induced blister delamination is of particular interest in applications of thin film electronics, where sweat, blood, and other body fluid could penetrate into the film/substrate interface, causing blisters. In the course of study, we name these blisters as body fluid induced blisters.

In practice, pressurized blisters are designed to measure the adhesion of thin films to their substrates, known as blister tests [30, 31]. Theoretical analyses of blister tests focus on blisters with small central deflection (small deformations), so that linear plate or membrane theories apply [32, 33]. For example, Gent and Lewandowski [34] studied initiation and subsequent delamination of thin films; Hohlfelder et al. [35] derived a membrane theory for determining the adhesion energy of an interface by measuring the blister pressure and the amount of liquid injected into the testing system; Cao [36] looked into the mixed-mode interfacial fracture of thin films and substrates. However, in applications of thin film electronics, deformation of the polymeric layer could be significant and may exceed the linear regime of the material behavior, so that geometric nonlinearity and material nonlinearity should both be taken into consideration. It is worth noting that studies with geometric nonlinearity taken into account have been carried out by researchers. For example, Jensen [37] showed the transition from plate to membrane behavior of blisters under pressure loading by using von Karman plate theory. Wagner and Vella [38], and Pascalis et al. [39] considered large deformation described by Euler elastica theory in the study of compression-induced blisters.

2.2 MOTIVATION

As body fluid induced blisters significantly distort the functionality of thin film devices in applications, a good understanding is helpful to minimize the effect of blisters, e.g. avoiding delamination propagation. Studying the behavior of blisters made of nonlinear elastic membranes is also of paramount importance in measuring adhesion between elastomeric films and substrates.

In this dissertation, we consider quasi-static blisters. The delamination propagation of blisters depends on the balance between the strain energies stored in the blister layer and the substrate, and the adhesive energy of the film/substrate interface. Due to large central deflections, the membrane energy of the film outweighs the bending energy so that we consider the thin film device as a thin membrane. A nonlinear membrane theory adopted in [40-44] is applied which takes geometric and material nonlinearities into account. We reformulate the nonlinear membrane theory to make its physical meaning more straightforward. Ferroelectricity and magnetoelasticity and can be incorporated in this theory for dielectric elastomers [43] and magnetoelastic polymers [44], respectively. In our study, as the film and substrate are both soft materials, we studied elasto-capillary effect.

Chapter 3 Blisters on Rigid Substrates

Models for blisters trapped by thin films on rigid substrates have been widely used for the calculation of adhesion energy at the film-substrate interface. Plate theory is applicable when the central deflection of the film is relatively small compared with the blister radius such that the deformation is bending dominant. However, when the thin film is made of a soft material, the blister can grow such that stretching becomes dominant and the film behavior is membrane-like. This chapter presents a membrane theory for blisters on rigid substrates. Nonlinearity in both geometry and material behavior is considered. A variety of boundary conditions is studied and includes blister-induced interfacial delamination.

3.1 ANALYTICAL METHODS

This section includes basic analytical methods used for conventional blister tests as well as a nonlinear model developed for blisters with huge deflection. Comparisons among different models will be made and followed by discussions. In all analyses, materials are treated as isotropic.

3.1.1 Simple Plate Theory

Consider an axisymmetric blister with radius r_0 and thickness t_0. Kirchhoff-Love plate theory [45] can be used to model the blister layer undergoing small central deflections. The corresponding governing equation is

$$D\nabla^2\nabla^2 u_z = \Delta p \tag{3.1}$$

where

$u_z =$ the out-of-plane deflection of the plate,

$D = Et_0^3/12(1-\nu^2)$,

$\nu =$ the Poisson's ratio,

$E =$ the Young's modulus,

$\Delta p =$ the blister pressure, and

$$\nabla^2 = \frac{d^2}{dr^2} + \frac{1}{r}\frac{d}{dr}$$

under axisymmetry. Here we focus on blisters that satisfy fully clamped boundary conditions, i.e. $u_z(r_0) = 0$, and $u_z'(r_0) = 0$. Taking symmetry at $r = 0$ into account and considering that moments at $r = 0$ are finite, one obtains

$$u_z(r) = \frac{3(1-\nu)}{32}\frac{\Delta p r_0^4}{\mu_f t_0^3}\left(1 - \frac{r^2}{r_0^2}\right)^2 \tag{3.2}$$

where μ_f is the small strain shear modulus of the material of the blister layer.

3.1.2 Moderate Plate Theory

For moderate deflections, Föppl–von Kármán plate theory [46] can be used to model the deflection profile of the blister layer, which involves the effect of membrane stresses. Different formulisms can be found through literature [46]. An example in index-notation is given as

$$\begin{cases} M_{\alpha\beta},_{\alpha\beta} + \left(N_{\alpha\beta} u_\alpha\right),_\beta + \Delta p = 0 \\ N_{\alpha\beta},_\beta = 0 \end{cases} \tag{3.3}$$

where $M_{\alpha\beta}$ are in-plane moments, $N_{\alpha\beta}$ are in-plane membrane forces, and α, β = 1, 2 represent indices of in-plane coordinates. For axisymmetric circular plates, we have

$$\begin{cases} \dfrac{d^2 M_r}{dr^2} + \dfrac{2}{r}\dfrac{dM_r}{dr} - \dfrac{1}{r}\dfrac{dM_\theta}{dr} + \dfrac{1}{r}\dfrac{d}{dr}\left(N_r r \dfrac{du_z}{dr}\right) + \Delta p = 0 \\ \dfrac{dN_r}{dr} + \dfrac{N_r - N_\theta}{r} = 0 \end{cases} \tag{3.4}$$

The following elastic constitutive behavior is used according to von Karman's assumptions

$$\begin{cases} M_r = -D(\kappa_r + \nu\kappa_\theta) \approx -D\left(\dfrac{d^2 u_z}{dr^2} + \dfrac{\nu}{r}\dfrac{du_z}{dr}\right) \\ M_\theta = -D(\kappa_\theta + \nu\kappa_r) \approx -D\left(\dfrac{1}{r}\dfrac{du_z}{dr} + \nu\dfrac{d^2 u_z}{dr^2}\right) \\ N_r = \dfrac{Et_0}{1-\nu^2}(\epsilon_r + \nu\epsilon_\theta) = \dfrac{Et_0}{1-\nu^2}\left[\dfrac{du_r}{dr} + \dfrac{1}{2}\left(\dfrac{du_z}{dr}\right)^2 + \nu\dfrac{u_r}{r}\right] \\ N_\theta = \dfrac{Et_0}{1-\nu^2}(\epsilon_\theta + \nu\epsilon_r) = \dfrac{Et_0}{1-\nu^2}\left[\dfrac{u_r}{r} + \nu\dfrac{du_r}{dr} + \dfrac{\nu}{2}\left(\dfrac{du_z}{dr}\right)^2\right] \end{cases} \tag{3.5}$$

where u_r is the radial in-plane displacement of the plate, and κ_r and κ_θ are principal curvatures of the middle plane of the blister in the radial and circumferential directions, respectively. Note, linearization of κ_r and κ_θ has been applied, i.e.

$$\kappa_r \approx \frac{d^2 u_z}{dr^2}, \kappa_\theta \approx \frac{1}{r}\frac{du_z}{dr} \tag{3.6}$$

Substituting Eq. (3.5) into Eq. (3.4), one obtains von Karman equations in terms of displacements [46] as presented below

$$\begin{cases} \dfrac{d^3u_z}{dr^3}+\dfrac{1}{r}\dfrac{d^2u_z}{dr^2}-\dfrac{1}{r^2}\dfrac{du_z}{dr}=-\dfrac{12}{t_0^2}\dfrac{du_z}{dr}\left[\dfrac{du_r}{dr}+\dfrac{1}{2}\left(\dfrac{du_z}{dr}\right)^2+\nu\dfrac{u_r}{r}\right]+\dfrac{\Delta pr}{2D} \\ \dfrac{d^2u_r}{dr^2}+\dfrac{1}{r}\dfrac{du_r}{dr}-\dfrac{u_r}{r^2}=-\dfrac{1-\nu}{2r}\left(\dfrac{du_z}{dr}\right)^2-\dfrac{du_z}{dr}\dfrac{d^2u_z}{dr^2} \end{cases} \tag{3.7}$$

Here u_z still meets the same boundary conditions as in Kirchhoff-Love plate theory, i.e.

$$\frac{du_z(0)}{dr}=\frac{du_z(r_0)}{dr}=u_z(r_0)=0 \tag{3.8}$$

whereas u_r follows the following boundary conditions

$$u_r(0)=u_r(r_0)=0 \tag{3.9}$$

Note, an integration operation is applied to the moment balance equation in Eq. (3.4) to obtain Eq. (3.7). Solutions have been obtained for these equations using both analytical and numerical methods, and examples can be found in Timoshenko and Woinowsky-Krieger [46]. A perturbation method reported by Wei-Zang Chien [47] has also been widely used to asymptotically solve this nonlinear differential equation system. A shooting method was also used to numerically solve the nondimensionalized version of Eq. (3.7) [48], in which the unknown values of u_z, d^2u_z/dr^2, and du_r/dr at $r=0$ were varied until the three conditions at $r=r_0$ were satisfied with sufficient accuracy.

3.1.3 Simple Membrane Theory

When the central deflection of the blister layer is smaller than its thickness, the deformation of the blister layer is bending dominant, and plate theory is applicable. However, for a blister whose central deflection is at least several times of the film thickness, the deformation of the thin elastic film is stretching dominated, and therefore, the blister layer should be treated as a membrane [49]. In membrane theories, the blister layer does not have any flexural rigidity and can only sustain tensile loads.

Still, consider an axisymmetric blister with radius r_0 and thickness t_0. In simple membrane theory, the condition of equilibrium is

$$T\nabla^2 u_z = \Delta p \tag{3.10}$$

where T is the constant in-plane force in the membrane. For clamped blisters, the solution of Eq. (3.10) is

$$u_z(r) = h\left(1 - \frac{r^2}{r_0^2}\right) \tag{3.11}$$

and the corresponding radial displacement $u_r(r)$ is assumed to be

$$u_r(r) = c\, r\left(1 - \frac{r}{r_0}\right) \tag{3.12}$$

where h is the central deflection of the blister, and c is a constant. To determine h and c, we can apply the principal of minimum free energy, i.e.

$$\frac{\partial \Pi}{\partial h} = 0, \frac{\partial \Pi}{\partial c} = 0 \tag{3.13}$$

where

$$\Pi = U - pV \tag{3.14}$$

is the total free energy of the system, where

$$U = \frac{1}{2}\frac{Et_0}{1-\nu^2} 2\pi \int_0^{r_0} \left(\epsilon_r^2 + \epsilon_\theta^2 + 2\nu\epsilon_r\epsilon_\theta\right) r dr \tag{3.15}$$

is the strain energy stored in the blister layer, and

$$V = 2\pi \int_0^{r_0} u_z(r) r dr \tag{3.16}$$

is the volume contained by the blister. Then from Eq. (3.13), one obtains

$$u_z(r) = \left(\frac{75(1-\nu)}{16(23 + 18\nu - 3\nu^2)} \frac{\Delta p r_0}{\mu t_0}\right)^{1/3} r_0 \left(1 - \frac{r^2}{r_0^2}\right) \tag{3.17}$$

3.1.4 Moderate Membrane Theory

In von Karman plate theory, as the blister central deflection increases to a certain level, the bending energy in the blister layer becomes negligible. By setting the flexural rigidity to zero, one obtains the Föppl [50] membrane equations

$$\begin{cases} \dfrac{1}{r}\dfrac{d}{dr}\left(N_r r \dfrac{du_z}{dr}\right) + \Delta p = 0 \\ \dfrac{dN_r}{dr} + \dfrac{N_r - N_\theta}{r} = 0 \end{cases} \tag{3.18}$$

According to the second equation in Eq. (3.18), we have $d(rN_r)/dr = N_\theta$. Plugging this relation into the first equation of Eq. (3.18) yields the following

$$\begin{cases} N_r \dfrac{d^2 u_z}{dr^2} + N_\theta \dfrac{1}{r}\dfrac{du_z}{dr} + \Delta p = 0 \\ \dfrac{dN_r}{dr} + \dfrac{N_r - N_\theta}{r} = 0 \end{cases} \tag{3.19}$$

Using the elastic constitutive relation as given in Eq. (3.5) and the boundary conditions

$$u_r(0) = \frac{du_z(0)}{dr} = u_r(r_0) = u_z(r_0) = 0 \tag{3.20}$$

we can still apply the shooting method to solve for the deflection profile numerically. Though the governing equation (3.19) is achieved by omitting the bending related terms in von Karman's equations, they can also be obtained by linearizing a rigorously derived nonlinear membrane theory. The details are included in Section 3.1.5.

3.1.5 Nonlinear Membrane Theory

When the central deflection of the blister is much larger than its thickness, the membrane theory is no longer applicable. Under large stretches, the material of the blister layer exhibits nonlinear behavior, especially for elastomeric thin films. Also, the linearization of curvatures in Eq. (3.6) no longer holds. In this section, we present a nonlinear membrane theory that takes both geometric nonlinearity and nonlinear material behavior into account. This theory has been reported in [40] and was used to model highly inflated membranes made of dielectric elastomers [41-43].

Considering the undeformed configuration of the middle plane of the blister layer as $(R, 0)$, its deformed configuration can be written as $\left(r_f, z_f\right)$ (see Figure 3.1), where the subscript f represents "film" which also applies to the rest of the dissertation, and r_f and z_f are functions of R

$$r_f = r_f(R), z_f = z_f(R) \tag{3.21}$$

The strain energy density function of the material of the blister is

$$W_f = W_f(\lambda_1, \lambda_2) \tag{3.22}$$

which represents the strain energy per unit volume in the undeformed configuration. λ_1 and λ_2 are the in-plane principal stretches of the blister middle plane. Due to axisymmetry, λ_1 and λ_2 are stretches in tangential and circumferential directions of blister profile (r_f, z_f), respectively, so that it is convenient to rename them as

$$\lambda_r = \lambda_1 \text{ and } \lambda_\theta = \lambda_2.$$

Moreover, the geometric analysis provides the following relations

$$\lambda_r = \sqrt{r_f'^2 + z_f'^2}, \lambda_\theta = \frac{r_f}{R} \tag{3.23}$$

where $(\ )'$ represents d/dR.

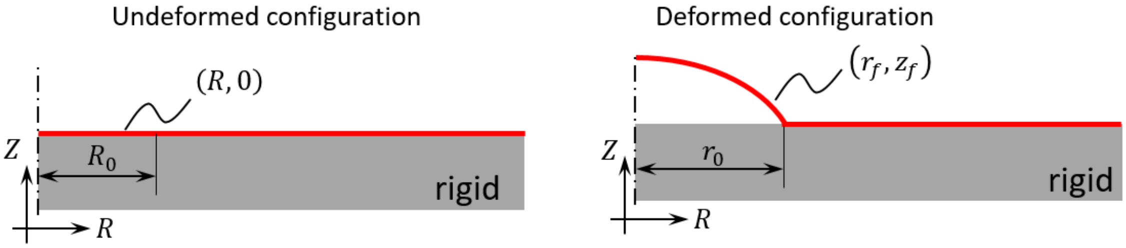

Figure 3.1 Undeformed and deformed configurations of a blister resting on a rigid substrate

For a clamped blister with radius r_0 and thickness t_0, the total free energy can be written as

$$\Pi = U_f - \Delta pV \tag{3.24}$$

where U_f is the strain energy stored in the blister layer, and V is the volume contained by it. Equations (3.25) and (3.26) give the explicit expression of U_f and V:

$$U_f = U_f\left(r_f, z_f, r_f', z_f'\right) = \int_0^{R_0} 2\pi t_0 R W_f\left(r_f, r_f', z_f'\right) dR \tag{3.25}$$

$$V = V\left(r_f, z_f, r_f', z_f'\right) = \int_0^{R_0} 2\pi r_f r_f' z_f dR \tag{3.26}$$

where R_0 is the location of the material point at the edge of the blister in undeformed configuration, i.e. $r_0 = r_f(R_0)$. When computing U_f, the bonded part of the blister layer ($R > R_0$) remains unstretched so that the strain energy over $R > R_0$ is neglected. Notice that $\Pi = \Pi\left(r_f, z_f, r_f', z_f'\right)$. One can do variation to the total free energy Π using r_f, z_f, r_f', z_f' as the variation terms. At equilibrium, the principle of minimum free energy is applied, i.e.

$$\delta\Pi = 0 \tag{3.27}$$

which leads to the corresponding Euler-Lagrangian (EL) equations

$$\begin{cases} \Delta p = -\dfrac{t_0}{r_f z_f'}\left[R\dfrac{\partial W_f}{\partial r_f} - \dfrac{\partial W_f}{\partial r_f'} - R\left(\dfrac{\partial W_f}{\partial r_f'}\right)'\right] \\ \Delta p = \dfrac{t_0}{r_f r_f'}\left[R\dfrac{\partial W_f}{\partial z_f} - \left(R\dfrac{\partial W_f}{\partial z_f'}\right)'\right] \end{cases} \tag{3.28}$$

as well as boundary conditions

$$r_f(0) = z_f'(0) = z_f(R_0) = 0, r_f(R_0) = R_0 \tag{3.29}$$

According to the relations between principal stretches and the deflection profile (Eq. (3.23)), we have

$$\frac{\partial W_f}{\partial r_f} = \frac{1}{R}\frac{\partial W_f}{\partial \lambda_\theta}, \frac{\partial W_f}{\partial r_f'} = \frac{r_f'}{\lambda_r}\frac{\partial W_f}{\partial \lambda_r}, \frac{\partial W_f}{\partial z_f} = 0, \frac{\partial W_f}{\partial z_f'} = \frac{z_f'}{\lambda_r}\frac{\partial W_f}{\partial \lambda_r^f} \tag{3.30}$$

Inserting relations from Eq. (3.30) into Eq. (3.28) yields

$$\begin{cases} \Delta p = -\dfrac{t_0}{r_f z_f'}\left[\dfrac{\partial W_f}{\partial \lambda_\theta} - \dfrac{r_f'}{\lambda_r}\dfrac{\partial W_f}{\partial \lambda_r} - R\left(\dfrac{r_f'}{\lambda_r}\right)'\dfrac{\partial W_f}{\partial \lambda_r} - R\dfrac{r_f'}{\lambda_r}\left(\dfrac{\partial W_f}{\partial \lambda_r}\right)'\right] \\ \Delta p = \dfrac{t_0}{r_f r_f'}\left[-\dfrac{\partial W_f}{\partial \lambda_r}\left(R\dfrac{z_f'}{\lambda_r}\right)' - R\dfrac{z_f'}{\lambda_r}\left(\dfrac{\partial W_f}{\partial \lambda_r}\right)'\right] \end{cases} \tag{3.31}$$

which can be reformulated into

$$\begin{cases} t_0\left(\dfrac{\kappa_r}{\lambda_\theta}\dfrac{\partial W_f}{\partial \lambda_r} + \dfrac{\kappa_\theta}{\lambda_r}\dfrac{\partial W_f}{\partial \lambda_\theta}\right) + \Delta p = 0 \\ \dfrac{r_f'}{\lambda_r}\dfrac{\partial W_f}{\partial \lambda_\theta} - \left(R\dfrac{\partial W_f}{\partial \lambda_r}\right)' = 0 \end{cases} \tag{3.32}$$

where κ_r and κ_θ are the principal curvatures of the blister profile

$$\kappa_r = \frac{r_f' z_f'' - r_f'' z_f'}{\left(r_f'^2 + z_f'^2\right)^{3/2}}, \kappa_\theta = \frac{z_f'}{r_f\left(r_f'^2 + z_f'^2\right)^{1/2}} \tag{3.33}$$

Since in-plane Cauchy stresses in the blister layer are

$$\sigma_r = \lambda_r \frac{\partial W_f}{\partial \lambda_r}, \sigma_\theta = \lambda_\theta \frac{\partial W_f}{\partial \lambda_\theta} \tag{3.34}$$

we can define in-plane membrane tractions

$$N_r = t\sigma_r = \frac{t_0}{\lambda_\theta}\frac{\partial W_f}{\partial \lambda_r}, N_\theta = t\sigma_\theta = \frac{t_0}{\lambda_r}\frac{\partial W_f}{\partial \lambda_\theta} \tag{3.35}$$

where $t = t_0/\lambda_r\lambda_\theta$ is the membrane thickness in deformed configuration considering blister layers made of incompressible materials. Substituting Eq. (3.35) into Eq. (3.32), the two equilibrium equations can be expressed as

$$\begin{cases} \kappa_r N_r + \kappa_\theta N_\theta + \Delta p = 0 \\ \dfrac{dN_r}{dR} + \dfrac{r_f'(N_r - N_\theta)}{r_f} = 0 \end{cases} \tag{3.36}$$

By applying the linearized curvatures (Eq. (3.6)) and constitutive relations (Eq. (3.5)), one can show that Eq. (3.36) recovers Föppl's membrane equations (Eq. (3.19)), which is used to model moderately deflected membranes.

Note that the governing equations in Eq. (3.36) do not depend on the choice of the material behavior, i.e. W_f. In [40-44], W_f is considered as Helmholtz free energy density function, which also contains the electrostatic energy stored in dielectric elastomers. If only strain energy is involved, with incompressible Neo-Hookean type material, the strain energy density function W_f can be expressed as

$$W_f = \frac{\mu_f}{2}(I_1 - 3) = \frac{\mu_f}{2}\left(\lambda_r^2 + \lambda_\theta^2 + \frac{1}{\lambda_r^2\lambda_\theta^2} - 3\right) \tag{3.37}$$

where I_1 is the first invariant of the unimodular component of the left Cauchy–Green deformation tensor. For incompressible Gent's material, W_f is given as

$$W_f = -\frac{\mu_f}{2}J_m \ln\left(1 - \frac{I_1 - 3}{J_m}\right) \tag{3.38}$$

where J_m is the limit of $I_1 - 3$. In Eqs. (3.37) and (3.38), μ_f is the small strain shear modulus of the material.

A shooting method was used to solve this nonlinear differential equation system. And details of the numerical method is included in Section 3.2.2.

Before moving forward to next section, it is worth to point out the difference between formulation in this sub-section and in previous studies [40-44]. In references, authors formulated the system free energy Π in terms of λ_r^f, λ_θ^f and ϕ_f, where angle ϕ_f is defined as the following

$$\sin\phi_f = -\frac{z_f'}{\sqrt{r_f'^2 + z_f'^2}} = -\frac{z_f'}{\lambda_r^f}, \cos\phi_f = -\frac{r_f'}{\sqrt{r_f'^2 + z_f'^2}} = -\frac{r_f'}{\lambda_r^f} \tag{3.39}$$

The corresponding conditions of equilibrium are

$$\begin{cases} \dfrac{d}{dR}\left(R\lambda_\theta N_r \sin\phi_f\right) = 2\Delta p \lambda_r \lambda_\theta R \cos\phi_f \\ \dfrac{d}{dR}\left(R\lambda_\theta N_r \cos\phi_f\right) - \lambda_r N_\theta = 2\Delta p \lambda_r \lambda_\theta R \sin\phi_f \end{cases} \tag{3.40}$$

It can be shown that Eqs. (3.36) and (3.40) are equivalent. However, compared to Eq. (3.40), the two equilibrium equations from Eq. (3.36) represent the force balance in normal and tangential directions, respectively, which are more physically meaningful. The reformulation in this sub-section provides a more elegant and physically meaningful expression for the boundary value problem of blisters under large stretch.

3.1.6 Results and Discussions

In the studies of blister tests, researchers mainly focus on the deflection profiles of blisters. Central deflection, volume, and pressure inside the blister are usually measured experimentally and used for further analyses. In this section, we compare the aforementioned models and make discussions. Since the clamped boundary condition in plate theory and membrane theory are intrinsically different, only membrane theories are used to serve the comparison purpose.

Pressure-volume curves and pressure-central deflection curves in different membrane theoriesFigure 3.2 plots the normalized pressure-volume relation in frames (a) and (b), and pressure-central deflection relation in frames (c) and (d). In each frame, simple membrane theory (dash-dot curves), moderate membrane theory (dashed curves), and the nonlinear membrane theory (solid curves) are used. Blister volume V is normalized by V_0 where

$$V_0 = \frac{4}{3}\pi R_0^3 \tag{3.41}$$

In the simple membrane theory and moderate membrane theory, material behavior is linear elastic with Poisson's ratio equal to 0.5, which corresponds to incompressible material. In the nonlinear membrane theory, incompressible Gent's material model is used with $J_m =$ 100, 200 and ∞. Note, $J_m \to \infty$ denotes incompressible Neo-Hookean material. Figures 3.1b and 3.1d display the portion highlighted by the red box in Figures 3.1a and 3.1c, repectively. As we can see, under small deformation, the three theories produce a similar pressure-volume relationship. However, as the blister volume increases, pressure predicted by the small and moderate membrane theories increases monotonically, while the pressure predicted by nonlinear membrane theory shows non-monotonical behavior, where N-shape pressure-volume relation can be observed. Similar deviations can also be found from the pressure-central deflection plot. From Figure 3.2, one can conclude that, when the central deflection is greater than 15% of the blister radius, the geometric and material nonlinearities become more and more significant and should not be neglected.

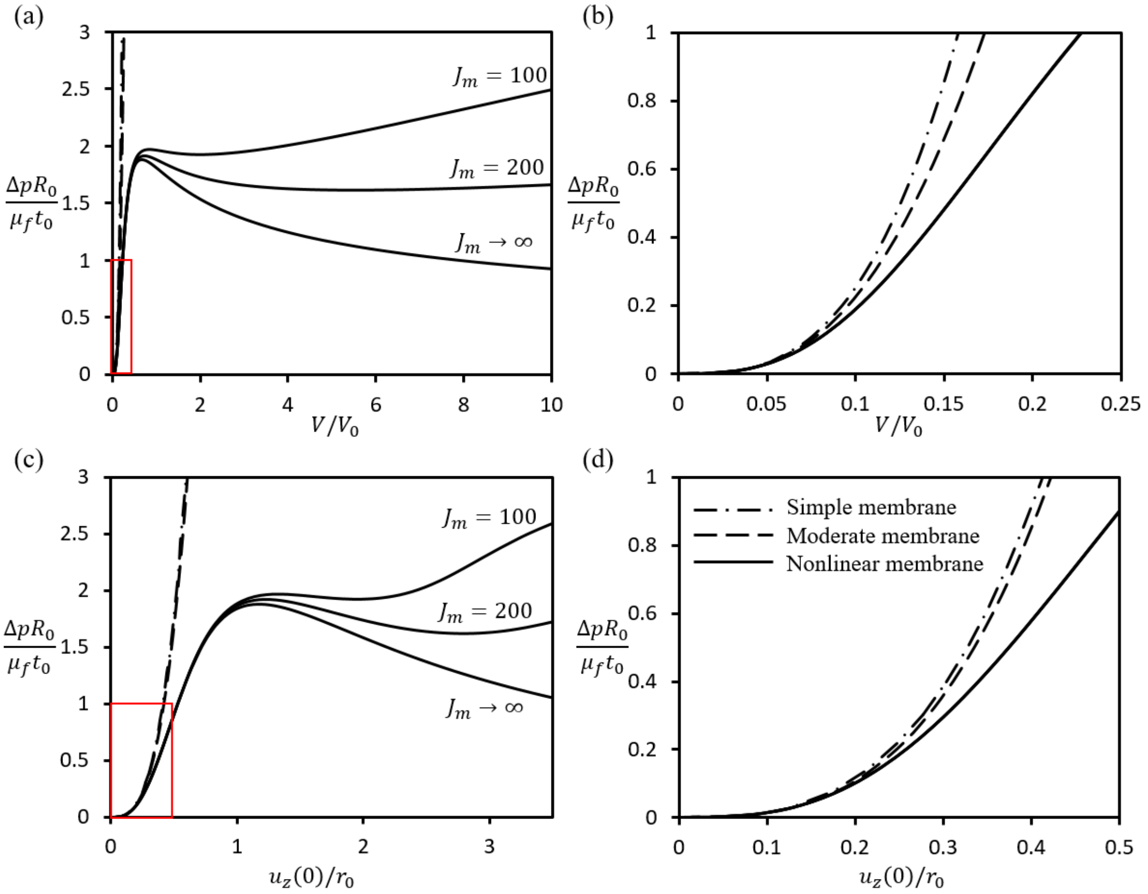

Figure 3.2 Pressure-volume curves and pressure-central deflection curves in different membrane theories

3.2 ELASTO-CAPILLARY EFFECTS

Besides the geometric and material nonlinearities discussed in Section 3.1, surface tension may also strongly affect the blister profile. For blisters made of thin membranes and filled with liquid, surface tension comes into consideration if the dimensionless elasto-capillary factor, $\gamma_l/\mu_f t_0$, is large enough, where γ_l is the surface tension exerted on the liquid/blister-layer interface.

3.2.1 Formulations of the Boundary Value Problem

If the blister with radius r_0 and initial layer thickness t_0 is filled with liquid whose surface tension is not negligible, the total free energy can be written as

$$\Pi = U_f - \Delta pV + \gamma_l A + \pi r_0^2(\gamma_{ls} - \Delta\gamma) \tag{3.42}$$

where U_f, V and Δp remain the same meaning as in Eq. (3.24), and

$\gamma_l =$ the surface energy density of the liquid/blister-layer interface,

$\gamma_{ls} =$ the surface energy density of the liquid/substrate interface,

$\Delta\gamma =$ the surface energy density of the blister-layer/substrate interface,

$A =$ the area of the liquid/blister-layer interface.

According to the definition, we have

$$\Delta\gamma = \gamma_{film} + \gamma_s - w \tag{3.43}$$

where γ_{film} is the surface energy density of the blister layer surface, γ_s is the surface energy density of the substrate surface, and w is the work of separation of the blister-layer/substrate interface. Note that when the blister is gone, γ_l recovers the surface tension of the liquid, and $w \to 0$ as well as $\gamma_{film} \to 0$ so that $\Delta\gamma \to \gamma_s$. In the following analyses, the interfacial energy densities are considered to be constant, i.e. they are independent with the deformation of the blister layer.

In this section, we do not limit ourselves to clamped blisters. Instead, we would like to look into the boundary terms obtained from the variation process, and four possible boundary conditions were extracted and discussed. To serve this purpose, instead of following Eqs. (3.25) to compute U_f, we used the following

$$U_f = \int_0^{R_0} 2\pi t_0 R W_f\left(r_f, r_f', z_f'\right) dR + \int_{R_0}^{\infty} 2\pi t_0 R W_f\left(r_f, r_f', 0\right) dR \tag{3.44}$$

In addition, we have the liquid/blister interface area written as

$$A = \int_0^{R_0} 2\pi r_f \sqrt{r_f'^2 + z_f'^2}\, dR \tag{3.45}$$

Note that the strain energy for $R > R_0$ is now taken into account in Eq. (3.44). Besides, since the substrate is flat so that $z(R) = 0$ for $R > R_0$, and therefore, the strain energy density function in the second integral of Eq. (3.44) is given as $W_f = W_f\left(r_f, r_f', 0\right)$.

Apparently, for clamped blisters, one has $r_0 = R_0$. But this may not be true for blisters that are not clamped. Note, one can also take the gravity of the liquid into consideration by simply adding the gravity potential Φ into Π, where

$$\Phi = \int_0^{R_0} \int_0^{z_f} \rho g \xi d\xi \, dA = \int_0^{R_0} \frac{1}{2} \rho g z_f^2 2\pi r_f r_f' dR \tag{3.46}$$

where ρ is the mass density of the liquid, and g is gravity acceleration. However, since the application of epidermal electronics mainly involves blisters under millimeter size, the effect of gravity can be neglected. Thus, for future formulations and discussions, gravity effect won't be included.

Following the same variation procedure and simplification in Section 3.1.5, we obtain the following equilibrium equations

$$\begin{cases} \kappa_r N_r + \kappa_\theta N_\theta + \gamma_l(\kappa_r + \kappa_\theta) + \Delta p = 0 \\ \dfrac{dN_r}{dR} + \dfrac{r_f'(N_r - N_\theta)}{r_f} = 0 \end{cases} \qquad \forall\, 0 \leq R < R_0 \tag{3.47}$$

and

$$\begin{cases} z_f = 0 \\ \dfrac{dN_r}{dR} + \dfrac{r_f'(N_r - N_\theta)}{r_f} = 0 \end{cases} \qquad \forall\, R \geq R_0 \tag{3.48}$$

The first observation is that, compared to Eq. (3.36), Eq. (3.47) has the same force balance equation in the tangential direction of the blister layer, but has extra terms in the force balance equation in the normal direction due to surface tension. Also, by removing the blister layer, i.e. $N_r = N_\theta = 0$, the second equation of (3.47) vanishes, whereas the first equation of (3.47) recovers the Laplace-Young equation [51]:

$$\gamma_l(\kappa_r + \kappa_\theta) + \Delta p = 0 \tag{3.49}$$

which governs the shape of a liquid droplet.

As to the boundary conditions, since we are using membrane theory to describe the blister layer, $r_f(R)$ and $z_f(R)$ are continuous at $R = R_0$, but $r_f'(R)$ and $z_f'(R)$ are allowed to be discontinuous at $R = R_0$. To differentiate this discontinuity, we use $f(R_0^-)$ and $f(R_0^+)$ to represent the value of $f(R_0)$ evaluated form the left and right side of R_0 [52]. According to the continuity of r_f and z_f, we have

$$\begin{aligned} &\delta R_0^- = \delta R_0^+ = \delta R_0, \\ &\delta r_f(R_0^-) = \delta r_f(R_0^+) = \delta r_0, \\ &\delta z_f(R_0^-) = \delta z_f(R_0^+) = \delta z_0 \end{aligned} \tag{3.50}$$

where z_0 is defined as $z_0 = z_f(R_0)$.

For blisters with boundary conditions different from clamped conditions, R_0 could have non zero variation, i.e. $\delta R_0 \neq 0$, such that the variation of the evaluation of a function at $R = R_0$ may be different from the evaluation of the variation of the function, i.e.

$$\delta f(R_0) \neq (\delta f)(R_0) \tag{3.51}$$

On the left-hand side of Eq. (3.51), evaluation is operated to the function $f(R)$ before variation, whereas on the right hand side, variation is firstly operated. Based on this analysis, we applied the following relations in our variation process

$$(\delta r_f)(R_0^\pm) = \delta r_f(R_0^\pm) - (r_f')\big|_{R_0^\pm}\delta R_0^\pm = \delta r_0 - (r_f')\big|_{R_0^\pm}\delta R_0, \tag{3.52}$$

$$(\delta z_f)(R_0^\pm) = \delta z_f(R_0^\pm) - (z_f')\big|_{R_0^\pm}\delta R_0^\pm = \delta z_0 - (z_f')\big|_{R_0^\pm}\delta R_0$$

Besides, regularity of r_f and z_f at $R = 0$ implies the following

$$\begin{aligned} (\delta r_f)(0) &= \delta r_f(0) - r_f'(0)\delta 0 = 0, \\ (\delta z_f)(0) &= \delta z_f(0) - z_f'(0)\delta 0 = \delta z_f(0) \end{aligned} \tag{3.53}$$

Substituting Eqs. (3.50), (3.52) and (3.53) into the boundary terms in $\delta\Pi = 0$ produces

$$\begin{aligned} &[-\cos\phi_0^- \,(N_r^- + \gamma_l) - \Delta p z_0 + (\gamma_{ls} - \Delta\gamma) + \cos\phi_0^+ \,N_r^+] r_0 \delta r_0 + \\ &[-r_0(\lambda_r^- N_r^- - \lambda_r^+ N_r^+) + R_0 t_0 (W_f^- - W_f^+)]\delta R_0 - \\ &r_0 \sin\phi_0^- \,(N_r^- + \gamma_l)\delta z_0 - [(\cos\phi_f \,N_r - \Delta\gamma) r_f \delta r_f]\big|_{R\to\infty} = 0 \end{aligned} \tag{3.54}$$

where

$$\phi_0^\pm = \phi_f(R_0^\pm), \lambda_r^\pm = \lambda_r(R_0^\pm), N_r^\pm = N_r(R_0^\pm), W_f^\pm = W_f(R_0^\pm) \tag{3.55}$$

For flat rigid substrates, one has $z_0 = \delta z_0 = 0$, and $\phi_0^+ = \pi$, such that Eq. (3.54) is further simplified into

$$\begin{aligned} &[(\gamma_{ls} - \Delta\gamma) - \cos\phi_0^- \,(N_r^- + \gamma_l) - N_r^+] r_0 \delta r_0 + \\ &[R_0 t_0 (W_f^- - W_f^+) - r_0(\lambda_r^- N_r^- - \lambda_r^+ N_r^+)]\delta R_0 - \\ &[(\cos\phi_f \,N_r - \Delta\gamma) r_f \delta r_f]\big|_{R\to\infty} = 0 \end{aligned} \tag{3.56}$$

Based on Eq. (3.56), four types of boundary conditions are extracted and are summarized.

Clamped Boundary:

For clamped boundaries (Figure 3.3a), we have $r_0 = R_0$ which are considered to be known constants, so that

$$\delta r_0 = \delta R_0 = \delta r_f\big|_{R\to\infty} = 0 \tag{3.57}$$

Thus, Eq. (3.56) is automatically satisfied. The corresponding boundary conditions for Eq. (3.47) are

$$r_f(0) = z_f'(0) = z_f(R_0) = 0, r_f(R_0) = R_0 \tag{3.58}$$

For $R > R_0$, trivial solution $r_f(R) = z_f(R) = 0$ is obtained.

Sliding Boundary:

The sliding boundary describes a blister with an initial size R_0 that does not sustain any shear force at the boundary ($R = R_0$) (Figure 3.3b). The blister boundary at R_0 could slide freely in the lateral direction. For the sake of simplicity, delaminated from the substrate at R_0 is assumed to be impossible. Then, we have

$$\delta R_0 = 0, \delta r_0 \neq 0 \tag{3.59}$$

For this case, the $R > R_0$ part is neglected so that $\left(\delta r_f\right)(\infty) = 0$, and the terms in Eq. (3.56) involving R_0^+ are set to be zero. Thus, we obtain

$$[(\gamma_{ls} - \gamma_s) - \cos\phi_0^- (N_r^- + \gamma_l)] r_0 \delta r_0 = 0 \tag{3.60}$$

and the corresponding boundary conditions of Eq. (3.47) are

$$r_f(0) = z_f'(0) = z_f(R_0) = 0, \cos\phi_0^- = -\frac{\gamma_s - \gamma_{ls}}{N_r^- + \gamma_l} \tag{3.61}$$

Note, that γ_s is used here, instead of $\Delta\gamma$, since the substrate is exposed to ambient over $R > r_0$.

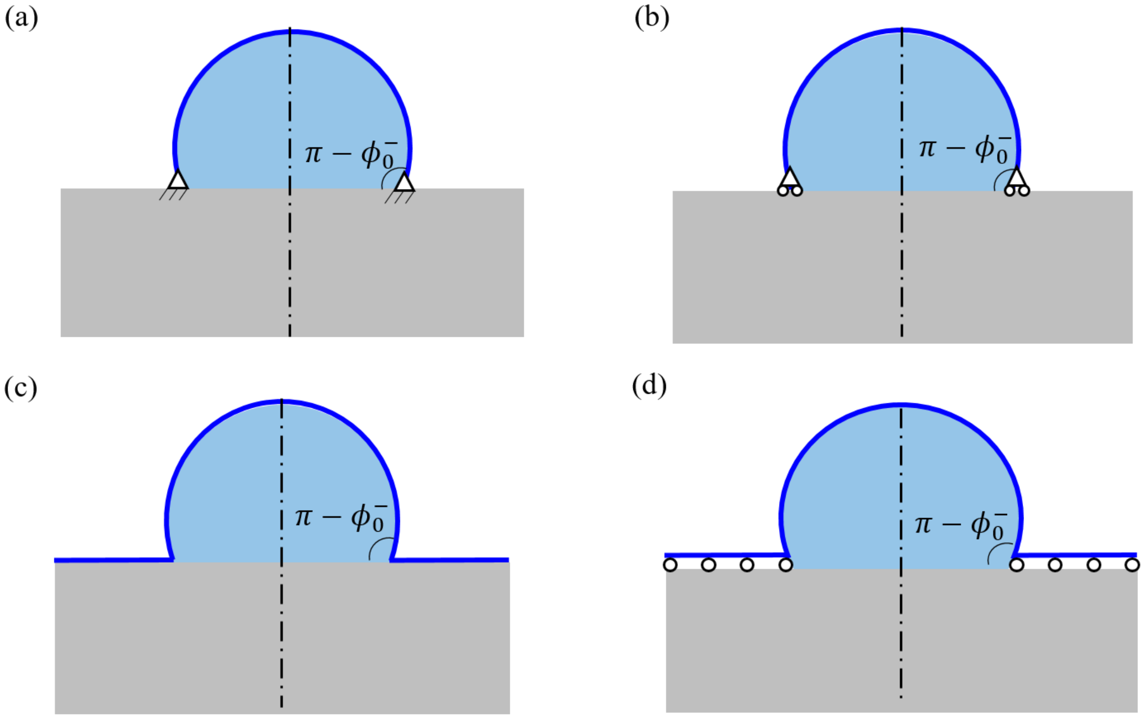

Figure 3.3 Schematics of the four different types of boundaries: (a) clamped boundary, (b) sliding boundary, (c) adhesive boundary, and (d) slippery boundary.

Adhesive Boundary:

When the blister pressure is large enough, delamination propagates into the initially bonded part. Boundaries of this type of blisters are named as adhesive boundaries (Figure 3.3c). For this case, we have $r_0 = R_0$ which are unknown once delamination propagation occurs, and

$$\delta r_0 = \delta R_0 \neq 0 \tag{3.62}$$

Note, now r_0 differs from the blister radius before delamination propagation. For the attached part, trivial solution is obtained so that all the $f(R_0^+)$ terms in Eq. (3.56) are zero. With consideration of Eq. (3.62), Eq. (3.56) could be expressed as

$$\left[(\gamma_{ls} - \Delta\gamma) - \cos\phi_0^- \,(N_r^- + \gamma_l) + t_0 W_f^- - \lambda_r^- N_r^-\right] r_0 \delta r_0 = 0 \tag{3.63}$$

In order for Eq. (3.63) to be true, when delamination propagation occurs, the corresponding boundary conditions of Eq. (3.47) are

$$r_f(0) = z_f'(0) = z_f(R_0) = 0, \cos\phi_0^- = -\frac{\Delta\gamma - \gamma_{ls} + \lambda_r^- N_r^- - t_0 W_f^-}{N_r^- + \gamma_l} \tag{3.64}$$

whereas for $R > R_0$, the trivial solution will be obtained. In addition, the extra relation $r(R_0) = R_0$ is to be used to identify the unknown location R_0. If delamination propagation does not happen, Eq. (3.64) simply decays to the clamped boundary conditions.

Slippery Boundary:

Considering a blister layer covering a wet surface, the attached part may slide in the lateral direction (Figure 3.3d), which means $r_0 \neq R_0$, and they are both unknown. For this case, one has

$$\delta r_0, \delta R_0 \neq 0 \tag{3.65}$$

According to Eq. (3.65), for governing equation (3.47), we have boundary conditions

$$r_f(0) = z_f'(0) = z_f(R_0) = 0, r_f(R_0^-) = r_0 \tag{3.66}$$

while for governing equation (3.48), we have

$$r_f(R_0^+) = r_0, N_r(\infty) = -\Delta\gamma \tag{3.67}$$

Note, if the blister layer is finite with outer radius nR_0 where $n > 1$, the boundary condition at far field should be replaced with

$$N_r(nR_0) = \gamma_s - \Delta\gamma \tag{3.68}$$

where γ_s is the surface tension of the substrate. In addition, we use

$$\cos\phi_0^- = -\frac{\Delta\gamma - \gamma_{ls} + N_r^+}{N_r^- + \gamma_l}, N_r^-\lambda_r^- - N_r^+\lambda_r^+ = t_0\frac{W_f^- - W_f^+}{\lambda_\theta^f} \tag{3.69}$$

as compatibility conditions to solve for the unknown r_0 and R_0.

It is worth noting that, for sliding, adhesive and slippery boundaries, we have conditions involving angle ϕ_0^-:

$$\boxed{\begin{array}{lr} \text{Sliding boundary: } \cos\phi_0^- = -\dfrac{\gamma_s - \gamma_{ls}}{N_r^- + \gamma_l} & (3.70) \\ \text{Adhesive boundary: } \cos\phi_0^- = -\dfrac{\Delta\gamma - \gamma_{ls} + \lambda_r^- N_r^- - t_0 W_f^-}{N_r^- + \gamma_l} & (3.71) \\ \text{Slippery Boundary: } \cos\phi_0^- = -\dfrac{\Delta\gamma - \gamma_{ls} + N_r^+}{N_r^- + \gamma_l} & (3.72) \end{array}}$$

As the blister layer being removed, all the membrane-related terms go to zero and $\Delta\gamma$ recovers the surface tension of the substrate, i.e. $\Delta\gamma \rightarrow \gamma_s$. Thus, Eqs. (3.70)~(3.72) all recover the Young's equation for contact angle

$$\cos(\pi - \phi_0^-) = \frac{\gamma_s - \gamma_{ls}}{\gamma_l} \tag{3.73}$$

where $\pi - \phi_0^-$ represents the contact angle of the blister at $R = R_0^-$. Later on, when discussing the results, for the sake of simplicity, $\pi - \phi_0^-$ will be named as the contact angle of the blister which follows Eqs. (3.70)~(3.72) for each type of boundary conditions.

3.2.2 Shooting Method

According to the definition of angle ϕ_f (Eq. (3.39)), the principal curvatures, κ_r and κ_θ, can be rewritten as

$$\kappa_r = \frac{\phi_f'}{\lambda_r}, \kappa_\theta = -\frac{\sin\phi_f}{r_f} \tag{3.74}$$

The equilibrium equations now become

$$\begin{cases} N_r \dfrac{\phi_f'}{\lambda_r} - N_\theta \dfrac{\sin\phi_f}{r_f} + \gamma_l \left(\dfrac{\phi_f'}{\lambda_r} - \dfrac{\sin\phi_f}{r_f} \right) + \Delta p = 0 \\ \dfrac{\partial N_r}{\partial \lambda_r} \lambda_r' - \dfrac{\partial N_r}{\partial \lambda_\theta} \dfrac{\cos\phi_f \, \lambda_r R + r_f}{R^2} - \cos\phi_f \, \lambda_r \dfrac{N_r - N_\theta}{r_f} = 0 \end{cases} \tag{3.75}$$

or

$$\begin{cases} \phi_f' = \dfrac{(N_\theta + \gamma_l) \dfrac{\lambda_r}{\lambda_\theta} \dfrac{\sin\phi_f}{R} - \Delta p \lambda_r}{N_r + \gamma_l} \\ \lambda_r' = \dfrac{\dfrac{\cos\phi_f \, \lambda_r}{R} \left(\dfrac{\partial N_r}{\partial \lambda_\theta} + \dfrac{N_r - N_\theta}{\lambda_\theta} \right) + \dfrac{\partial N_r}{\partial \lambda_\theta} \dfrac{\lambda_\theta}{R}}{\dfrac{\partial N_r}{\partial \lambda_r}} \end{cases} \tag{3.76}$$

where N_r, N_θ are algebraic functions of λ_r and λ_θ, and r_f' has been replaced with $-\cos\phi_f \, \lambda_r$. If we use incompressible Gent's material law for the blister layer material, we have the in-plane membrane tractions expressed as

$$\begin{aligned} N_r &= \frac{-\mu_f t_0 J_m \left(\lambda_r^4 \lambda_\theta^2 - 1 \right)}{\lambda_r \lambda_\theta + \lambda_r^3 \lambda_\theta^3 \left(\lambda_r^2 + \lambda_\theta^2 - 3 - J_m \right)} \\ N_\theta &= \frac{-\mu_f t_0 J_m (\lambda_r^2 \lambda_\theta^4 - 1)}{\lambda_r \lambda_\theta + \lambda_r^3 \lambda_\theta^3 (\lambda_r^2 + \lambda_\theta^2 - 3 - J_m)} \end{aligned} \tag{3.77}$$

Now a shooting method can be constructed using $r_f(R)$, $z_f(R)$, $\phi_f(R)$ and $\lambda_r(R)$. The corresponding initial problem is given as the following

$$\begin{cases} \dfrac{d}{d\hat{R}} y_1 = -\dfrac{y_4 \cos y_3 + y_1}{\hat{R}} \\ \dfrac{d}{d\hat{R}} y_2 = -y_4 \sin y_3 \\ \dfrac{d}{d\hat{R}} y_3 = \dfrac{y_4 [y_4^2 y_1^4 - 1 + \alpha y_4^3 y_1^3 \delta] \dfrac{\sin\phi}{\hat{R}} - \beta y_4^4 y_1^4 \delta}{y_1 [y_4^4 y_1^2 - 1 + \alpha y_4^3 y_1^3 \delta]} \\ \dfrac{d}{d\hat{R}} y_4 = -\delta \dfrac{y_4^2 (y_4^2 y_1^4 - 3) \cos\phi + y_4 y_1 (y_4^4 y_1^2 - 3)}{\hat{R} y_1 \left[(y_4^4 y_1^2 + 3)\delta + \dfrac{2(y_4^4 y_1^2 - 1)^2}{J_m y_4^2 y_1^2} \right]} \\ \qquad + \dfrac{2 y_4 (y_4^6 y_1^6 - y_4^2 y_1^2 I_1 + 2)(y_4 \cos\phi + y_1)}{\hat{R} y_1 [y_4^2 y_1^2 (y_4^4 y_1^2 + 3) J_m \delta + 2(y_4^4 y_1^2 - 1)^2]} \end{cases} \tag{3.78}$$

where

$$\delta = 1 - \frac{I_1 - 3}{J_m} \tag{3.79}$$

$$\hat{R} = \frac{R}{R_0}, y_1 = \lambda_\theta, y_2 = \frac{z_f}{R_0}, y_3 = \phi_f, y_4 = \lambda_r \tag{3.80}$$

and

$$\alpha = \frac{\gamma_l}{\mu_f t_0}, \beta = \frac{\Delta p R_0}{\mu_f t_0} \tag{3.81}$$

According to the initial conditions summarized in Section 3.2.1, the initial conditions at $\hat{R} = 0$ are

$$y_1(0) = k, y_2(0) = 0, y_3(0) = \pi \text{ and } y_4(0) = k \tag{3.82}$$

where k is varied until boundary conditions at $\hat{R} = 1$ are satisfied. However, this initial condition produces zero Jacobian from the first increment. Due to this numerical difficulties at $\hat{R} = 0$, the solution procedure began at a small value, i.e. $\hat{R} = dR \ll 1$, so that the initial conditions are reformulated as:

$$\begin{gathered} y_1(dR) = k, y_2(dR) = 0, \\ y_3 = \pi - \frac{\beta k^7 g(k)}{2[k^6 - 1 + \alpha k^6 g(k)]} dR, y_4 = k \end{gathered} \tag{3.83}$$

where

$$g(k) = 1 - \frac{2k^6 - 3k^4 + 1}{J_m k^4} \tag{3.84}$$

The numerical solver is coded in Matlab using $dR = 0.00001$ which is resulted from a basic convergence study.

Particular attention should be paid to adhesive boundaries and slippery boundaries. For adhesive boundaries, once delamination propagates, R_0 changes and differs from the previous R_0. To differentiate these two R_0's, we keep the notation R_0 for the blister size before delamination propagation and use R_1 to denote the blister size after delamination propagation. In the corresponding shooting method, same y_i's would be used, but we will be varying both k and R_1/R_0 until

$$\cos\phi_0^- = -\frac{\Delta\gamma - \gamma_{ls} + \lambda_r^- N_r^- - t_0 W_f^-}{N_r^- + \gamma_l} \text{ and } r_f(R_1) = R_1 \tag{3.85}$$

are satisfied. For slippery boundaries, we vary three parameters, k, r_1/R_0 and R_1/R_0, until all the other boundary conditions are satisfied.

3.2.3 Results and Discussions

As aforementioned in Section 3.1.6, central deflection, volume, and pressure inside the blister are usually measured experimentally and used for further analyses. In this section, we looked into the effect of surface tension on the relationships among the central deflection, volume, pressure of the blister. In addition, we also studied the “contact angle”, i.e. $\pi - \phi_0^-$, of the blister, which is another experimentally measurable parameter.

In extreme case $\mu_f t_0 \to 0$, the blister recovers a liquid droplet, so that numerical solutions of Eq. (3.47) should satisfy the Young’s equations of Laplace pressure (Eq. (3.49)) and contact angle (Eq. (3.73)). Taking axisymmetry into account, Eq. (3.49) can be solved analytically. The corresponding profile of a droplet is a spherical shape. Thus, one obtains the following relations for a droplet

$$\begin{cases} \dfrac{\Delta p R_0}{\gamma_l} = 2\sin\phi_0^- \\ \dfrac{z_f(0)}{R_0} = \dfrac{1+\cos\phi_0^-}{\sin\phi_0^-} \\ \dfrac{V}{V_0} = \dfrac{(1+\cos\phi_0^-)^2(2-\cos\phi_0^-)}{4\sin\phi_0^-} \end{cases} \tag{3.86}$$

where $z_f(0)/R_0$ is the normalized central deflection that will be referred as the aspect ratio of the blister. Using the shooting method prescribed in Section 3.2.2, we numerically obtained $\Delta p R_0/\gamma_l$, volume, aspect ratio and contact angle of the blister when $\mu_f t_0 \to 0$. The corresponding analytical and numerical results are plotted in Figure 3.4 as black dashed curves and red solid curves, respectively. The coincidence between results using analytical and numerical methods validates our numerical code, and thus, it can be applied to more general situations, e.g. $\mu_f t_0 \neq 0$.

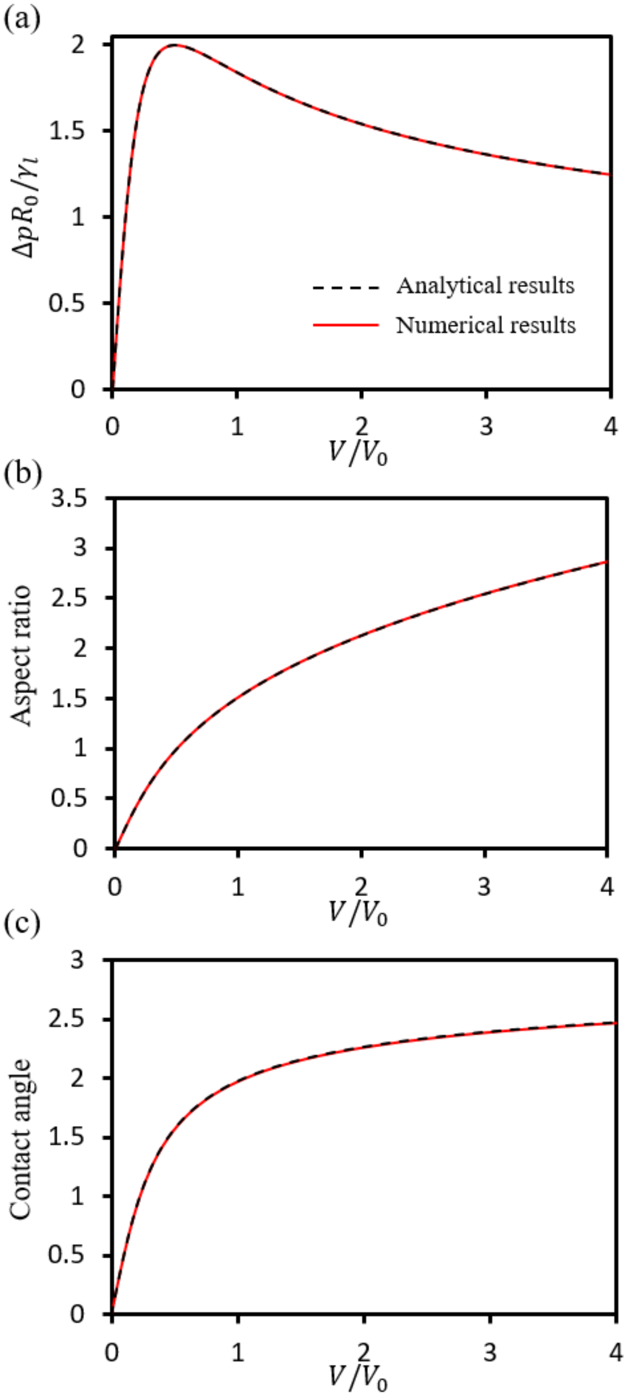

Figure 3.4 Comparisons between analytical results and numerical results on (a) pressure-volume, (b) aspect ratio-volume, and (c) contact angle-volume relations

Clamped Boundary:

Figure 3.5 shows the computed (a) pressure-volume, (b) aspect ratio-volume, and (c) contact angle-volume relations at α =0.0, 0.5, 1.0 and 2.0. For comparison purpose, the material behavior of the blister layer is modeled as incompressible Gent's material (dashed curves) using $J_m = 100$, and incompressible Neo-Hookean material (solid curves).

According to Figure 3.5a, when surface tension is taken into consideration, blisters with higher surface tension (large α) require stronger pressurization exerted on the blister layer in order to achieve the same blister volume. At small blister volume, i.e. $V/V_0 < 1$, pressure-volume relations modeled with both material laws almost coincide with each other, which means the material law does not affect blister behavior at small deformation. However, at large blister volume, i.e. $V/V_0 > 1$, the two models produce significantly deviated pressure. Eventually, N-shape pressure-volume relation is achieved in Gent's blister, while the pressure in the Neo-Hookean blister first increases then decreases along with the growth of blister volume. The difference is due to the strengthen effect in Gent's material as $I_1 - 3 \rightarrow J_m$.

In experiments, the aspect ratio and the contact angle of a blister can be easily measured using imaging techniques. However, Figures 3.4b and 3.4c show that, for Neo-Hookean blisters, the blister aspect ratio and the contact angle are nearly independent with α. Thus, in blister tests on Neo-Hookean thin films (i.e. weak strengthening effect), if the blister layer does not further delaminate from the substrate, one cannot effectively extract the value of α based on measured aspect ratio (i.e. central deflection), contact angle and blister volume. However, for Gent's blister layer, as the material strengthens at large V/V_0, blisters with smaller α show smaller aspect ratio and larger contact angle, and thus the measured aspect ratio and contact angle can be used to differentiate blister systems with different α. Besides, compared to Neo-Hookean blisters, Gent's blisters in general have flatter profiles, as shown in Figure 3.6.

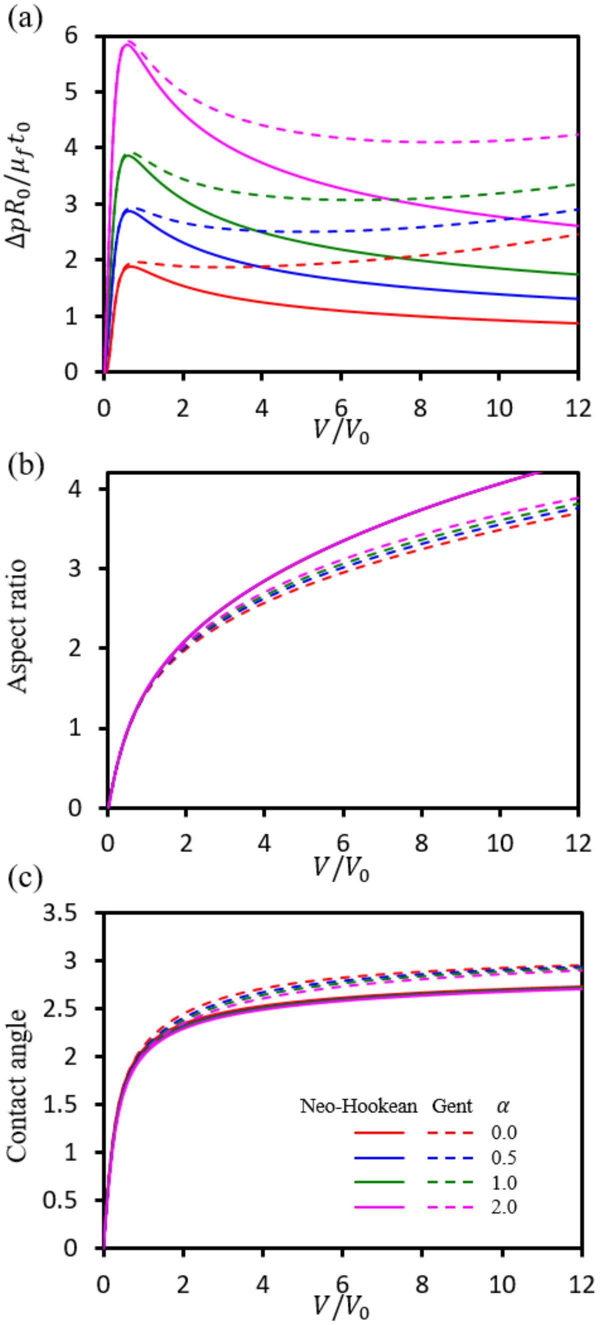

Figure 3.5 Computed (a) pressure-volume, (b) aspect ratio-volume, and (c) contact angle-volume relations at α = 0.0, 0.5, 1.0 and 2.0

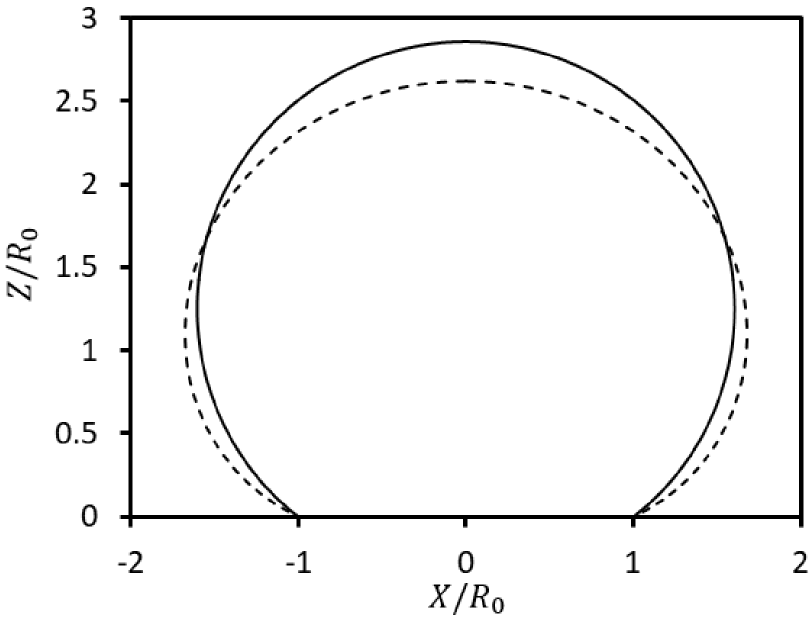

Figure 3.6 Side view of deformed profiles of clamped blisters at $V/V_0 = 4$. The solid and dashed curves correspond to blister layers modeled as incompressible Neo-Hookean material and Gent's material with $J_m = 100$, respectively

Sliding Boundary:

Sliding boundary does not apply to real applications. However, interesting phenomena can be observed from blisters with sliding boundaries. In this sub-section, we focus on incompressible Neo-Hookean blister layers only.

Numerical results of pressure-volume, aspect ratio-volume, and contact angle-volume relations at α =0.0, 0.5, 1.0, 2.0 and 5.0 are plotted in Figure 3.7. And to obtain results in Figure 3.7, one also needs to specify the value of $(\gamma_s - \gamma_{ls})/\gamma_l$, which corresponds to the Young's contact angle between the liquid and the substrate. In Figure 3.7, we used

$$\phi_Y = \frac{3\pi}{4} \tag{3.87}$$

where $\phi_Y = \mathrm{acos}((\gamma_s - \gamma_{ls})/\gamma_l)$.

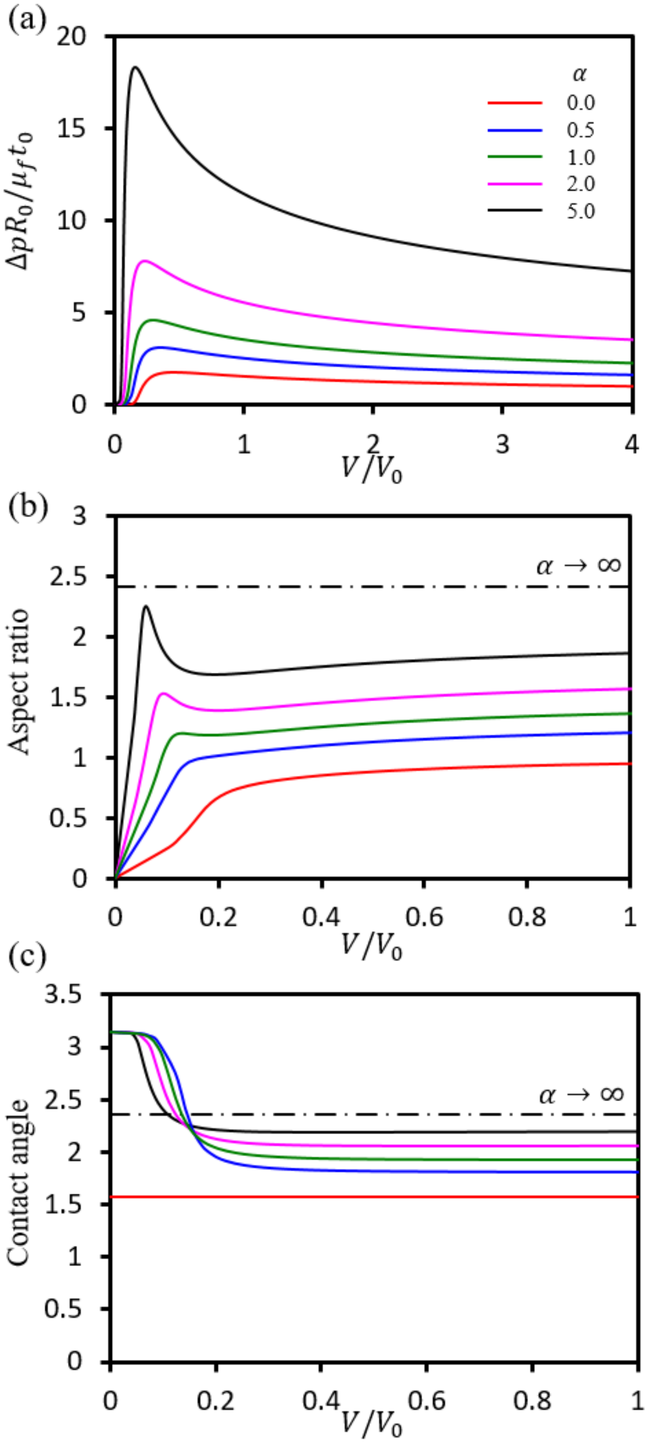

Figure 3.7 Numerical results of (a) pressure-volume, (b) aspect ratio-volume, and (c) contact angle-volume relations for α = 0.0, 0.5, 1.0, 2.0 and 5.0.

The pressure-volume relation of sliding boundary is similar with that of the clamped boundary. However, the blister aspect ratio and contact angle show different behaviors. According to Figure 3.7b and c, as the blister volume grows, the blister aspect ratio and contact angle both reach to plateaus. When α approaches to 0, the corresponding values of the plateaus are close to 1 for blister aspect ratio, and to $\pi/2$ for blister contact angle. This behavior indicates that the blister profile becomes more and more similar to hemispherical shape as $\alpha \rightarrow 0$ at large V/V_0. When $\alpha \rightarrow \infty$, the blister simply decays to a droplet so that the blister aspect ratio and contact angle are $1+\sqrt{2}/2$ and $3\pi/4$, respectively (see dashed-dotted curves in Figure 3.7).

Figure 3.8 plots blister aspect ratio and contact angle only, but different ϕ_Y's are considered. The black curve in Figure 3.8a denotes the aspect ratio-volume relation at $\alpha = 0$. In Figure 3.8a, as $\alpha \rightarrow 0$, all curves collapse to the black curve regardless to ϕ_Y. In Figure 3.8b, for $\phi_Y = \pi/2$, the blister contact angle is always $\pi/2$ and all the corresponding contact angle-volume curves at different α's coincide. Besides, at large V/V_0, for $\phi_Y = \pi/4$ and $\pi/2$, we also observe the similar trend for $\phi_Y = 3\pi/4$: as $\alpha \rightarrow 0$, plateaus value of blister aspect ratio approach to 1, and blister contact angles approach to $\pi/2$. This observation means that, regardless to the type of liquid filled in the blister, adding the blister layer always tends to change the liquid profile into a shape that's closer to a hemisphere, especially at large V/V_0. An intuitive explanation is that, at the contact line formed by the blister layer, the substrate, and the liquid, the tensile membrane force N_r leads to an equilibrium configuration so that the blister contact angle, $\pi - \phi_0^-$ is closer to $\pi/2$ compared to ϕ_Y. As shown in Figure 3.9, for $\phi_Y < \pi/2$ (Figure 3.9a), by adding the membrane force N_r, in order to achieve equilibrium, the tranction $N_r + \gamma_l$ rotates counterclockwise which ends up with incense in contact angle; for $\phi_Y > \pi/2$

(Figure 3.9b), $N_r + \gamma_l$ rotates clockwise to maintain equilibrium, which leads to decrese in contact angle.

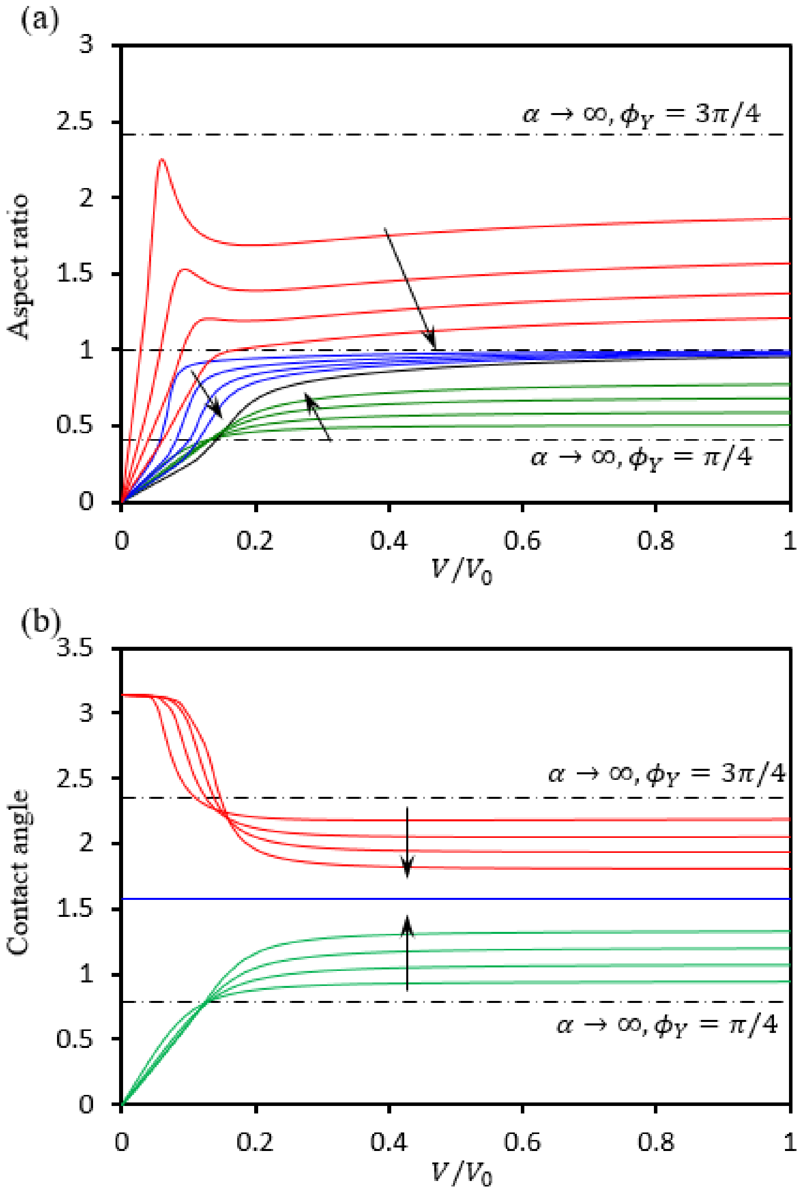

Figure 3.8 Computed (a) aspect ratio-volume, and (b) contact angle-volume curves at $\phi_Y = \pi/4$ (green), $\pi/2$ (blue) and $3\pi/4$ (red). Along the arrows, α deacreases from ∞ to 0: $\alpha = \infty$, 5.0, 2.0, 1.0, 0.5, and 0.0.

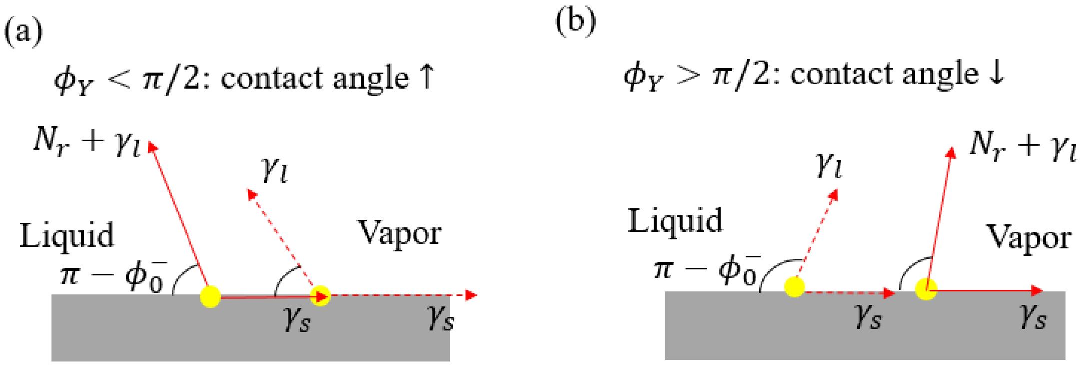

Figure 3.9 Schematics for equilibrium configuration at contact line (yellow dots) with (red solid arrows) and without (red dashed arrows) the blister layer for (a) $\phi_Y < \pi/2$, and (b) $\phi_Y > \pi/2$

Another interesting observation is that, at small V/V_0, when surface tension is taken into account, instead of bulging out, the blister layer simply wraps around the liquid between the blister layer and substrate, as shown in Figure 3.10. Due to the effect of surface tension, the blister layer wrapping around the liquid produces higher strain energy but lower surface energy. And the increase in strain energy is overwhelmed by the decrease in surface energy so that a lower free energy is achieved at the end. This phenomenon is named as elasto-capillary wrapping, and has been reported and well-studied in many literatures [53-55]. A series of pictures taken by Antkowiak et al [56] is shown in Figure 3.11 in which an elasto-capillary wrapping phenomenon can be observed.

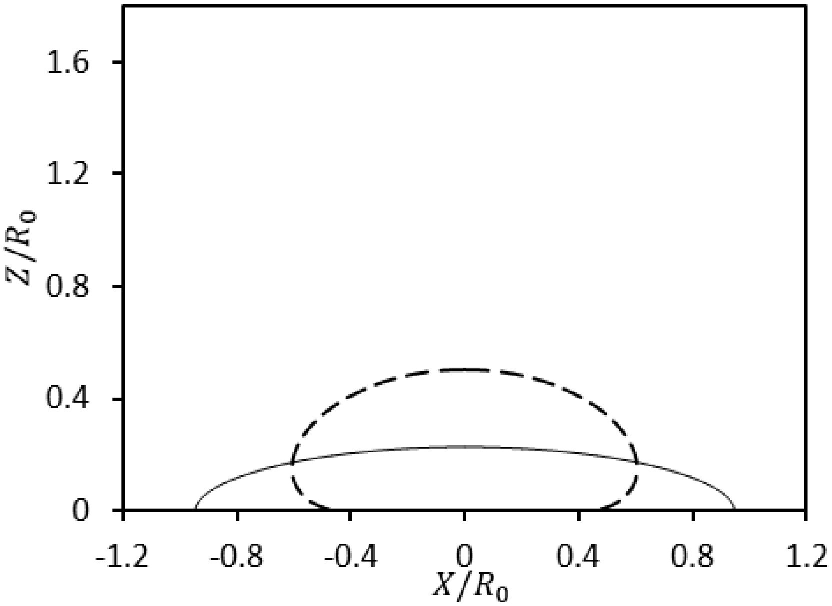

Figure 3.10 Side views of deformed profiles of blisters with sliding boundaries at $V/V_0 = 0.1$. The solid and dashed curves correspond to blister layers modeled as incompressible Neo-Hookean material with $\alpha = 0$ and $\alpha = 1$, respectively

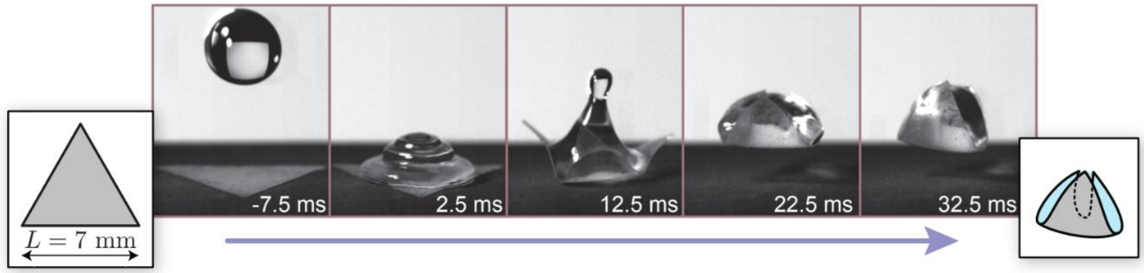

Figure 3.11 Instant capillary origami, obtained with a water droplet of radius R = 1.55 mm impacting a thin triangular polymer sheet with thickness h = 55 µm at velocity 0.53 m/s (adopted with permission from Ref. [56], Copyright (2011) National Academy of Sciences)

Adhesive Boundary:

Consider a blister layer with adhesive boundary whose initial delamination size is R_0. Before delamination propagation, the blister layer behaves the same with a blister clamped at $R = R_0$. As V/V_0 increases in a volume-controlled blister test, delamination propagation may occur when Eq. (3.71) is met. Whether the delaminated zone grows or not depends on how the system free energy acts. If delamination propagation brings the system to a configuration that has lower free energy compared to the configuration that delamination size maintains, then the blister tends to be delaminated from the substrate.

Figure 3.12 shows side views of computed blister profiles at $V/V_0 = 3$. The blister layer is modeled as incompressible Gent material with $J_m = 100$. Other dimensionless parameters, α and $(\gamma_{ls} - \Delta\gamma)/\mu_f t_0$, are set to be 0.5 and 2.5, respectively. If delamination zone does not grow, we treat the boundary as clamped boundary at $R = R_0$ and the dashed curve was obtained. If delamination zone grows from R_0 to R_1, at equilibrium, we solve for the blister profile using boundary conditions given in Eq. (3.64). Note, since we use R_1 to denote the size of delamination zone, r_0 and R_0 in Eq. (3.64) should be replaced with r_1 and R_1, respectively, where r_1 is defined as $r_1 = r(R_1)$. The extra unknown R_1 can be obtained using the relation $r_1 = R_1$. By doing so, we numerically obtained the solid curve in Figure 3.12. The blue segment represents the part of the blister layer that's initially delaminated from the substrate, while the red segment is initially bonded to the substrate. The total free energy of the system, Π, can be calculated following the definition in Eq. (3.42). In Figure 3.12, the normalized free energy, $\Pi/(\pi R_0^2 \mu_f t_0)$, was found to be 13.4 and 29.4 for configurations with and without delamination propagation, respectively. Thus, for this case, delamination propagation is preferred since it produces lower free energy.

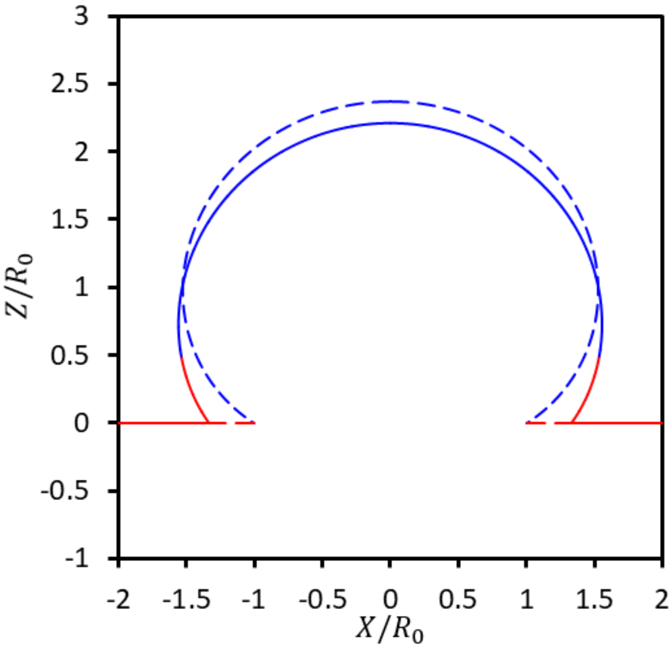

Figure 3.12 Side views of blister profiles at $V/V_0 = 3$ with $\alpha = 0.5$, and $(\gamma_{ls} - \Delta\gamma)/\mu_f t_0 = 2.5$. Dashed and solid curves are obtained using clamped and adhesive boundary conditions, respectively. For both configurations, blue part of the curve represents the blister layer that's initially delaminated from the substrate, whereas the red part is initially bonded to the substrate

With the same parameters used in Figure 3.12, Figure 3.13 is generated which plots the normalized pressure-volume and free energy-volume relations. In Figure 3.13, red curves represent configurations with delamination propagation, while black curves are without delamination propagation. The intersected point (blue markers) of results from the two sets of configurations corresponds to the critical blister volume $V_c = 1.27V_0$ at which delamination starts to propagate. According to Figure 3.13b, delamination propagation leads to higher free energy when $V < V_c$, whereas it lowers the system free energy when $V > V_c$. Thus, delamination propagation is always preferred for $V > V_c$. As a result, in Figure 3.13a, the real pressure-volume relation follows the black curve for $V < V_c$, and the red curve for $V > V_c$.

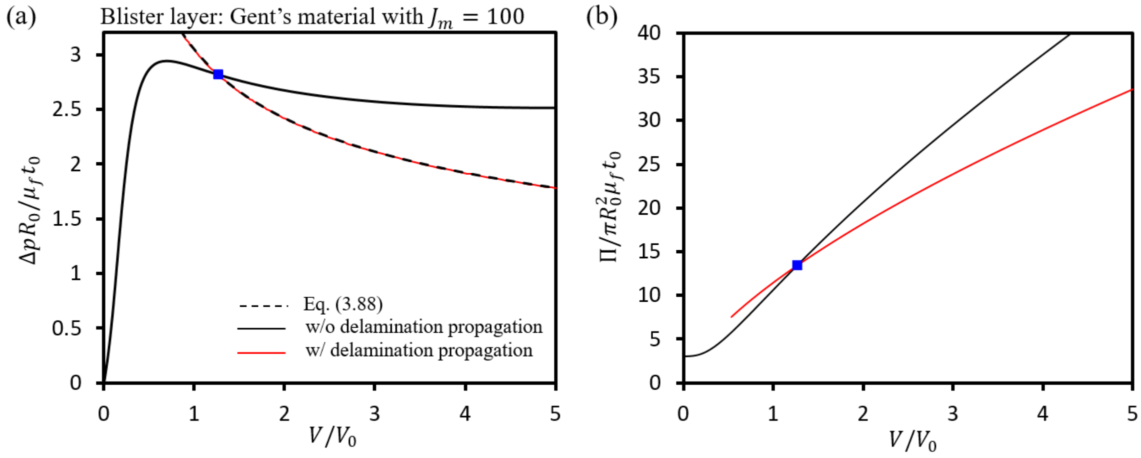

Figure 3.13 Computed (a) pressure-volume and (b) free energy-volume relations. Red curves represent configurations with delamination propagation, while black curves are without delamination propagation.

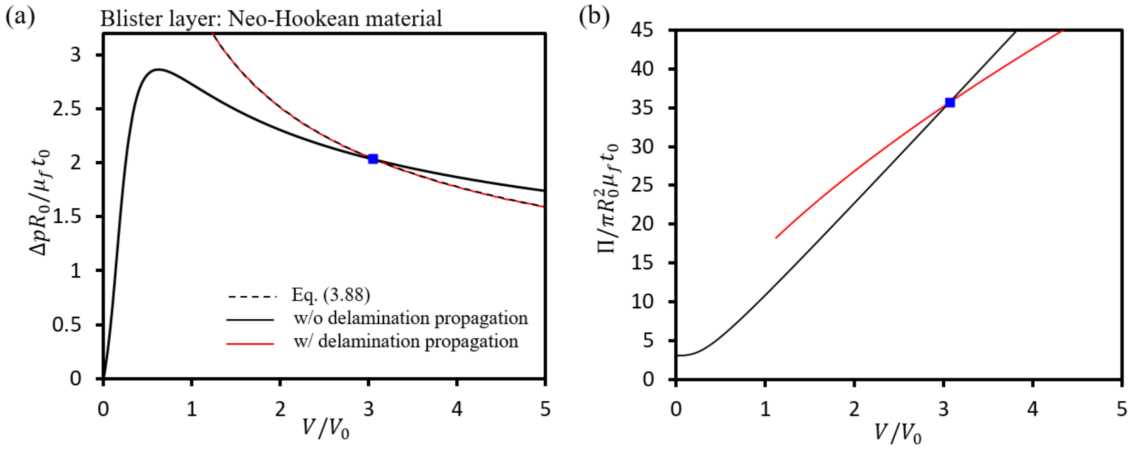

Figure 3.14 Computed (a) pressure-volume and (b) free energy-volume relations. Red curves represent configurations with delamination propagation, while black curves are without delamination propagation.

Similar with Figure 3.13, Figure 3.14 can be obtained using incompressible Neo-Hookean material law. The corresponding critical volume V_c was found to be $3.06V_0$ which is larger than that of the blister layer governed by Gent material law. This difference is induced by the strengthening effect in Gent material at larger stretch, which allows the blister layer sustain higher membrane traction, N_r, at large deformation. Thus, as a driving force, the membrane traction N_r at $R = R_0^-$ peels the blister layer off substrate and leads to delamination propagation. However, Neo-Hookean material does not strengthen so that the membrane traction N_r can only peel the bonded blister layer off at larger contact angle, i.e. larger critical volume V_c.

Based on dimensional analysis, we found that once delamination propagation sets in, dimensionless parameters V/V_1, $\Delta p R_1/\mu_f t_0$, $z(0)/R_1$ (i.e. blister aspect ratio), and $\pi - \phi_0^-$ (i.e. blister contact angle) only depends on α (i.e. $\gamma_l/\mu_f t_0$) and $(\gamma_{ls} - \Delta\gamma)/\mu_f t_0$, where $V_1 = 4\pi R_1^3/3$. Thus, when delamination propagates, the pressure-volume relation of the blister can also be written as

$$V\left(\frac{\Delta p}{\mu_f t_0}\right)^3 = const \tag{3.88}$$

where the value of the constant is determined by the critical values, V_c and Δp_c, at which the blister starts to further delaminate. The pressure-volume relation following Eq. (3.88) were also plotted in Figures 3.13a and 3.14a as dashed black curves which overlap with the numerical results. Furthermore, once delamination propagation sets in, the corresponding V/V_1, $\Delta p R_1/\mu_f t_0$, blister aspect ratio, and blister contact angle can be plotted as contour plots in $\gamma_l/\mu_f t_0 \sim (\gamma_{ls} - \Delta\gamma)/\mu_f t_0$ parametric space, as shown in Figures 3.15 and 3.16, where the blister layer is modeled as incompressible Gent and Neo-Hookean material, respectively. In each frame of Figures 3.15 and 3.16, the left border corresponds to the extreme situation that $V \rightarrow 0$, which ends up with

$$\gamma_l = \Delta\gamma - \gamma_{ls} \tag{3.89}$$

For large $(\gamma_{ls} - \Delta\gamma)/\mu_f t_0$, under certain level of $\gamma_l/\mu t_0$, there is no solution for Neo-Hookean blister layer (labeled blank area in Figure 3.16) when applying adhesive boundary conditions. It means, for these blisters, the membrane/substrate interface is bonded so well, such that, no matter what pressurization is applied, blisters would only grow into bigger shapes before break, and the initial delamination never grows. For blister layers modeled as Gent material, due to the strengthening effect, delamination propagation always occur at certain V_c. Thus, in blistering tests aiming for measurement of the adhesive strength of thin-film/substrate interface, if the blister layer material does not strengthen significantly (e.g. Neo-Hookean material), one should choose membranes thickness so that the combination of $\gamma_l/\mu_f t_0$ and $(\gamma_{ls} - \Delta\gamma)/\mu_f t_0$ does yields delamination propagation.

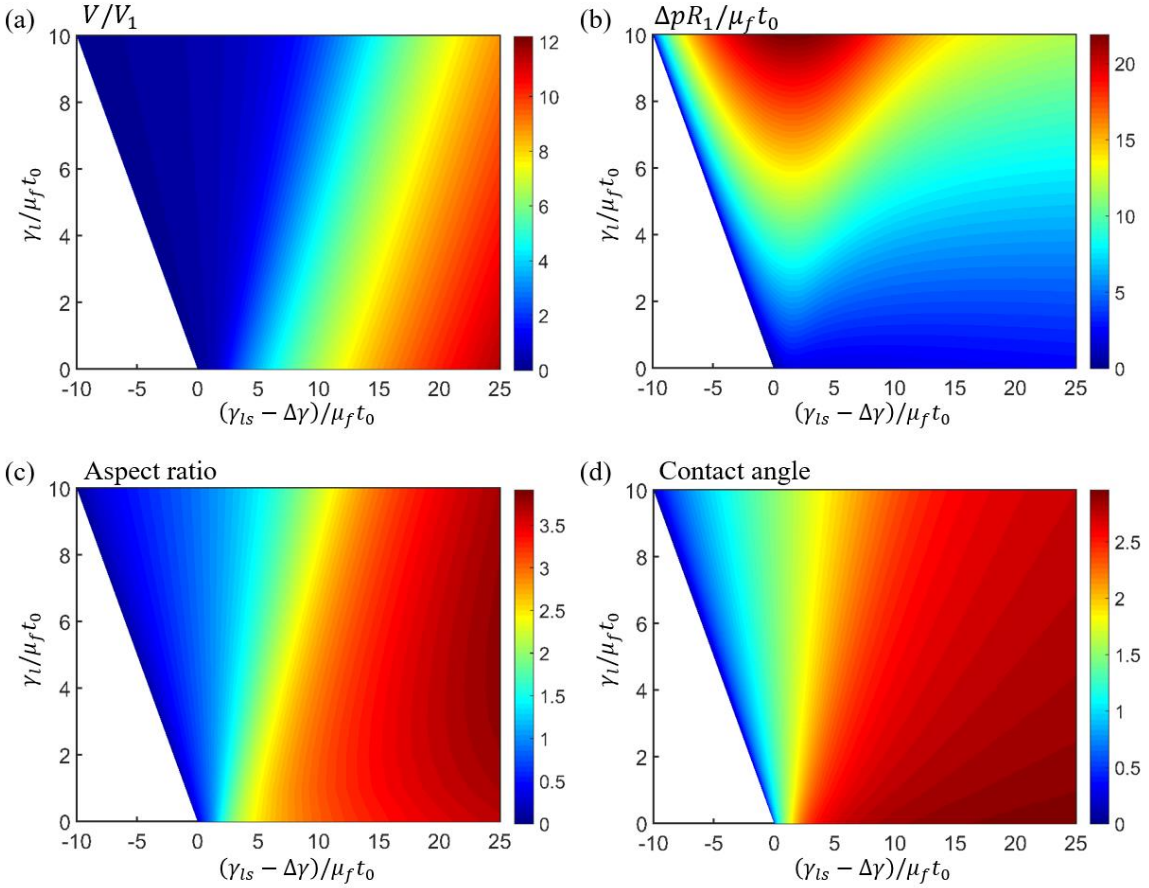

Figure 3.15 (a)-(d): contour plots of normalized blister volume, pressure, aspect ratio, and contact angle as functions of $\gamma_l/\mu_f t_0$ and $(\gamma_{ls}-\Delta\gamma)/\mu_f t_0$. Blister layer is modeled as incompressible Gent material with $J_m = 100$

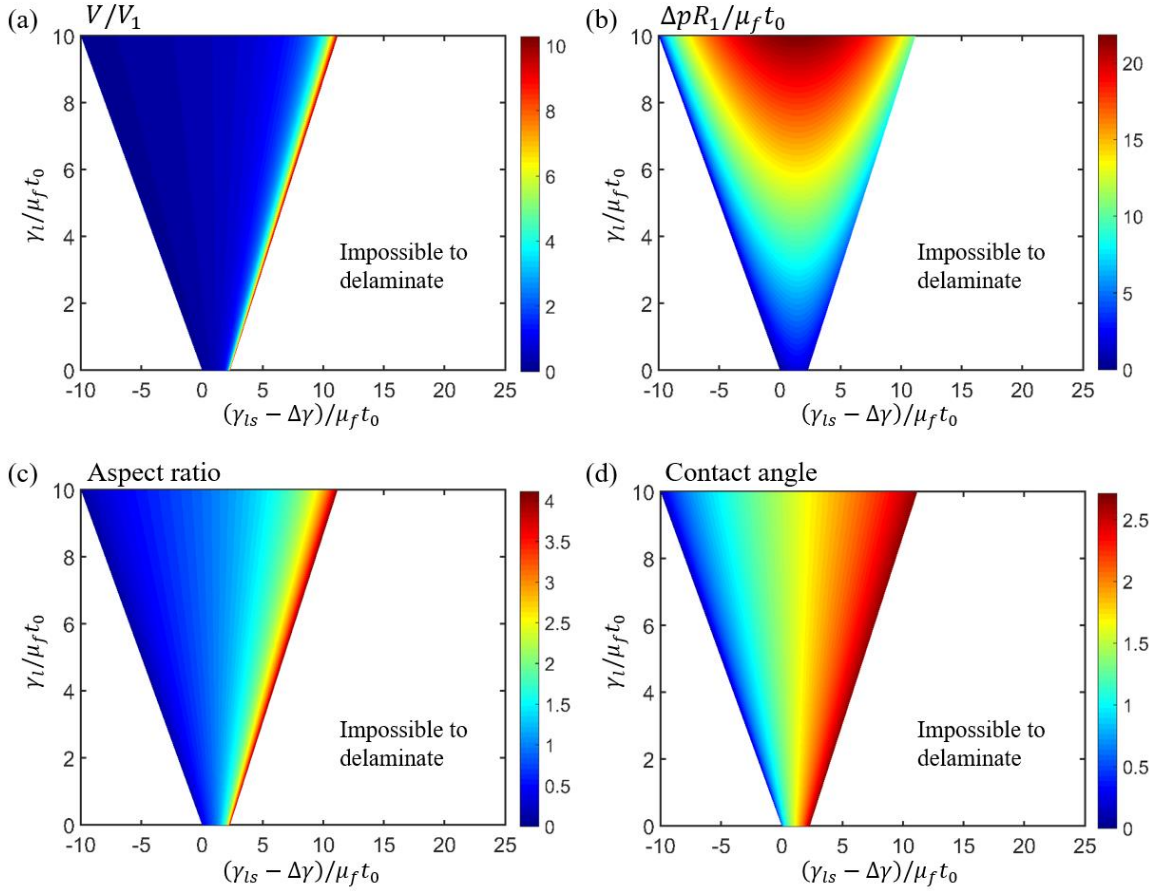

Figure 3.16 (a)-(d): contour plots of normalized blister volume, pressure, aspect ratio, and contact angle as functions of $\gamma_l/\mu_f t_0$ and $(\gamma_{ls}-\Delta\gamma)/\mu_f t_0$. Blister layer is modeled as incompressible Neo-Hookean material

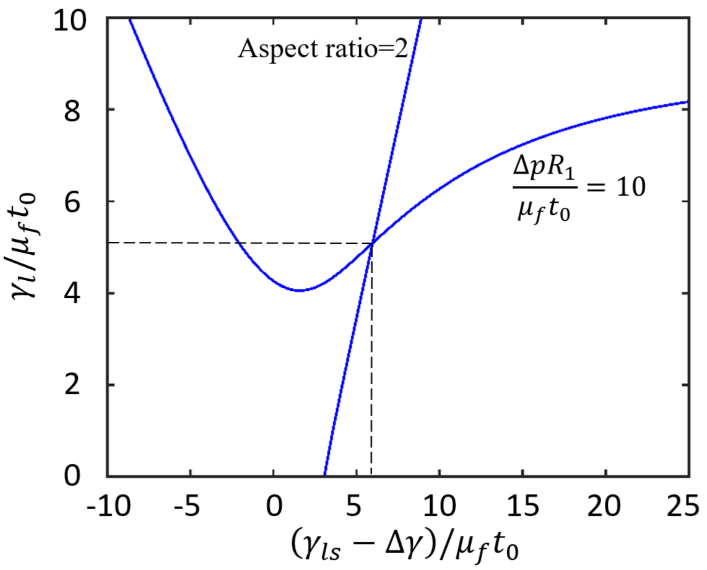

Figure 3.17 Contour curves for aspect ratio = 2, and $\gamma_l/\mu_f t_0$ and $\Delta pR_1/\mu_f t_0 = 10$ in $\gamma_l/\mu_f t_0 \sim (\gamma_{ls} - \Delta\gamma)/\mu_f t_0$ parametric space. The lister layer is modeled as incompressible Gent material with $J_m = 100$

Contour plots in Figures 3.14 and 3.15 can be used to help extract $\gamma_l/\mu_f t_0$ and $(\gamma_{ls} - \Delta\gamma)/\mu_f t_0$ in experiments. For example, in a volume controlled blister test in which the mechanical behavior of the blister layer is characterized by incompressible Gent material with $J_m = 100$, once delamination propagation is observed, one can measure the blister aspect ratio and blister pressure experimentally. If the corresponding aspect is found to be 2 and $\Delta pR_1/\mu t_0 = 10$, then using Figures 3.15b and 3.15c, one can plot contour curves of aspect ratio = 2, and $\Delta pR_1/\mu t_0 = 10$ in $\gamma_l/\mu_f t_0 \sim (\gamma_{ls} - \Delta\gamma)/\mu_f t_0$ parametric space, as shown in Figure 3.17. The intersected point of the two curves yields $\gamma_l/\mu_f t_0 = 5.1$ and $(\gamma_{ls} - \Delta\gamma)/\mu_f t_0 = 15.9$.

Slippery Boundary:

Slippery boundary applies to blister layers covering wet surfaces. The initially bonded part may slide in lateral direction but is still considered as “attached” to substrate, unless it’s delaminated from the substrate, i.e. $z_f > 0$. Similar with adhesive boundary, by analyzing the system free energy, we can find the critical volume V_c that delamination propagation sets in.

Figure 3.18 displays two pressurized blisters at $V/V_0 = 1.5$ with $\alpha = 0.5$, and $(\gamma_{ls} - \Delta\gamma)/\mu_f t_0 = 2.5$. Incompressible Gent material with $J_m = 100$ is used to model the blister layers in Figure 3.18, as well as the rest part of this subsection. Since the attached part of the blister layer also deforms, the system free energy Π should include the strain energy stored in the blister layer that is attached to the substrate ($R > R_0$ or $R > R_1$). The normalized free energy, $\Pi/(\pi R_0^2 \mu_f t_0)$, was found to be 10.0 and 24.5 for configurations with and without delamination propagation, respectively. Thus, delamination propagation does occur at $V/V_0 = 1.5$ as it produces lower free energy.

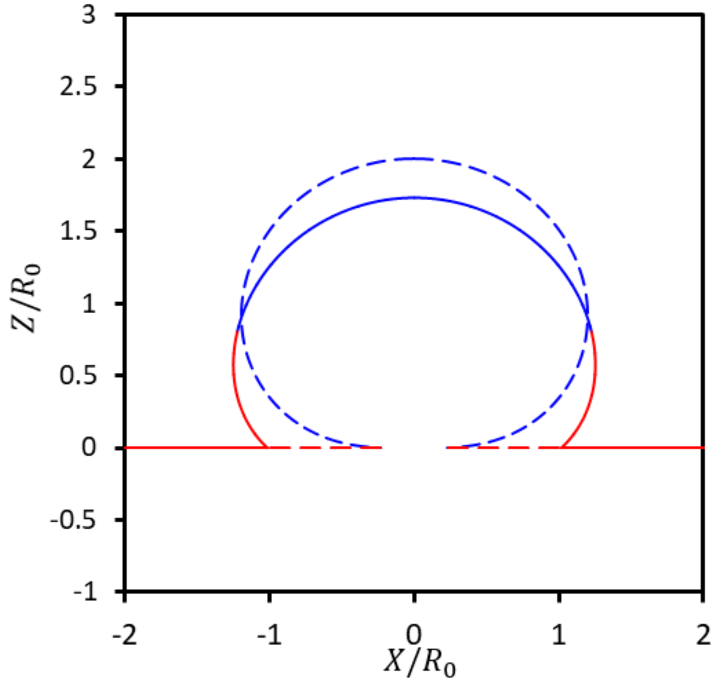

Figure 3.18 Side views of blister profiles at $V/V_0 = 1.5$ with $\alpha = 0.5$, and $(\gamma_{ls} - \Delta\gamma)/\mu_f t_0 = 2.5$. Dashed and solid curves are obtained using slippery boundary conditions without and with consideration of delamination propagation, respectively. For both configurations, blue part of the curve represents the blister layer that's initially delaminated from the substrate, whereas the red part is initially bonded to the substrate

As a blister with slippery boundary being pressurized, the attached part is dragged inward which creates compressive hoop stress around the contact line ($R = R_1$ or $R = R_0$). As shown in Figure 3.19, due to delamination, the compressive membrane hoop stress is released (solid curve). However, further pressurization could increase higher compressive hoop stress in the blister layer that may cause instabilities in circumferential direction, as observed in [57, 58]. The instability behavior of blisters with slippery boundary is out of the scope of this dissertation, and will not be considered in the rest of this dissertation.

Similar to the adhesive boundary, Figure 3.20 is generated plotting the normalized pressure-volume and free energy-volume relations. Figure 3.20 uses the same parameter as in Figure 3.13, but the critical blister volume is found to be $V_c = 0.35V_0$, smaller compared to that of adhesive boundary ($V_c = 1.17V_0$). According to Figure 3.20b, delamination propagation leads to lower free energy when $V > V_c$, so that delamination propagation always occurs for $V > V_c$.

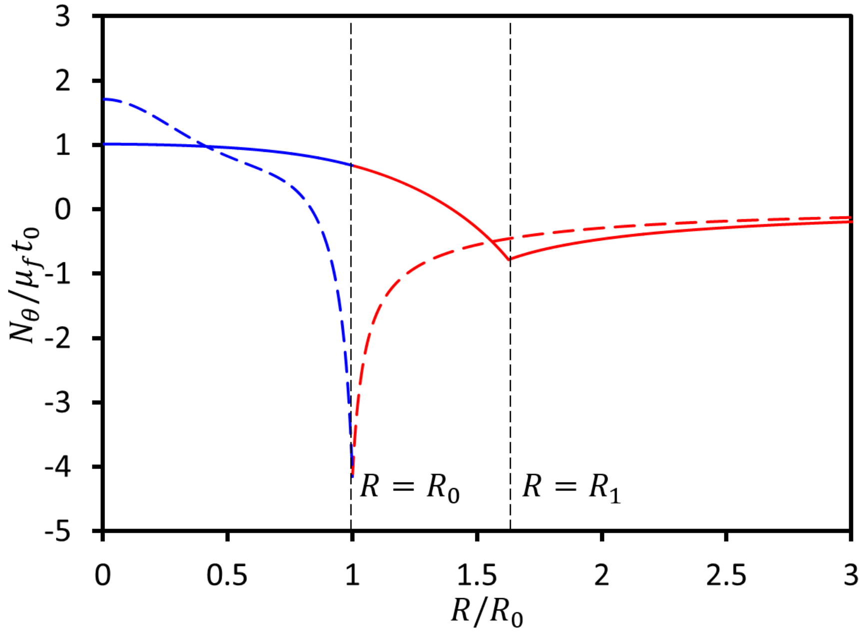

Figure 3.19 Distribution of $N_\theta/\mu_f t_0$ for equilibrium status shown in Figure 3.18

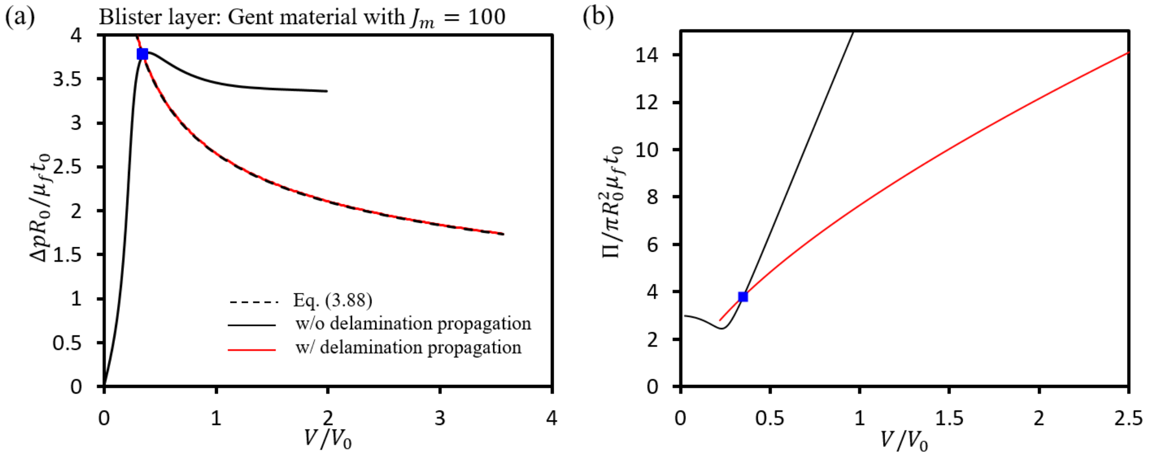

Figure 3.20 Computed (a) pressure-volume and (b) free energy-volume relations. Red curves represent configurations with delamination propagation, while black curves are without delamination propagation.

Chapter 4 Blisters on Soft Substrates

Blisters on soft substrates are modeled in this chapter. Based on the nonlinear membrane theory formulated in Chapter 3, a boundary value problem for a blister formed between a soft membrane and a soft substrate with adhesive interface is developed. Surface tensions of the soft material and the fluid, and the membrane-substrate interface adhesive energy are taken into consideration. To solve the nonlinear boundary value problem, finite element formulation was derived and surface tension effect was implemented in Abaqus through user defined element (UEL). For the sake of simplicity, in this chapter, only incompressible Neo-Hookean material model is used for both the membrane and the substrate.

4.1 FORMULATIONS OF THE BOUNDARY VALUE PROBLEM

If the substrate is soft or flexible (see Figure 4.1), the total free energy of a blister with thickness t_0 is

$$\Pi = U_f + U_s - \Delta pV + \gamma_l A_l + \gamma_{ls} A_{ls} + \Delta\gamma A_s \tag{4.1}$$

where Δp, U_f, V, γ_l, γ_{ls} and $\Delta\gamma$ remain the same meanings as in Eq. (3.42), and in addition,

$U_s =$ the strain energy of the substrate,

$A_l =$ the area of the liquid/blister-layer interface,

$A_{ls} =$ the area of the liquid/substrate interface,

$A_s =$ the area of the blister-layer/substrate interface.

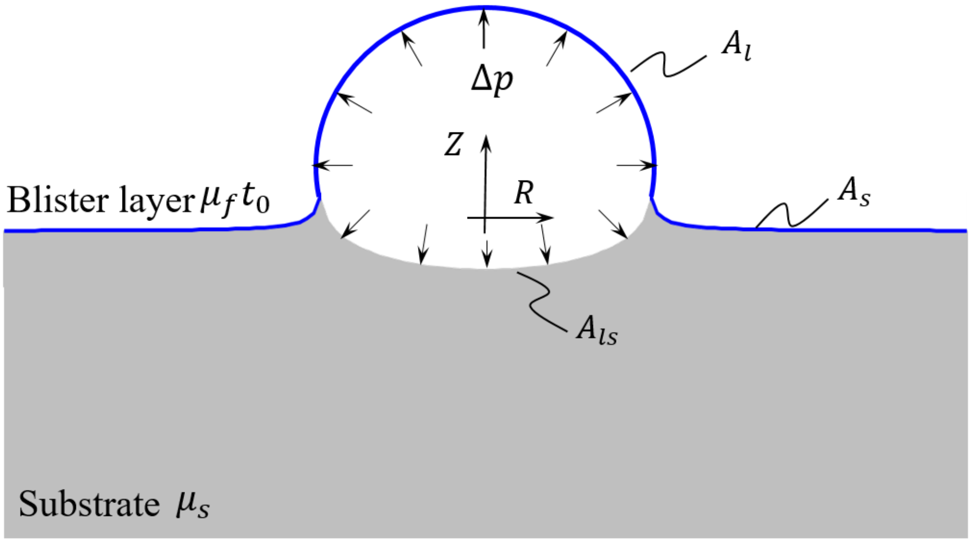

Figure 4.1 Schematic of a blister on soft substrate

Surface tension, γ, and the magnitude of surface stress, Υ, are the same for liquids. However, for many solids, changes in surface area are accommodated through the stretching of bonds between particles on the surface, leading to a nonconstant and non-isotropic surface stress [59, 60], Υ_{ij}, which is different from surface tension γ. For these materials, Υ_{ij} and γ are related by the Shuttleworth equation [61]

$$\Upsilon_{ij} = \gamma\delta_{ij} + \frac{\partial\gamma}{\partial\epsilon_{ij}} \tag{4.2}$$

where ϵ_{ij} denotes the strain components on the surface. In our study, γ_l, γ_{ls} and $\Delta\gamma$ are considered to be constant, i.e. they are independent with the deformation of the blister layer and the substrate, so that surface tension and surface stress are equal. This is true for amorphous polymeric materials that are lightly cross-linked, whose molecules have sufficient mobility to move from the bulk to the surface and vice versa, and thus, the behavior of surfaces of these materials is indeed fluid-like [59].

Considering the deformation of the substrate surface at $Z = 0$, we have

$$\begin{aligned}
U_f &= \int_0^{R_0} 2\pi R t_0 W_f dR + \int_{R_0}^{\infty} 2\pi R t_0 W_f dR \\
U_s &= \int_0^{\infty}\int_{-\infty}^{0} 2\pi R W_s dZ dR \\
V &= \int_0^{R_0} 2\pi\left(r_f r_f' z_f - r_s r_s' z_s\right) dR \\
A_l &= \int_0^{R_0} 2\pi r_f \sqrt{r_f'^2 + z_f'^2} dR \\
A_{ls} &= \int_0^{R_0} 2\pi r_s \sqrt{r_s'^2 + z_s'^2} dR \\
A_s &= \int_{R_0}^{\infty} 2\pi r_f \sqrt{r_f'^2 + z_f'^2} dR
\end{aligned} \tag{4.3}$$

where r_f, z_f and W_f remain the same meanings as in Chapter 3, R_0, and r_0 are still the locations of the contact line of the blister in undeformed and deformed configurations, and

$\left(r_s(R), z_s(R)\right) =$ the deflection profile of the substrate surface at $Z = 0$,

$W_s =$ the strain energy density function of the material of the substrate.

In cylindrical coordinate system, the deformed configuration of the substrate is described by

$$r = r(R, Z) \text{ and } z = z(R, Z) \;\; \forall R \geq 0, Z \leq 0 \tag{4.4}$$

Then, It's straightforward that

$$r_s(R) = r(R, 0), z_s(R) = z(R, 0) \tag{4.5}$$

In this chapter, we only focus on adhesive boundaries as described in Section 3.2.1. Thus, at $Z = 0$, we have

$$r_f = r_s, z_f = z_s \;\forall R > R_0 \tag{4.6}$$

Note that even though gravity of the liquid inside the blister is neglected in Eq. (4.1), one can still take it into consideration by adopting the gravity potential Φ in system free energy Π, where

$$\Phi = \int_0^{R_0} 2\pi \frac{1}{2} \rho g \left(r_f r_f' z_f^2 - r_s r_s' z_s^2\right) dR \tag{4.7}$$

We use λ_r^f and λ_θ^f to denote the principal stretches of the blister layer, and λ_r^s, λ_θ^s to present the principal stretches of the substrate surface at $Z = 0$. Following Eq. (3.23), we have

$$\begin{gathered} \lambda_r^f = \sqrt{{r_f'}^2 + {z_f'}^2}, \lambda_\theta^f = \frac{r_f}{R} \\ \lambda_r^s = \sqrt{{r_s'}^2 + {z_s'}^2}, \lambda_\theta^s = \frac{r_s}{R} \end{gathered} \tag{4.8}$$

so that

$$W_f = W_f\left(\lambda_r^f, \lambda_\theta^f\right) = W_f\left(r_f, r_f', z_f'\right) \tag{4.9}$$

As to the substrate, considering the axisymmetry in cylindrical coordinate, the deformation gradient $\boldsymbol{F} = F_{iJ} \boldsymbol{e}_i \otimes \boldsymbol{E}_J$ is written as

$$\boldsymbol{F} = \frac{\partial r}{\partial R} \boldsymbol{e}_r \otimes \boldsymbol{E}_R + \frac{\partial r}{\partial Z} \boldsymbol{e}_r \otimes \boldsymbol{E}_Z + \frac{r}{R} \boldsymbol{e}_\theta \otimes \boldsymbol{E}_\Theta + \frac{\partial z}{\partial R} \boldsymbol{e}_z \otimes \boldsymbol{E}_R + \frac{\partial z}{\partial Z} \boldsymbol{e}_z \otimes \boldsymbol{E}_Z \tag{4.10}$$

where $\boldsymbol{e}_i$ $(i = r, \theta, z)$ and $\boldsymbol{E}_J$ $(J = R, \Theta, Z)$ represent the basis vectors in deformed and undeformed configurations, respectively. In the furture, in order to simplify expressions, we use the following notations to denote partial differentiations

$$r_{,R} = \frac{\partial r}{\partial R}, r_{,Z} = \frac{\partial r}{\partial Z}, z_{,R} = \frac{\partial z}{\partial R}, z_{,Z} = \frac{\partial z}{\partial Z} \tag{4.11}$$

According to Eq. (4.10), the principal stretches in the substrate can be expressed in terms of r, $r_{,R}$, $r_{,Z}$, $z_{,R}$ and $z_{,Z}$, and therefore, we have

$$W_s = W_s(r, r_{,R}, r_{,Z}, z_{,R}, z_{,Z}) \tag{4.12}$$

Thus, the total free energy Π is

$$\Pi = \Pi(r_f, r_f', z_f', r, r_{,R}, r_{,Z}, z_{,R}, z_{,Z}) \tag{4.13}$$

The corresponding Euler-Lagrangian equations as well as boundary conditions can be developed following the minimum principle of total free energy

$$\delta\Pi = \delta U_f + \delta U_s - \Delta p\delta V + \gamma_l \delta A_l + \gamma_{ls}\delta A_{ls} + \Delta\gamma\delta A_s = 0 \tag{4.14}$$

or

$$\delta\int_0^{R_0} F_1 dR + \delta\int_0^{R_0} F_2 dR + \delta\int_{R_0}^{\infty} F_3 dR + \delta\int_0^{\infty}\int_{-\infty}^{0} F_s dZ dR = 0 \tag{4.15}$$

where

$$\begin{aligned} F_1 &= Rt_0W_f - \Delta p r_f r_f' z_f + \gamma_l r_f\sqrt{{r_f'}^2 + {z_f'}^2}, \\ F_2 &= \Delta p r_s r_s' z_s + \gamma_{ls} r_s\sqrt{{r_s'}^2 + {z_s'}^2}, \\ F_3 &= Rt_0W_f + \Delta\gamma r_f\sqrt{{r_f'}^2 + {z_f'}^2}, \text{ and } F_s = RW_s \end{aligned} \tag{4.16}$$

4.1.1 Substrate

In Eq. (4.15), we have $\delta\int_0^{\infty}\int_{-\infty}^{0} F_s dZ dR$ written as

$$\begin{aligned} &\int_0^{\infty}\int_{-\infty}^{0}\left(\frac{\partial F_s}{\partial r} - \frac{\partial}{\partial R}\frac{\partial F_s}{\partial r_R} - \frac{\partial}{\partial Z}\frac{\partial F_s}{\partial r_Z}\right)\delta r + \left(\frac{\partial F_s}{\partial z} - \frac{\partial}{\partial R}\frac{\partial F_s}{\partial z_R} - \frac{\partial}{\partial Z}\frac{\partial F_s}{\partial z_Z}\right)\delta z dZ dR + \\ &\int_0^{\infty}\int_{-\infty}^{0}\frac{\partial}{\partial R}\left(\frac{\partial F_s}{\partial r_R}\delta r + \frac{\partial F_s}{\partial z_R}\delta z + F_s\delta R\right) + \frac{\partial}{\partial Z}\left(\frac{\partial F_s}{\partial r_Z}\delta r + \frac{\partial F_s}{\partial z_Z}\delta z + F_s\delta Z\right) dZ dR \end{aligned} \tag{4.17}$$

Applying divergence theorem, the second integral of Eq. (4.17) can be expressed as

$$\oint \left(\frac{\partial F_s}{\partial r_R}\delta r + \frac{\partial F_s}{\partial z_R}\delta z\right) dZ - \left(\frac{\partial F_s}{\partial r_Z}\delta r + \frac{\partial F_s}{\partial z_Z}\delta z\right) dR \tag{4.18}$$

where the line integral goes in the counterclockwise direction in $R-Z$ plane. We denote the far field boundary of the substrate as Γ_∞^s (see Figure 4.2). Then, the line integral in Eq. (4.18) can be split into three parts,

$$\oint \left[\left(\frac{\partial F_s}{\partial r_R}\delta r + \frac{\partial F_s}{\partial z_R}\delta z\right) dZ - \left(\frac{\partial F_s}{\partial r_Z}\delta r + \frac{\partial F_s}{\partial z_Z}\delta z\right) dR\right] = H_1 + H_2 + H_3 \tag{4.19}$$

where

$$\begin{aligned} H_1 &= -\int_{-\infty}^{0} \left(\frac{\partial F_s}{\partial r_R}\delta r + \frac{\partial F_s}{\partial z_R}\delta z\right)\Big|_{R=0} dZ \\ H_2 &= \int_{0}^{\infty} \left(\frac{\partial F_s}{\partial r_Z}\delta r + \frac{\partial F_s}{\partial z_Z}\delta z\right)\Big|_{Z=0} dR \end{aligned} \tag{4.20}$$

and

$$H_3 = \int_{\Gamma_\infty^s} \left(\frac{\partial F_s}{\partial r_R}\delta r + \frac{\partial F_s}{\partial z_R}\delta z\right) dZ - \left(\frac{\partial F_s}{\partial r_Z}\delta r + \frac{\partial F_s}{\partial z_Z}\delta z\right) dR \tag{4.21}$$

Then, $H_1 = 0$ essentially provides the regularity of functions r and z at $R = 0$, i.e.

$$r(0,Z) = z_{,R}(0,Z) = 0 \tag{4.22}$$

while $H_3 = 0$ yields the boundary condition on Γ_∞^s, which will be discussed later. However, H_2 is not necessary to vanish and it should be kept in Eq. (4.15).

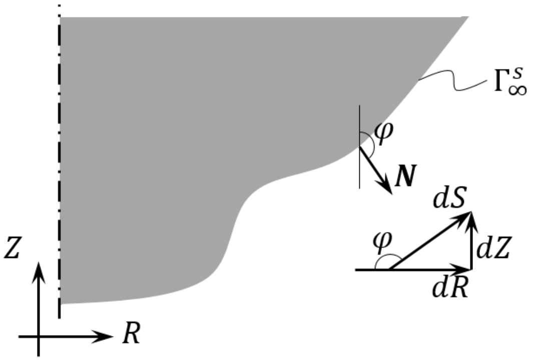

Figure 4.2 Schematic of the substrate boundary Γ^s_∞

According to Eq. (4.17), the Euler-Lagrangian equation of the substrate is

$$\begin{cases} \frac{\partial F_s}{\partial r} - \frac{\partial}{\partial R}\frac{\partial F_s}{\partial r_R} - \frac{\partial}{\partial Z}\frac{\partial F_s}{\partial r_Z} = 0 \\ \frac{\partial F_s}{\partial z} - \frac{\partial}{\partial R}\frac{\partial F_s}{\partial z_R} - \frac{\partial}{\partial Z}\frac{\partial F_s}{\partial z_Z} = 0 \end{cases} \tag{4.23}$$

Inserting F_s into Eq. (4.23) leads to

$$\begin{cases} R\frac{\partial W_s}{\partial r} - \frac{\partial}{\partial R}R\frac{\partial W_s}{\partial r_R} - R\frac{\partial}{\partial Z}\frac{\partial W_s}{\partial r_Z} = 0 \\ R\frac{\partial W_s}{\partial z} - \frac{\partial}{\partial R}R\frac{\partial W_s}{\partial z_R} - R\frac{\partial}{\partial Z}\frac{\partial W_s}{\partial z_Z} = 0 \end{cases} \tag{4.24}$$

Note that components of 1st Piola-Kirchhoff stress tensor $\boldsymbol{P}$ are defined as

$$P_{iJ} = \frac{\partial W_s}{\partial F_{iJ}} \tag{4.25}$$

and under cylindrical coordinates with consideration of axisymmetry, they can be expressed as

$$P_{rR} = \frac{\partial W_s}{\partial r_R}, P_{rZ} = \frac{\partial W_s}{\partial r_Z}, P_{\theta\Theta} = R\frac{\partial W_s}{\partial r}, P_{zR} = \frac{\partial W_s}{\partial z_R}, P_{zZ} = \frac{\partial W_s}{\partial z_Z} \tag{4.26}$$

Then, Eq. (4.24) can be reformulated into

$$\begin{cases} \frac{\partial P_{rR}}{\partial R} + \frac{\partial P_{rZ}}{\partial Z} + \frac{P_{rR} - P_{\theta\Theta}}{R} = 0 \\ \frac{\partial P_{zR}}{\partial R} + \frac{\partial P_{zZ}}{\partial Z} + \frac{P_{zR}}{R} = 0 \end{cases} \tag{4.27}$$

which is the equilibrium equations of the substrate. Furthermore, a brief expression of Eq. (4.27) is simply

$$\mathrm{Div}_{\boldsymbol{X}}\boldsymbol{P} = \boldsymbol{0} \tag{4.28}$$

where $\mathrm{Div}_{\boldsymbol{X}}$ is the divergence operator with respect to the undeformed configuration. Equation (4.28) is equivalent with

$$\mathrm{div}_{\boldsymbol{x}}\boldsymbol{\sigma} = \boldsymbol{0} \tag{4.29}$$

which is the force equilibrium equation in deformed configuration, where $\boldsymbol{\sigma}$ is the Cauchy stress tensor, and $\mathrm{div}_{\boldsymbol{x}}$ is the divergence operator with respect to the deformed configuration.

Define $\boldsymbol{N}$ as the unit normal vector of the boundary of the substrate domain in $R-Z$ plane in undeformed configuration. We have

$$\boldsymbol{N} = \sin\varphi\, \boldsymbol{E}_R + \cos\varphi\, \boldsymbol{E}_Z \tag{4.30}$$

where φ is the orientation angle of $\boldsymbol{N}$ (Figure 4.2). For an infinitesimal segment dS on Γ_∞^s, one has

$$dR = -\cos\varphi\, dS, dZ = \sin\varphi\, dS \tag{4.31}$$

Plugging Eqs. (4.26), (4.31) and F_s into H_3 produces

$$\int_{\Gamma_\infty^s} R[(P_{rR}\sin\varphi + P_{rZ}\cos\varphi)\delta r + (P_{zR}\sin\varphi + P_{zZ}\cos\varphi)\delta z]dS = 0 \tag{4.32}$$

which implies the traction free boundary condition

$$\begin{bmatrix} P_{rR} & P_{rZ} \\ P_{zR} & P_{zZ} \end{bmatrix} \begin{bmatrix} \sin\varphi \\ \cos\varphi \end{bmatrix} = \begin{bmatrix} 0 \\ 0 \end{bmatrix} \tag{4.33}$$

or $\boldsymbol{P}\cdot\boldsymbol{N} = \boldsymbol{0}$, or $\boldsymbol{\sigma}\cdot\boldsymbol{n} = \boldsymbol{0}$, where

$$\boldsymbol{n} = \frac{\boldsymbol{F}^{-T}\boldsymbol{N}}{\|\boldsymbol{F}^{-T}\boldsymbol{N}\|} \tag{4.34}$$

is the unit normal vector of the boundary of the substrate domain in deformed configuration.

4.1.2 Soft membrane

So far, Eq. (4.15) is left with

$$\delta\int_0^{R_0} F_1 dR + \delta\int_0^{R_0} F_2 dR + \delta\int_{R_0}^{\infty} F_3 dR + H_2 = 0 \tag{4.35}$$

Substituting F_1 and F_2 into Eq. (4.35), and considering the relationships given in Eq. (4.26), we obtain the corresponding Euler-Lagrangian equations at $Z = 0$:

$$\begin{cases} \kappa_r^f N_r + \kappa_\theta^f N_\theta + \gamma_l\left(\kappa_r^f + \kappa_r^f\right) + \Delta p = 0 \\ \dfrac{dN_r}{dR} + \dfrac{r_f'(N_r - N_\theta)}{r_f} = 0 \end{cases} \qquad \forall\, 0 \le R < R_0 \tag{4.36}$$

$$\begin{cases} \gamma_{ls}(\kappa_r^s + \kappa_\theta^s) + \dfrac{-\sin\phi_s P_{rZ} + \cos\phi_s P_{zZ}}{\lambda_r^s \lambda_\theta^s} - \Delta p = 0 \\ \cos\phi_s P_{rZ} + \sin\phi_s P_{zZ} = 0 \end{cases} \qquad \forall\, 0 \le R < R_0 \tag{4.37}$$

$$\begin{cases} \kappa_r^f N_r + \kappa_\theta^f N_\theta + \Delta\gamma\left(\kappa_r^f + \kappa_r^f\right) + \dfrac{-\sin\phi_f P_{rZ} + \cos\phi_f P_{zZ}}{\lambda_r^f \lambda_\theta^f} = 0 \\ \dfrac{dN_r}{dR} + \dfrac{r_f'(N_r - N_\theta)}{r_f} + \dfrac{\cos\phi_f P_{rZ} + \sin\phi_f P_{zZ}}{\lambda_\theta^f} = 0 \end{cases} \qquad \forall\, R > R_0 \tag{4.38}$$

where

$$\begin{gathered} N_r = \frac{t_0}{\lambda_\theta^f}\frac{\partial W_f}{\partial \lambda_r^f}, N_\theta = \frac{t_0}{\lambda_r^f}\frac{\partial W_f}{\partial \lambda_\theta^f} \\ \kappa_r^f = \frac{r_f' z_f'' - r_f'' z_f'}{\left(r_f'^2 + z_f'^2\right)^{3/2}}, \kappa_\theta^f = \frac{z_f'}{r_f\left(r_f'^2 + z_f'^2\right)^{1/2}}, \\ \kappa_r^s = \frac{r_s' z_s'' - r_s'' z_s'}{(r_s'^2 + z_s'^2)^{3/2}}, \kappa_\theta^s = \frac{z_s'}{r(r_s'^2 + z_s'^2)^{1/2}} \end{gathered} \tag{4.39}$$

and ϕ_f and ϕ_s are defined in the same way as Eq. (3.39). In addition, $\phi_s = \phi_f$, $\kappa_r^s = \kappa_r^f$ and $\kappa_\theta^s = \kappa_\theta^f$ for $R > R_0$ according to Eq. (4.6). As we can see, Eq. (4.36) has the same form with Eq. (3.47). However, Eqs. (4.37) and (4.38) contains extra terms involving the substrate deformation, aand are difficult to be interpreted. Further reformulation of Eqs. (4.37) and (4.38) is needed in order to understand their physical meanings.

The surface traction in deformed configuration is

$$\boldsymbol{\sigma} \cdot \boldsymbol{n} = \frac{\boldsymbol{P} \cdot \boldsymbol{N}}{J\|\boldsymbol{F}^{-T} \cdot \boldsymbol{N}\|} \tag{4.40}$$

where $\| \quad \|$ presents the Euclidian norm, $J = \mathrm{Det}(\boldsymbol{F})$ is the Jacobian of deformation gradient $\boldsymbol{F}$, and $\boldsymbol{F}^{-T}$ is the inverse of the transpose of $\boldsymbol{F}$, which can be expressed as

$$\begin{aligned} \boldsymbol{F}^{-T} = & \frac{1}{J}\frac{r}{R}(z_{,Z}\ \boldsymbol{e}_r \otimes \boldsymbol{E}_R - z_{,R}\ \boldsymbol{e}_r \otimes \boldsymbol{E}_Z - r_{,Z}\ \boldsymbol{e}_z \otimes \boldsymbol{E}_R + r_{,R}\ \boldsymbol{e}_z \otimes \boldsymbol{E}_Z) \\ & + \frac{R}{r}\ \boldsymbol{e}_\theta \otimes \boldsymbol{E}_\Theta \end{aligned} \tag{4.41}$$

At $Z = 0$, the unit normal vector of the substrate surface under undeformed configuration is $\boldsymbol{N} = \boldsymbol{E}_Z$. Thus, inserting Eqs. (4.10) and (4.41) into Eq. (4.40) leads to

$$\boldsymbol{\sigma} \cdot \boldsymbol{n} = \frac{R}{r}\frac{P_{rZ}\boldsymbol{e}_r + P_{zZ}\boldsymbol{e}_z}{\sqrt{r_{,R}^2 + z_{,R}^2}} = \frac{R}{r_s}\frac{P_{rZ}\boldsymbol{e}_r + P_{zZ}\boldsymbol{e}_z}{\sqrt{r_s'^2 + z_s'^2}} = \frac{P_{rZ}\boldsymbol{e}_r + P_{zZ}\boldsymbol{e}_z}{\lambda_r^s \lambda_\theta^s} \tag{4.42}$$

Under deformed configuration, the unit normal vector $\boldsymbol{n}$ of the substrate surface at $Z = 0$ is

$$\begin{aligned} \boldsymbol{n} &= \frac{\boldsymbol{F}^{-T} \cdot \boldsymbol{N}}{\|\boldsymbol{F}^{-T} \cdot \boldsymbol{N}\|} = \frac{-z_R\ \boldsymbol{e}_r + r_R\ \boldsymbol{e}_z}{\sqrt{r_R^2 + z_R^2}} = \frac{-z_s'\ \boldsymbol{e}_r + r_s'\ \boldsymbol{e}_z}{\sqrt{{r_s'}^2 + {z_s'}^2}} \\ &= \sin\phi_s\ \boldsymbol{e}_r - \cos\phi_s\ \boldsymbol{e}_z \end{aligned} \tag{4.43}$$

and the unit shear vector $\boldsymbol{\tau}$ is obtained by rotating the normal vector by $\pi/2$ conterclockwisely, i.e.

$$\boldsymbol{\tau} = \sin\left(\phi_s - \frac{\pi}{2}\right)\boldsymbol{e}_r - \cos\left(\phi_s - \frac{\pi}{2}\right)\boldsymbol{e}_z = -\cos\phi_s\ \boldsymbol{e}_r - \sin\phi_s\ \boldsymbol{e}_z \tag{4.44}$$

Then the surface traction exerted on the $Z = 0$ surface of the substrate has normal and shear components t_n and t_τ that can be expressed as the following

$$\begin{aligned} t_n &= \boldsymbol{n} \cdot (\boldsymbol{\sigma} \cdot \boldsymbol{n}) = \frac{\sin\phi_s\, P_{rZ} - \cos\phi_s\, P_{zZ}}{\lambda_r^s \lambda_\theta^s} \\ t_\tau &= \boldsymbol{\tau} \cdot (\boldsymbol{\sigma} \cdot \boldsymbol{n}) = -\frac{\cos\phi_s\, P_{rZ} + \sin\phi_s\, P_{zZ}}{\lambda_r^s \lambda_\theta^s} \end{aligned} \tag{4.45}$$

Thus, considering Eq. (4.45), Eqs. (4.37) and (4.38) can be rewritten as

$$\begin{cases} \gamma_{ls}(\kappa_r^s + \kappa_\theta^s) - t_n - \Delta p = 0 \\ t_\tau = 0 \end{cases} \qquad \forall\, 0 \le R < R_0, Z = 0$$

$$\begin{cases} \kappa_r^f N_r + \kappa_\theta^f N_\theta + w\left(\kappa_r^f + \kappa_r^f\right) - t_n = 0 \\ \dfrac{dN_r}{dR} + \dfrac{r_f'(N_r - N_\theta)}{r_f} - \lambda_r^s t_\tau = 0 \end{cases} \qquad \forall\, R > R_0, Z = 0 \tag{4.46}$$

4.1.3 Boundary Conditions

For adhesive boundaries, we have the following relations

$$\begin{gathered} \left(\delta r_f\right)(0) = \delta r_f(0) = 0, \left(\delta z_f\right)(0) = \delta z_f(0) \neq 0 \\ (\delta r_s)(0) = \delta r_s(0) = 0, (\delta z_s)(0) = \delta z_s(0) \neq 0 \\ \delta R_0^- = \delta R_0^+ = \delta R_0 \end{gathered} \tag{4.47}$$

Define (r_0, z_0) as the location of the blister boundary, i.e. "contact line", under deformed configuration. The continuity at contact line implies

$$\begin{gathered} r_f\left(R_0^\pm\right) = r_s\left(R_0^\pm\right) = r_0, \\ z_f\left(R_0^\pm\right) = z_s\left(R_0^\pm\right) = z_0 \end{gathered} \tag{4.48}$$

As discussed in Section 3.2.1, we need to pay attention to the difference between the variation of the evaluation of a function and the evaluation of its variation at the same point. Following Eq. (3.52), we have

$$\begin{gathered} \left(\delta r_f\right)\left(R_0^\pm\right) = \delta r_0 - r_f'\left(R_0^\pm\right)\delta R_0 = \delta r_0 + \cos\phi_f^\pm\, \lambda_f^\pm \delta R_0, \\ \left(\delta z_f\right)\left(R_0^\pm\right) = \delta z_0 - z_f'\left(R_0^\pm\right)\delta R_0 = \delta z_0 + \sin\phi_f^\pm\, R_0^\pm \delta R_0, \\ (\delta r_s)\left(R_0^\pm\right) = \delta r_0 - r_s'\left(R_0^\pm\right)\delta R_0 = \delta r_0 + \cos\phi_s^\pm\, \lambda_s^\pm \delta R_0, \\ (\delta z_s)\left(R_0^\pm\right) = \delta z_0 - z_s'\left(R_0^\pm\right)\delta R_0 = \delta z_0 + \sin\phi_s^\pm\, \lambda_s^\pm \delta R_0 \end{gathered} \tag{4.49}$$

With the help of Eqs. (4.47) and (4.49), the rest of Eq. (4.15) can be simplified into

$$\begin{aligned} &\left[R_0 t_0\left(W_f^- - W_f^+\right) - r_0\left(\lambda_r^{f-} N_r^- - \lambda_r^{f+} N_r^+\right)\right]\delta R_0 \\ &-\left[\cos\phi_f^-\,(N_r^- + \gamma_l) + \cos\phi_s^-\,\gamma_{ls} - \cos\phi_f^+\,(N_r^+ + \Delta\gamma)\right] r_0 \delta r_0 \\ &-r_0\left[\sin\phi_f^-\,(N_r^- + \gamma_l) + \sin\phi_s^-\,\gamma_{ls} - \sin\phi_f^+\,(N_r^+ + \Delta\gamma)\right]\delta z_0 \end{aligned} \tag{4.50}$$

$$+\left[\frac{r_f}{\lambda_r^f}(N_r+\Delta\gamma)\left(r_f'\delta r_f+z_f'\delta z_f\right)\right]\Bigg|_{\infty}=0$$

If the substrate is rigid, we have $r_s(R)=z_s(R)\equiv 0$, $z_f(R>R_0)\equiv 0$, $z_0=0$ $\phi_s(R)\equiv\pi$, and $\phi_f^+=0$, and, as a sequence, Eq. (4.50) recovers Eq. (3.58).

In order for Eq. (4.50) to be satisfied, we have

$$R_0t_0\left(W_f^- - W_f^+\right)-r_0\left(\lambda_r^{f-}N_r^- - \lambda_r^{f+}N_r^+\right)=0 \tag{4.51}$$

$$\cos\phi_f^-\,(N_r^-+\gamma_l)+\cos\phi_s^-\,\gamma_{ls}-\cos\phi_f^+\,(N_r^++\Delta\gamma)=0 \tag{4.52}$$

$$\sin\phi_f^-\,(N_r^-+\gamma_l)+\sin\phi_s^-\,\gamma_{ls}-\sin\phi_f^+\,(N_r^++\Delta\gamma)=0 \tag{4.53}$$

and $N_r+\Delta\gamma=0, z_f=0$ as $R\to\infty$. If the blister layer is removed, Eq. (4.51) vanishes and Eqs. (4.52) and (4.53) decay to

$$\begin{gathered}\cos\phi_f^-\,\gamma_l+\cos\phi_s^-\,\gamma_{ls}-\cos\phi_f^+\,\gamma_s=0\\ \sin\phi_f^-\,\gamma_l+\sin\phi_s^-\,\gamma_{ls}-\sin\phi_f^+\,\gamma_s=0\end{gathered} \tag{4.54}$$

which recovers the equations of Neumann's triangle [62]. For $R\geq R_0$, if the membrane and substrate are always perfectly bonded so that delamination does not propagate, then we are only left with Eqs. (4.52) and (4.53) at $R=R_0$. Once delamination propagation occurs, we need to use one more compatibility condition

$$R_0t_0\left(W_f^- - W_f^+\right)-r_0\left(\lambda_r^{f-}N_r^- - \lambda_r^{f+}N_r^+\right)=0 \tag{4.55}$$

to find R_0.

4.2. NUMERICAL METHOD

The boundary value problem we developed in Section 4.1 can be split into two boundary value problems:

Boundary value problem (BVP) of the blister layer:

Governing equations:

$$\begin{cases} \kappa_r^f N_r + \kappa_\theta^f N_\theta + \gamma_l\left(\kappa_r^f + \kappa_r^f\right) + \Delta p = 0 \\ \dfrac{dN_r}{dR} + \dfrac{r_f'(N_r - N_\theta)}{r_f} = 0 \end{cases} \qquad \forall\, 0 \le R < R_0, Z = 0 \tag{4.56}$$

Boundary conditions:

$$r_f(0) = z_f'(0) = 0, r_f(R_0) = r_0, z_f(R_0) = z_0 \tag{4.57}$$

Boundary value problem (BVP) of the substrate:

Governing equations:

$$\mathrm{div}_{\boldsymbol{x}}\boldsymbol{\sigma} = \boldsymbol{0}, \boldsymbol{\sigma} = \boldsymbol{\sigma}^T \ \ \forall \boldsymbol{x} \in \boldsymbol{B}(\Omega) \tag{4.58}$$

Boundary conditions:

$$\boldsymbol{\sigma} \cdot \boldsymbol{n} = \begin{cases} [\gamma_{ls}(\kappa_r^s + \kappa_\theta^s) - \Delta p]\boldsymbol{n} & \forall \boldsymbol{x} \in \boldsymbol{B}(\Gamma_1^s) \\ \left[\kappa_r^f N_r + \kappa_\theta^f N_\theta + \Delta\gamma\left(\kappa_r^f + \kappa_r^f\right)\right]\boldsymbol{n} + \dfrac{1}{\lambda_r^s}\left[\dfrac{dN_r}{dR} + \dfrac{r_f'(N_r - N_\theta)}{r_f}\right]\boldsymbol{\tau} & \forall \boldsymbol{x} \in \boldsymbol{B}(\Gamma_2^s) \\ (N_r^- + \gamma_l)\delta(\boldsymbol{x} - \boldsymbol{x}_0)\boldsymbol{v} & \text{for } \boldsymbol{x} = \boldsymbol{x}_0 \end{cases} \tag{4.59}$$

where

Ω =the domain occupied by the substrate= $\{(R, Z) | R \ge 0, Z < 0\}$,

Γ_0^s =the top surface of the substrate= $\{(R, Z) | R \ge 0, Z = 0\}$,

$\Gamma_1^s = \{(R, Z) | 0 \le R < R_0, Z = 0\} \subset \Gamma_0^s$,

$\Gamma_2^s = \{(R, Z) | R > R_0, Z = 0\} \subset \Gamma_0^s$,

$\boldsymbol{v} = \cos\phi_f^-\, \boldsymbol{e}_r + \sin\phi_f^-\, \boldsymbol{e}_z$,

$\boldsymbol{x}_0 = r_0\boldsymbol{e}_r + z_0\boldsymbol{e}_z = \boldsymbol{B}\big((R_0, 0)\big)$,

$\delta(\boldsymbol{x})$ =the Dirichlet delta function,

$\boldsymbol{n}$ =the unit normal vector of surface $\boldsymbol{B}(\Gamma_0^s) = \sin\phi_s\, \boldsymbol{e}_r - \cos\phi_s\, \boldsymbol{e}_z$,

$\boldsymbol{\tau}$ =the unit tangential vectors of surface $\boldsymbol{B}(\Gamma_0^s) = -\cos\phi_s\,\boldsymbol{e}_r - \sin\phi_s\,\boldsymbol{e}_z$,

$\boldsymbol{B}$ =the operation that transform the undeformed configuration into deformed configuration.

Note that $r_f \equiv r_s$ and $z_f \equiv z_s$ $\forall \boldsymbol{x} \in \boldsymbol{B}(\Gamma_2^s)$. Then, except for N_r^-, all the components in Eq. (4.59) can be expressed in terms of only r_s, z_s and their derivatives. Besides, $(N_r^- + \gamma_l)\delta(\boldsymbol{x} - \boldsymbol{x}_0)\boldsymbol{v}$ represents a line load $\boldsymbol{T} = (N_r^- + \gamma_l)\boldsymbol{v}$ applied at $\boldsymbol{x} = \boldsymbol{x}_0$ in direction $\boldsymbol{v}$. Thus, Eqs. (4.52) and (4.53) represent the force balance at the contact line

$$(N_r^- + \gamma_l)\boldsymbol{v} - \gamma_{ls}\boldsymbol{\tau}^- + (N_r^+ + \Delta\gamma)\boldsymbol{\tau}^+ = \boldsymbol{0} \tag{4.60}$$

where

$$\boldsymbol{\tau}^\pm = \boldsymbol{\tau}(R_0^\pm) = -\cos\phi_s^\pm\,\boldsymbol{e}_r - \sin\phi_s^\pm\,\boldsymbol{e}_z \tag{4.61}$$

The BVP of the blister layer for $0 \le R < R_0$ can still be solved using shooting method, whereas the BVP of the substrate will be solved by nonlinear finite element method (FEM). In the shooting method, boundary conditions $r_f(R_0) = r_0$ and $z_f(R_0) = z_0$ can be neglected firstly. For given Δp, we vary the initial condition $\lambda_r^f(0) = \lambda_\theta^f(0) = k$ in the shooting method to find solution(s) of the governing equations (Eq. (4.56)), which produces the corresponding r_f^-, ϕ_f^- and N_r^- at $R = R_0^-$. Due to the consideration of geometric and material nonlinearities, one may find no solution or multiple solutions for Eq. (4.56) at certain Δp. Once a solution of (r_f, z_f) for $0 \le R < R_0$ is obtained, the corresponding ϕ_f^- and N_r^- will be used to produce the dead load $\boldsymbol{T}$ applied on the substrate at $(R_0, 0)$ in undeformed configuration. A FEM code is used to solve the BVP of the substrate under load $\boldsymbol{T}$ with boundary conditions prescribed in (4.59). At equilibrium, the FEM result essentially satisfies Eqs. (4.52) and (4.53) automatically [59] (this point will be explained in next section). Besides, $r_s(R_0)$ and $z_s(R_0)$ can be extracted from the FEM result as well. If $r_s(R_0) \neq r_f^-$, we need to change the value of k and rerun the process until $r_s(R_0) = r_f^-$ is achieved; if $r_s(R_0) = r_f^-$ but Eq. (4.51) is not satisfied, then solutions of the two BVPs together form the solution of a blister on soft substrate under blister pressure Δp whose initial delamination size is R_0 and delamination propagation does not occur; moreover, if $r_s(R_0) = r_f^-$ and Eq. (4.51) are both satisfied, solutions of the two BVPs corresponds to a blister on soft substrate under blister pressure Δp whose initial delamination propagates from its initial size to R_0.

The solving routine described above is summarized in the following in Figure 4.3. In the process shown in Figure 4.3, parameters like γ_l, γ_{ls}, $\Delta\gamma$ and t_0 are fixed. One can also look into the effect of these parameters by varying the value of them at the beginning of the solving routine.

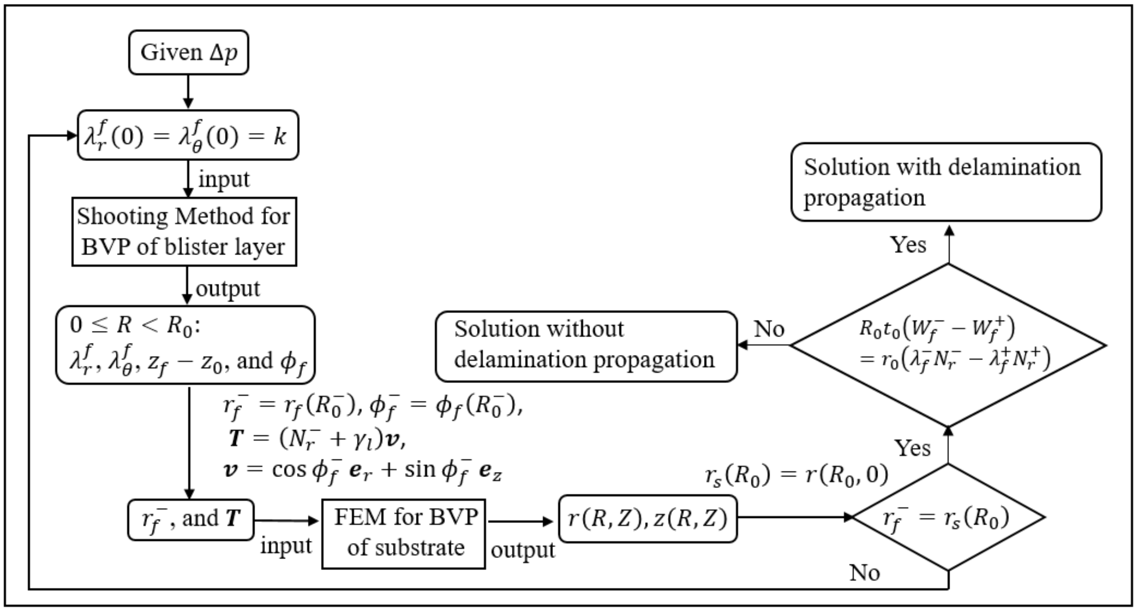

Figure 4.3 Flow chart for the solving routine of blister on soft substrate

4.3 FINITE ELEMENT FORMULATION

Define C as the contact line in undeformed configuration. According to the setup of BVP of the substrate in Section 4.2, we introduce a vector test field $\boldsymbol{w}$ and recast the equations of equilibriums (Eq. (4.58)), boundary conditions (Eq. (4.59)) and the force balance on $\boldsymbol{B}(C)$ (Eq. (4.60)) in the week form

$$\begin{aligned}
&-\int_{\boldsymbol{B}(\Omega)} \boldsymbol{\sigma}\colon \mathrm{grad}_{\boldsymbol{x}}\boldsymbol{w} d\mathrm{v} + \int_{\boldsymbol{B}(\Gamma_1^s)} [2\gamma_{ls}H - \Delta p]\boldsymbol{n}\cdot\boldsymbol{w} da \\
&+\int_{\boldsymbol{B}(\Gamma_2^s)} [N_r\kappa_r^s + N_\theta\kappa_\theta^s\ + 2\Delta\gamma H]\boldsymbol{n}\cdot\boldsymbol{w} + \frac{1}{\lambda_r^s}\left[\frac{dN_r}{dR} + \frac{r_s'(N_r - N_\theta)}{r_s}\right]\boldsymbol{t}\cdot\boldsymbol{w} da \\
&+\int_{\boldsymbol{B}(C)} [\boldsymbol{T} - \gamma_{ls}\boldsymbol{t}^- + (N_r^+ + \Delta\gamma)\boldsymbol{t}^+]\cdot\boldsymbol{w} ds = 0
\end{aligned} \tag{4.62}$$

where $\mathrm{grad}_{\boldsymbol{x}}\boldsymbol{w}$ is the gradient of $\boldsymbol{w}$ in deformed configuration, and $H = (\kappa_r^s + \kappa_\theta^s)/2$ is the mean curvature of surface $\boldsymbol{B}(\Gamma_0^s)$. Note that in the second line of Eq. (4.62), all the components should be expressed in terms of r_s, z_s and their derivatives, as discussed in Section 4.2. By applying the surface divergence theorem [63, 64], we obtain

$$\begin{aligned}
\int_{\boldsymbol{B}(\Gamma_1^s)} 2H\gamma_{ls}\boldsymbol{n}\cdot\boldsymbol{w} da &= \int_{\boldsymbol{B}(C)} \gamma_{ls}\boldsymbol{t}^-\cdot\boldsymbol{w} ds - \int_{\boldsymbol{B}(\Gamma_1^s)} \gamma_{ls}\mathrm{div}_{\boldsymbol{B}(\Gamma_1^s)}(\boldsymbol{w}) da \\
\int_{\boldsymbol{B}(\Gamma_2^s)} 2Hw\boldsymbol{n}\cdot\boldsymbol{w} da &= -\int_{\boldsymbol{B}(C)} w\boldsymbol{t}^+\cdot\boldsymbol{w} ds - \int_{\boldsymbol{B}(\Gamma_2^s)} w\mathrm{div}_{\boldsymbol{B}(\Gamma_2^s)}(\boldsymbol{w}) da
\end{aligned} \tag{4.63}$$

where $\mathrm{div}_{\boldsymbol{B}(\Gamma_1^s)}$ and $\mathrm{div}_{\boldsymbol{B}(\Gamma_2^s)}$ are the surface divergence operator defined on surfaces $\boldsymbol{B}(\Gamma_1^s)$ and $\boldsymbol{B}(\Gamma_1^s)$, respectively. Thus, Eq. (4.62) can be rewritten as

$$\begin{aligned}
&\int_{\boldsymbol{B}(\Omega)} \boldsymbol{\sigma}\colon \mathrm{grad}_{\boldsymbol{x}}\boldsymbol{w} d\mathrm{v} + \int_{\boldsymbol{B}(\Gamma_1^s)} \gamma_{ls}\mathrm{div}_{\boldsymbol{B}(\Gamma_1^s)}\cdot\boldsymbol{w} da + \int_{\boldsymbol{B}(\Gamma_2^s)} \Delta\gamma\mathrm{div}_{\boldsymbol{B}(\Gamma_2^s)}\cdot\boldsymbol{w} da \\
&= \int_{\boldsymbol{B}(\Gamma_2^s)} [N_r\kappa_r^s + N_\theta\kappa_\theta^s\ ]\boldsymbol{n}\cdot\boldsymbol{w} + \frac{1}{\lambda_r^s}\left[\frac{dN_r}{dR} + \frac{r_s'(N_r - N_\theta)}{r_s}\right]\boldsymbol{t}\cdot\boldsymbol{w} da \\
&+\int_{\boldsymbol{B}(C)} [\boldsymbol{T} + N_r^+\boldsymbol{t}^+]\cdot\boldsymbol{w} ds + \Delta p\int_{\boldsymbol{B}(\Gamma_1^s)} \boldsymbol{n}\cdot\boldsymbol{w} da
\end{aligned} \tag{4.64}$$

The finite element numerical solution procedure follows the work from Henann and Bertoldi [59]. The body of the substrate is approximated using finite elements, i.e. $\boldsymbol{B}(\Omega) =$

$\cup\, \boldsymbol{B}(\Omega^e)$. The nodal solution variable is taken to be the displacement, which is interpolated inside each element by

$$\boldsymbol{u} = \sum_A \boldsymbol{u}^A N^A \tag{4.65}$$

with the index $A = 1, 2, \ldots$ denoting the nodes of the element, $\boldsymbol{u}^A$ nodal displacements, and N^A the shape functions. We employ a standard Galerkin approach in that the test field is interpolated by the same shape functions,

$$\boldsymbol{w} = \sum_A \boldsymbol{w}^A N^A \tag{4.66}$$

Applying chain rule, we have

$$\begin{aligned}
&\int_{\boldsymbol{B}(\Gamma^s)} \mathrm{div}_{\boldsymbol{B}(\Gamma^s)} \cdot \left(\sum_A \boldsymbol{w}^A N^A\right) da \\
&= \sum_A \int_{\boldsymbol{B}(\Gamma^s)} \mathrm{grad}_{\boldsymbol{B}(\Gamma^s)} N^A \cdot \boldsymbol{w}^A + N^A \mathrm{div}_{\boldsymbol{B}(\Gamma^s)} \cdot \boldsymbol{w}^A da \\
&= \sum_A \left(\int_{\boldsymbol{B}(\Gamma^s)} \mathrm{grad}_{\boldsymbol{B}(\Gamma^s)} N^A da\right) \cdot \boldsymbol{w}^A
\end{aligned} \tag{4.67}$$

Thus, inserting Eqs. (4.65) ~ (4.67) into Eq. (4.64) yields the following system of equations

$$\boldsymbol{R}^A(\boldsymbol{u}) = \boldsymbol{0} \text{ for } A = 1,2, \ldots \tag{4.68}$$

where each $\boldsymbol{R}^A$ is a nonlinear equation of nodal displacements given as

$$\begin{aligned}
\boldsymbol{R}^A = &-\int_{\boldsymbol{B}(\Omega)} \boldsymbol{\sigma} \cdot \mathrm{grad}_{\boldsymbol{x}} N^A dv - \int_{\boldsymbol{B}(\Gamma_1^s)} \gamma_{ls}\, \mathrm{grad}_{\boldsymbol{B}(\Gamma_1^s)} N^A da \\
&- \int_{\boldsymbol{B}(\Gamma_2^s)} \Delta\gamma\, \mathrm{grad}_{\boldsymbol{B}(\Gamma_2^s)} N^A da + \int_{\boldsymbol{B}(C)} [\boldsymbol{T} + N_r^+ \boldsymbol{t}^+] N^A ds \\
&+ \int_{\boldsymbol{B}(\Gamma_2^s)} [N_r \kappa_r^s + N_\theta \kappa_\theta^s] N^A \boldsymbol{n} + \frac{1}{\lambda_r^s}\left[\frac{dN_r}{dR} + \frac{r_s'(N_r - N_\theta)}{r_s}\right] N^A \boldsymbol{t} da
\end{aligned} \tag{4.69}$$

This nonlinear system of equations is solved iteratively using Newton-Raphson method with corresponding tangent matrix

$$\boldsymbol{K}^{AB}(\boldsymbol{u}) = \frac{\partial \boldsymbol{R}^A(\boldsymbol{u})}{\partial \boldsymbol{u}^B} \tag{4.70}$$

with $A,\ B = 1, 2, \ldots$

4.4 IMPLEMENTATION OF SURFACE TENSION IN ABAQUS

The nonlinear system of equations can be solved iteratively using Newton-Raphson method. However, proper implementation of surface tension is required. Different methods of implementing surface tension in Abaqus have been reported [59, 65-69] and three common methods are summarized as the followings:

- Method 1: calculate the surface tension contribution to residuals in Eq. (4.69)

Consider four-noded, quadrilateral axisymmetric element. The surface tension contribution to residuals is,

$$\boldsymbol{R}_{\gamma}^{A}(\boldsymbol{u}) = -\gamma \int_{\boldsymbol{B}(\Gamma^{s})} \mathrm{grad}_{\boldsymbol{B}(\Gamma^{s})} N^{A} da \tag{4.71}$$

Following the work of Henann and Bertoldi [59], and Saksono and Peric [70], the element-level residuals and corresponding tangents[1] for face 1-2 shown in Figure 4.4 are

$$[R_{\gamma}] = -\frac{\pi\gamma(r_1+r_2)}{L}\begin{bmatrix} r_2-r_1 \\ z_2-z_1 \\ r_1-r_2 \\ z_1-z_2 \end{bmatrix} - \pi\gamma L \begin{bmatrix} 1 \\ 0 \\ 1 \\ 0 \end{bmatrix} \tag{4.72}$$

and

$$\begin{aligned}[K_{\gamma}] = &-\frac{\pi\gamma}{L}\begin{bmatrix} 2r_2 & 0 & -2r_1 & 0 \\ z_2-z_1 & r_1+r_2 & z_2-z_1 & -r_1-r_2 \\ -2r_2 & 0 & 2r_1 & 0 \\ z_1-z_2 & -r_1-r_2 & z_1-z_2 & r_1+r_2 \end{bmatrix} \\ &-\frac{\pi\gamma(r_1+r_2)}{L^3}\begin{bmatrix} r_2-r_1 \\ z_2-z_1 \\ r_1-r_2 \\ z_1-z_2 \end{bmatrix}\begin{bmatrix} r_2-r_1 \\ z_2-z_1 \\ r_1-r_2 \\ z_1-z_2 \end{bmatrix}^T + \frac{\pi\gamma}{L}\begin{bmatrix} 1 \\ 0 \\ 1 \\ 0 \end{bmatrix}\begin{bmatrix} r_2-r_1 \\ z_2-z_1 \\ r_1-r_2 \\ z_1-z_2 \end{bmatrix}^T \end{aligned} \tag{4.73}$$

where γ is the surface tension over surface 1-2, and $L = \sqrt{(r_1-r_2)^2 + (z_1-z_2)^2}$

---

[1] The author gratefully acknowledges Professor David Henann from Brown University for sharing his code.

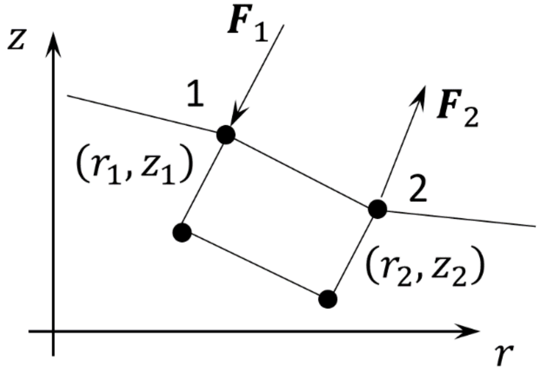

Figure 4.4 Schematic of the nodal forces due to surface tension

- Method 2: apply traction of the form $\boldsymbol{\sigma} \cdot \boldsymbol{n} = 2H\gamma\boldsymbol{n}$

The residual in Eq. (4.71) is equivalent with traction boundary condition $\boldsymbol{\sigma} \cdot \boldsymbol{n} = 2H\gamma\boldsymbol{n}$ on the surface, which can be applied through a user-subroutine DLOAD in Abaqus that allows for user-defined distributed loads as described in [65]. To calculate the mean curvature at an integration point, the coordinates of the integration points surrounding that point are needed. This data is obtained by using a FORTRAN module in [65], which is available globally during the analysis.

- Method 3: apply traction of the form $\partial\Pi_\gamma/\partial\boldsymbol{x}$

Identical nodal forces for traction forces $\boldsymbol{\sigma} \cdot \boldsymbol{n} = 2H\gamma\boldsymbol{n}$ can be obtained simply by considering the energy of surface between nodes 1-2:

$$\Pi_\gamma = \gamma\pi(r_1 + r_2)L \tag{4.74}$$

Due to Π_γ, at point 1, the conjugated nodal force $\boldsymbol{F}_1$ is

$$\begin{aligned} F_{1r} &= -\frac{\partial\Pi_\gamma}{\partial r_1} = \gamma\pi\left[\frac{(r_1 + r_2)(r_1 - r_2)}{L} - L\right] \\ F_{1z} &= -\frac{\partial\Pi_\gamma}{\partial z_1} = \gamma\pi\frac{(r_1 + r_2)(z_1 - z_2)}{L} \end{aligned} \tag{4.75}$$

The calculation of nodal forces $\boldsymbol{F}_1$ only depends on the coordinate of the point (r_1, z_1) and the other point (r_2, z_2) from the same element, and thus, can be implemented in user-defined element in Abaqus. In a series of works from Jagota and his colleagues [67-69], a two-node user defined surface element was developed and applied in various topics involving surface tensions[2] and would be used in this dissertation for our purpose.

After comprising the aforementioned 3 methods, we found that Method 3 is the best for our use. Though good accuracy can be achieved using any of these three methods, the computational cost of Method 3 is the lowest, and it is compatible with any existing mesh generation method, post processing, and element in Abaqus.

4.5 RESULTS AND DISCUSSIONS

The substrate is meshed using Abaqus 2-D axisymmetric elements CAX4H. We choose a domain $\Omega = \{(R, Z) | 0 \leq R \leq 10R_0, -10R_0 \leq Z \leq 0\}$ whose lateral size and depth are both 10 times of the initial blister radius, i.e. $10R_0$, so that the substrate could be considered as a half-space. For the sake of simplicity, only incompressible Neo-Hookean material model is used for both blister layer and substrate. μ_f and μ_s are used to denote the shear moduli of the substrate and the film. According to dimensional analysis, the deformation field of the substrate and the blister layer is governed by the following 5 dimensionless parameters: $\gamma_l/\mu_f t_0$, $\gamma_{ls}/\mu_f t_0$, $\Delta\gamma/\mu_f t_0$, $\mu_s R_0/\mu_f t_0$, and $\Delta p R_0/\mu_f t_0$.

---

[2] The author gratefully acknowledges Professor Anand Jagota from Leigh University for sharing his code.

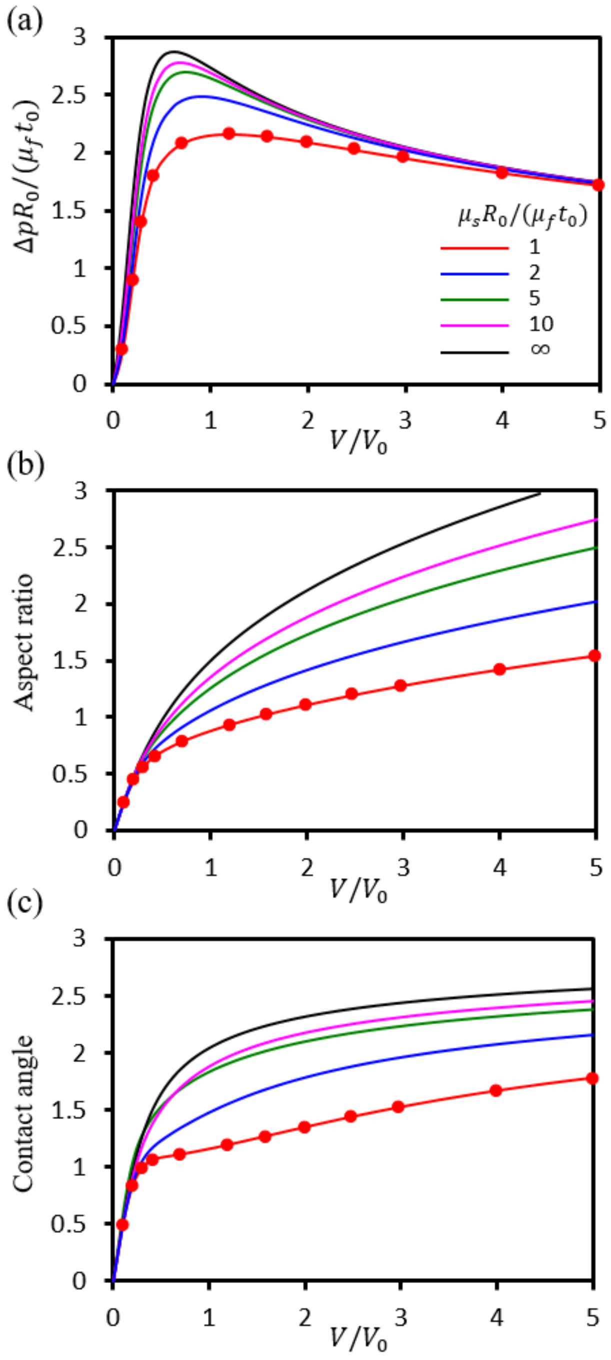

Figure 4.5 Computed (a) pressure-volume, (b) central deflection-volume, and (c) contact angle-volume relations with $\gamma_l = \gamma_{ls} = \Delta\gamma = 0.5\ \mu_f t_0$, and $\mu_s R_0/\mu_f t_0 = 1, 2, 5, 10, \infty$

Figure 4.5 plots the finite element results of normalized blister pressure ($\Delta p R_0/\mu_f t_0$), aspect ratio, and contact angle against the normalized blister volume (V/V_0), when delamination propagation is not allowed, i.e. $\delta R_0 = 0$. These results were produced by choosing $\gamma_l = \gamma_{ls} = \Delta\gamma = 0.5\mu_f t_0$ with $\mu_s R_0/\mu_f t_0$ varying from 1 to 10. The black curves in Figure 4.5 correspond to $\mu_s R_0/\mu_f t_0 \rightarrow \infty$, which represent results of a blister layer on rigid substrate with clamped boundary condition, and $\gamma_l = 0.5\mu_f t_0$. The aspect ratio of a blister on soft substrate is defined as $z_f(0)/r_0$, where $z_f(0)$ is the central deflection of the blister layer, and r_0 is the radial position of the contact line in deformed configuration. The results in Figure 4.5 indicate that, in a blister test, under the same blister volume, blisters on soft substrates have lower pressure, smaller aspect ratio, and smaller contact angle. The diminishment of blister layer deformation is due to the fact that the substrate deformation absorbs a portion of the energy that's done by increasing the blister volume. According to Figure 4.5, as $\mu_s R_0/\mu_f t_0$ increases, the behavior of blisters on soft substrates become more and more similar with blisters on rigid substrates. At $\gamma_l = 0.5\mu_f t_0$ and $\mu_s R_0/\mu_f t_0 > 10$, though the substrate deformation is still considerable around the contact line, the effect of substrate deformation on blister pressure, aspect ratio, and contact angle is already small enough and thus can be neglected. However, at $\mu_s R_0/\mu_f t_0 < 1$, the effect of substrate deformation is rather significant.

Figure 4.6 shows 12 representative deformed configurations of a blister on a soft substrate at $\mu_s R_0/\mu_f t_0 = 1$, corresponding to the 12 data points taken from Figure 4.5. From frame 1 to frame 12, the blister volume monotonically increases. In Figure 4.6, since delamination is not allowed to further propagate, the contact line in each frame represents the same material point, and it only advances due to the deformation of the substrate. The dashed line in each frame represents the position of the substrate surface in undeformed configuration. It can be seen that the substrate is clearly indented by the blister pressure.

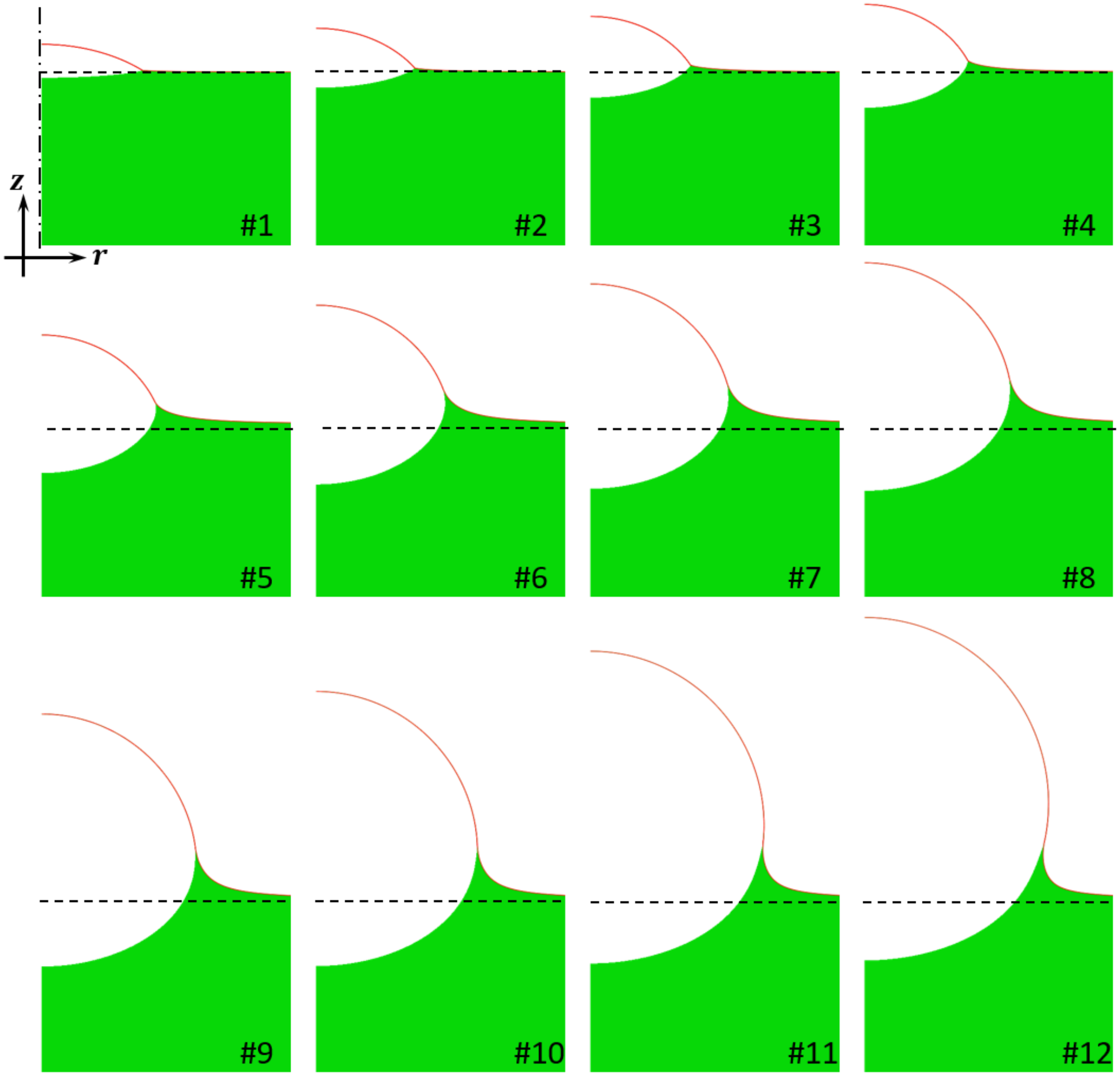

Figure 4.6 Deformed configurations of a blister on soft substrate corresponding to the nine dots displayed in Figure 4.5. From frame 1 to frame 12, volume of the blister increases monotonically.

We use $h_s = -z_s(0)$ to denote the indentation depth of the substrate, which is the distance from the central point of the substrate surface to its initial position. However, as shown Figure 4.7, the indentation depth h_s does not show proportional relation with the blister pressure,. The maximum blister pressure was achieved at $V/V_0 = 1.20$, while at $V/V_0 = 2.47$, the deepest indentation was reached. For $1.20 < V/V_0 < 2.47$, blister pressure drops due to the weakening in the blister layer, whereas the indentation depth h_s keeps increasing. This observed weakening in the substrate is mainly due to the consideration of surface tension γ_{ls}, and the membrane force $N_r^- + \gamma_l$ exerted at contact line. At moderate blister volume, the substrate surface deforms into a curved surface with certain mean curvature H. When surface tension γ_{ls} is taken into account, the corresponding Laplacian pressure $2\gamma_{ls}H$ diminishes the applied blister pressure, and thus, strengthens the substrate. However, as the blister volume increases, the mean curvature H of deformed substrate surface decreases, so that the strengthen effect is weakened.

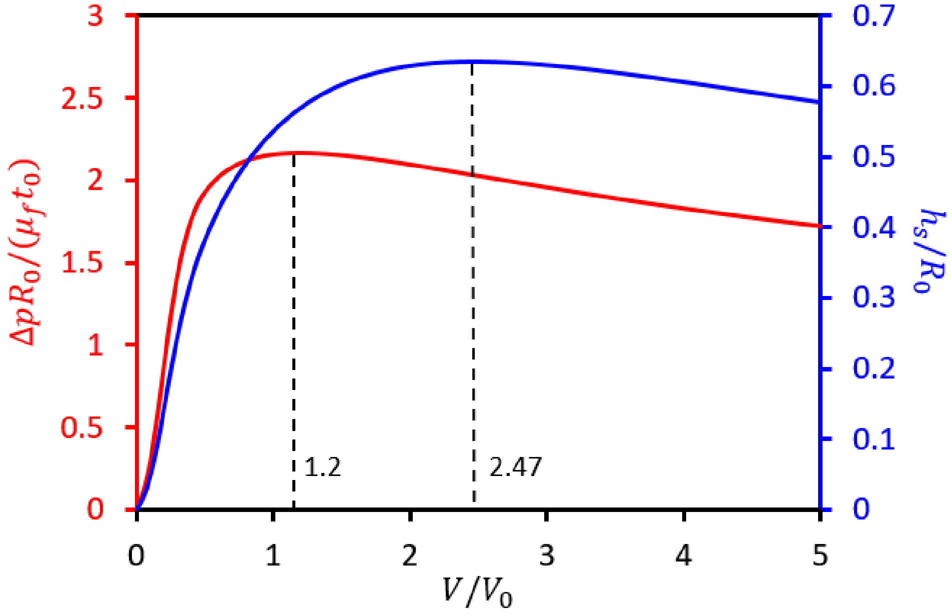

Figure 4.7 Normalized blister pressure (red) and substrate indentation depth (blue) v.s. normalized blister volume

When delamination propagation is considered, similar with the case of rigid substrate, we identity the deformed configuration of a blister with fixed initial radius $R_1 > R_0$, at which boundary conditions (Eqs. (4.51)~(4.53)) of delamination propagation are all satisfied, and consider it as the deformed configuration of a blister whose delamination radius propagates from R_0 to R_1. Figure 4.8 shows the computed results of normalized blister pressure, aspect ratio and contact angle, at $\gamma_l = \gamma_{ls} = 0.5\mu_f t_0$, $\Delta\gamma = 0$, and $\mu_s R_0/\mu_f t_0 = 2$. Black curves represent results of a blister when delamination propagation does not occur, while red curves are results when delamination propagates. Dashed curves are results for rigid substrates with the critical point of delamination propagation denoted by a solid blue square, and were obtained by using shooting method. Solid black solid curves were finite element results of a blister with initial radius R_0 and the corresponding critical point of delamination propagation is denoted by a solid blue diamond. Results of blisters with delamination propagation were obtained by building 6 blister with initial radii R_1 varying from 1.2 R_0 to 2.2 R_0 and identifying their critical configuration of delamination propagation. The corresponding results are denoted by hollow circles in Figure 4.8.

Unlike blisters on rigid substrates, when delamination propagates, the dimensionless parameters $V(\varDelta p/\mu_f t_0)^3$ is no longer constant due to the existence of the dimensionless parameter $\mu_s R_0/\mu_f t_0$, i.e. the effect of substrate deformation. However, the solid red curve in Figure 4.8a, which was produced by using $V(\varDelta p/\mu_f t_0)^3 = const$, and it still agrees well with finite element results, indicating that the effect of $\mu_s R_0/\mu_f t_0$ on $V(\varDelta p/\mu_f t_0)^3$ is relatively small at $\mu_s R_0/\mu_f t_0 = 2$ and therefore, can be neglected. It is also worth noting that results predicted by the relation $V(\varDelta p/\mu_f t_0)^3 = const$ are always smaller compared to finite element results. Besides, when delamination propagate, instead

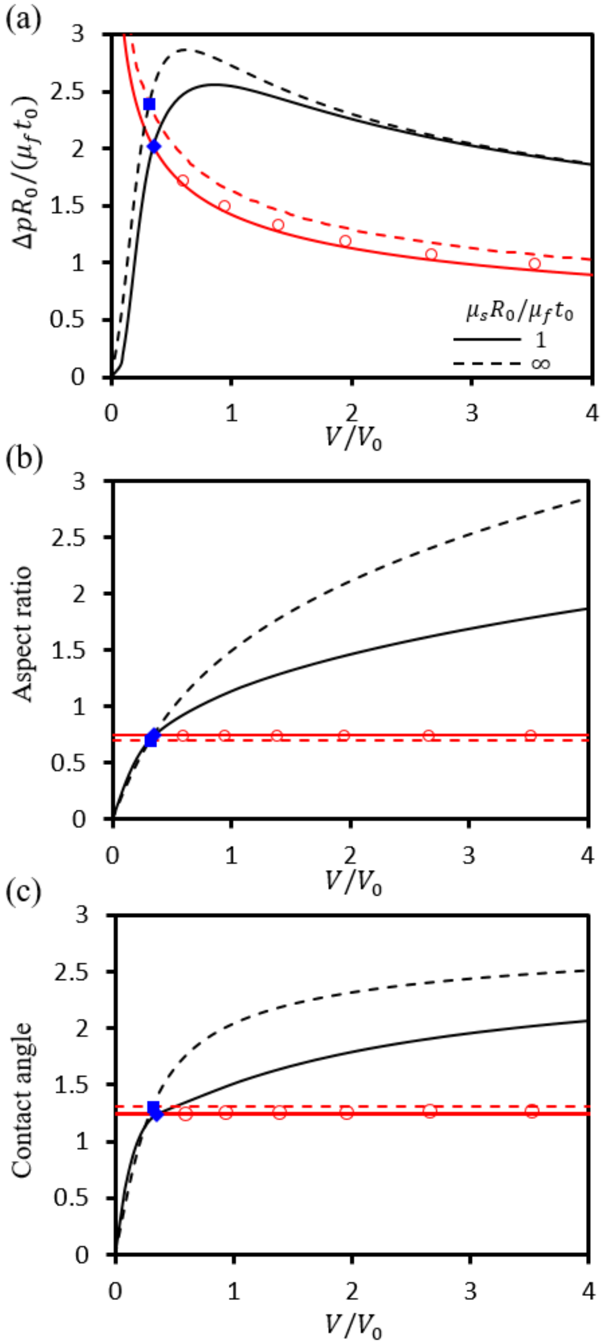

Figure 4.8 Computed (a) pressure-volume, (b) contact angle-volume, and (c) central deflection-volume relations with $\gamma_l = \gamma_{ls} = 0.5\mu_f t_0$, $\Delta\gamma = 0$, and $\mu_s R_0/\mu_f t_0 = 2$. Solid and dashed curves are results for soft and rigid substrates, respectively

of being constant, the aspect ratio and the contact angle of the blister slightly increase as the blister volume grows.

Figure 4.9 shows the deformed configurations of blisters corresponding to the hollow circles shown in Figure 4.8, whose delamination radius propagates from R_0 to R_1. The dashed line in each frame represents the initial position of the substrate surface. The scale bar in the first frame indicates the length of R_0, which is applicable to all the other frames. According to Figure 4.9, the contact line advances as the blister volume grows. Since delamination propagation occurs, the contact line in each frame of Figure 4.9 corresponds to different material point. Also, both the substrate deformation and delamination propagation contribute to the advancement of the contact line. The corresponding location of the contact line is plotted against the normalized blister volume in Figure 4.10. The black and red curves represent results without and with delamination propagation, respectively, and the intersected point is denoted by a blue dot which represents the critical point that delamination propagation sets in. According to Figure 4.10, once delamination propagation occurs, the contact line advances further compared to the configuration without delamination propagation.

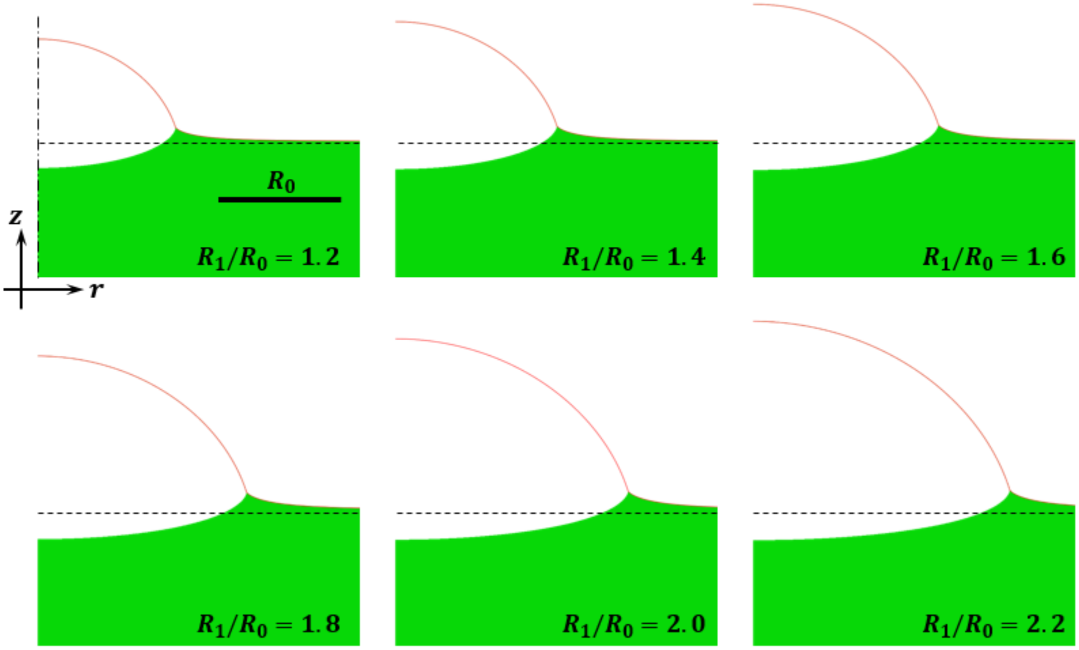

Figure 4.9 Deformed configurations of a blister on soft substrate when delamination propagation occurs. Each frame corresponds to the blister whose delamination radius propagates from R_0 to R_1 in undeformed configuration

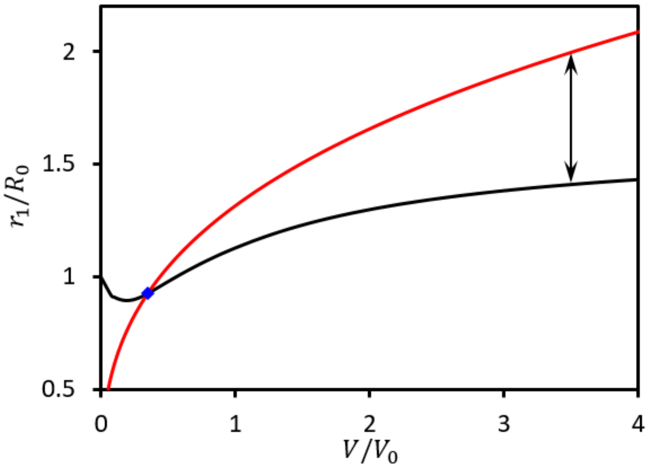

Figure 4.10 Normalized location of the contact line r_1/R_0 v.s. normalized blister volume of a blister on a soft substrate with $\gamma_l = \gamma_{ls} = 0.5\mu_f t_0$, $\Delta\gamma = 0$, and $\mu_s R_0/\mu_f t_0 = 2$. The blue dot denotes the critical point at which delamination propagation sets in. Black and red curves correspond to results without and with delamination propagation, respectively

Chapter 5 Droplets on Soft Substrates

Liquid droplet wetting soft substrate is studied in this chapter using the finite element method developed in Chapter 4 by simply setting $\mu_f t_0 \to 0$. In addition, by applying linearization, the boundary value problem in the linear elastic regime is established. Corresponding analytical solutions using linear elasticity are obtained when $\gamma_{ls} = \gamma_s$, i.e. Young's contact angle is $\pi/2$. General situations at $\gamma_{ls} \neq \gamma_s$ are solved using finite element method. Linear analytical and numerical results, and nonlinear numerical results are compared with available experimental measurements in the literature. Good agreement between the two validates my nonlinear models.

5.1 PROBLEM DESCRIPTION

By neglecting the out-of-plane deformation of the substrate, Young analyzed the equilibrium angle of a three-phase contact line of a droplet resting on flat substrate [62]. Young's classic analysis shows the contact angle satisfies the Young's equation (Eq. (3.73)). However, when the capillary length scale γ_l/μ_s is comparable with the droplet size, the out-of-plane deformation of the substrate is no longer negligible, and the shapes of both the substrate and the liquid are determined by the elastic response to the capillary force (Figure 5.1). Due to the elasto-capillarity, cusps can be developed below the contact line as reported in [71-73].

By setting $\mu_f t_0 \rightarrow 0$, from the formulism in Chapter 4, we obtain the boundary value problem of a droplet wetting soft substrate. The governing equations are

$$\mathrm{div}_{\boldsymbol{x}}\boldsymbol{\sigma} = \boldsymbol{0}, \boldsymbol{\sigma} = \boldsymbol{\sigma}^T \quad \forall \boldsymbol{x} \in \boldsymbol{B}(\Omega) \tag{5.}$$

and the boundary conditions are

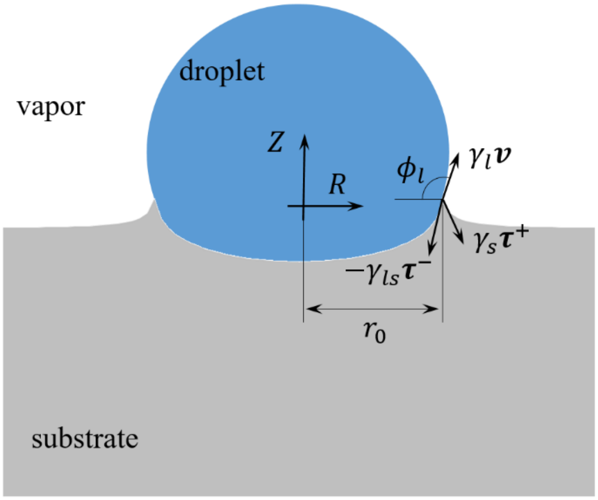

Figure 5.1 Schematic of a liquid droplet wetting soft substrate

$$\boldsymbol{\sigma}\cdot\boldsymbol{n}=\begin{cases}(2H\gamma_{ls}-\Delta p)\boldsymbol{n} & \forall\boldsymbol{x}\in\boldsymbol{B}(\Gamma_1^s)\\ 2H\gamma_s\boldsymbol{n} & \forall\boldsymbol{x}\in\boldsymbol{B}(\Gamma_2^s)\\ \gamma_l\delta(\boldsymbol{x}-\boldsymbol{x}_0)\boldsymbol{v} & \text{for } \boldsymbol{x}=\boldsymbol{x}_0\end{cases} \tag{5.1}$$

where γ_l now represents the surface tension of the liquid/vaper interface, $\boldsymbol{v}$ is the unit tangent vector along with the liquid/vaper interface at contact line as shown in Figure 5.1, i.e.

$$\boldsymbol{v}=-\cos\phi_l\,\boldsymbol{e}_r+\sin\phi_l\,\boldsymbol{e}_z \tag{5.2}$$

and all the other symbols maintain the same meanings as defined in Chapter 4. Also, at contact line, instead of Eq. (4.60), the force balance now is governed by the Neumann's triangle (or Neumann's law), i.e.

$$\gamma_l\boldsymbol{v}-\gamma_{ls}\boldsymbol{\tau}^-+\gamma_s\boldsymbol{\tau}^+=\boldsymbol{0} \tag{5.3}$$

Note that Neumann's triangle also holds for the contact line formed by three fluid phases. The reason it is applicable here is due to the constant surface energy density assumption we made in Chapter 4. Otherwise, for solids, the general Neumann's triangle should be written as [60]

$$\Upsilon_l\boldsymbol{v}-\Upsilon_{ls}\boldsymbol{\tau}^-+\Upsilon_s\boldsymbol{\tau}^+=\boldsymbol{0} \tag{5.4}$$

where Υ_i $(i=l,ls,s)$ and γ_i are connected through the Shuttleworth equation [61]. As $\mu_f t_0\to 0$, the solution of Eq. (4.57) yields $\Delta p=2\gamma_l\sin\phi_l/r_0$ which is the Laplacian pressure in the liquid droplet.

5.2 LINEAR ELASTICITY

In linear regime, using linear elasticity theory, analytical solutions and finite element model can be simplified . After linearization, the boundary value problem in Section 5.1 can be prescribed as the followings. The governing equations are

$$\begin{cases} (1-\nu)\left(\nabla^2 u_r - \dfrac{u_r}{r^2}\right) + \dfrac{\partial}{\partial r}(\nabla \cdot \boldsymbol{u}) = 0 \\ (1-2\nu)\nabla^2 u_z + \dfrac{\partial}{\partial z}(\nabla \cdot \boldsymbol{u}) = 0 \end{cases} \quad \forall \boldsymbol{x} \in \boldsymbol{B}(\Omega) \tag{5.5}$$

and boundary conditions at $z = 0$ are

$$\begin{cases} \sigma_{zz} = -\Delta p\, H(r_0 - r) + \dfrac{1}{r}\dfrac{\partial}{\partial r}\left(r \dfrac{\partial u_z}{\partial r}\right)\left(\gamma_{ls} H(r_0 - r) + \gamma_s H(r - r_0)\right) \\ \qquad + \gamma_l \sin\phi_Y\, \delta(r - r_0) \\ \sigma_{rz} = \gamma_l \cos\phi_Y\, \delta(r - r_0) \end{cases} \tag{5.6}$$

where

$r_0 =$ the radius of the circular contact line,

$H(r) =$ the Heaviside function of r,

$\phi_Y =$ the contact angle obtained from Young's law,

and isotropic constitutive relation is applied

$$\sigma_{ij} = \mu\left(u_{i,j} + u_{j,i} + \frac{2\nu}{1-2\nu} u_{k,k}\delta_{ij}\right) \tag{5.7}$$

Displacement components u_r, u_z, and stresses are functions of coordinates r and z. Note that under infinitesimal deformation, deformed and undeformed configurations are indistinguishable, so that instead of ϕ_l, ϕ_Y is imposed in Eq. (5.6). The Laplacian pressure Δp is directly given as $\Delta p = 2\gamma_l \sin\phi_Y / r_0$.

For substrates with infinite thickness or finite thickness, analytical solutions of Eqs. (5.5) and (5.6) are available when $\gamma_{ls} = \gamma_l$, i.e. $\phi_Y = \pi/2$. The details are included in Sections 5.2.1 and 5.2.2. In general case that $\gamma_{ls} \neq \gamma_l$, a finite element model is formulated in Section 5.2.3.

5.2.1 Droplet Wetting Elastic Half-Space

For an elastic half-space $\Omega = \{(r, z) | r \geq 0, z \leq 0\}$, the displacement field $\boldsymbol{u}(\boldsymbol{x})$ and surface traction $\boldsymbol{q}(\boldsymbol{x}_0)$ is connected by the surface Green function, $G_{ij}(\boldsymbol{x} - \boldsymbol{x}_0)$, which is defined as the x_i-component of displacement at $\boldsymbol{x}$ that is induced by a unit force applied at $\boldsymbol{x}_0$ on the surface along x_j direction. It can be obtained using double Fourier transform technique [74, 75]. When axisymmetry is taken into account, in the transformed space, the relation between displacement field $\hat{\boldsymbol{u}}(s, z)$ and the distributed surface traction $\hat{\boldsymbol{q}}(s)$ can be formulated as the following

$$\hat{\boldsymbol{u}}(s, z) = \begin{bmatrix} \hat{u}_r(s, z) \\ \hat{u}_z(s, z) \end{bmatrix} = \boldsymbol{G}(s, z)\boldsymbol{N}^{-1}(s)\hat{\boldsymbol{q}}(s) \tag{5.8}$$

where

$\hat{u}_r(s, z) = H_1\{u_r(r, z)\} =$ the 1st-order Hankel transform of u_r,

$\hat{u}_z(s, z) = H_0\{u_z(r, z)\} =$ the 0th-order of Hankel transform of u_z,

$\hat{\sigma}_{rz}(s, z) = H_1\{\sigma_{rz}(r, z)\} =$ the 1st-order Hankel transform of σ_{rz},

$\hat{\sigma}_{zz}(s, z) = H_0\{\sigma_{zz}(r, z)\} =$ the 0th-order of Hankel transform of σ_{zz},

$\boldsymbol{G}(s, z) = \frac{\mathrm{e}^{2\pi sz}}{16\pi s(1-\nu)\mu_s}\left((3 - 4\nu)\begin{bmatrix} 1 & 0 \\ 0 & 1 \end{bmatrix} + 2\pi sz\begin{bmatrix} 1 & 1 \\ -1 & 1 \end{bmatrix}\right)$,

$\boldsymbol{N}(s) = \frac{1}{2}\begin{bmatrix} 1 & 0 \\ 0 & 1 \end{bmatrix} - \frac{1-2\nu}{4(1-\nu)}\begin{bmatrix} 0 & 1 \\ 1 & 0 \end{bmatrix}$,

$\hat{\boldsymbol{q}}(s) = \begin{bmatrix} \hat{\sigma}_{rz}(s, 0) \\ \hat{\sigma}_{zz}(s, 0) \end{bmatrix}$.

The Hankel transform of order n of a function $f(r)$ is defined as

$$\hat{f}(s) = \int_0^\infty 2\pi r f(r) J_n(2\pi sr) dr \tag{5.9}$$

where J_n is the Bessel function of the first kind of n with $n \geq -1/2$. The inverse Hankel transform of $\hat{f}(s)$ is given as

$$f(r) = \int_0^\infty 2\pi s \hat{f}(s) J_n(2\pi sr) ds \tag{5.10}$$

When $\gamma_{ls} = \gamma_l$, i.e. $\phi_Y = \pi/2$, the traction force at $z = 0$ is

$$\begin{cases} \sigma_{zz} = \gamma_s \dfrac{1}{r}\dfrac{\partial}{\partial r}\left(r\dfrac{\partial u_z}{\partial r}\right) + \gamma_l \delta(r - r_0) - \dfrac{2\gamma_l}{r_0} H(r_0^- - r) \\ \sigma_{rz} = 0 \end{cases} \tag{5.11}$$

so that in the transformed space, the consequent $\hat{\boldsymbol{q}}(s)$ can be written as

$$\hat{\boldsymbol{q}}(s) = -2\pi \begin{bmatrix} 0 \\ 2\pi s^2 \hat{u}_z(s,0)\gamma_s + r_0 \gamma_l J_2(2\pi r_0 s) \end{bmatrix} \tag{5.12}$$

Substituting Eq. (5.12) into Eq. (5.8) yields [76]

$$\begin{cases} \bar{u}_r(\bar{r}) = -\dfrac{(1-2\nu)\gamma_l}{2\mu_s r_0} g_{r1}(\bar{r}, c) \\ \bar{u}_z(\bar{r}) = -\dfrac{(1-\nu)\gamma_l}{\mu_s r_0} g_{z1}(\bar{r}, c) \end{cases} s \tag{5.13}$$

where $\bar{r} = r/r_0$, $\bar{u}_r(\bar{r}) = u_r(r,h)/r_0$, $\bar{u}_z(\bar{r}) = u_z(r,h)/r_0$, and

$$\begin{gathered} c = \frac{\mu_s r_0}{(1-\nu)\gamma_s} \\ g_{r1}(\bar{r}, c) = \int_0^\infty \frac{J_2(\bar{s}) J_1(\bar{r}\bar{s}) d\bar{s}}{\bar{s}/c + 1} \\ g_{z1}(\bar{r}, c) = \int_0^\infty \frac{J_2(\bar{s}) J_0(\bar{r}\bar{s}) d\bar{s}}{\bar{s}/c + 1} \end{gathered} \tag{5.14}$$

which shares the same form with the result derived by Style and Dufresne [76].

5.2.2 Droplet Wetting Finite-Thickness Elastic Substrate

For an elastic substrate that has finite thickness, e.g. $\Omega = \{(r,z)|r \geq 0, -h \leq z \leq h\}$, with rigid boundary conditions $\boldsymbol{u}(r, -h) = \boldsymbol{0}$ on the bottom, and traction boundary condition $\boldsymbol{\sigma}(r,h) \cdot \boldsymbol{n} = \boldsymbol{q}(r)$ on the top, the resulted displacement filed in the transformed space can be expressed as

$$\hat{\boldsymbol{u}}(s,z) = \begin{bmatrix} \hat{u}_r(s,z) \\ \hat{u}_z(s,z) \end{bmatrix} = \left(\boldsymbol{G}_1(s,z)\boldsymbol{N}_1^{-1}(s) + \boldsymbol{G}_2(s, z+h)\boldsymbol{N}_2^{-1}(s)\right)\hat{\boldsymbol{q}}(s) \tag{5.15}$$

where

$$\begin{aligned} \boldsymbol{G}_1(s,z) &= \frac{\mathrm{e}^{2\pi s(z-h)}}{16\pi s(1-\nu)\mu_s}\left((3-4\nu)\begin{bmatrix} 1 & 0 \\ 0 & 1 \end{bmatrix} + 2\pi s(z-h)\begin{bmatrix} 1 & 1 \\ -1 & -1 \end{bmatrix}\right), \\ \boldsymbol{G}_2(s,z) &= \frac{\mathrm{e}^{-2\pi s(z+h)}}{16\pi s(1-\nu)\mu_s}\left((3-4\nu)\begin{bmatrix} 1 & 0 \\ 0 & 1 \end{bmatrix} - 2\pi s(z+h)\begin{bmatrix} 1 & -1 \\ 1 & -1 \end{bmatrix}\right), \end{aligned} \tag{5.16}$$

$$\begin{aligned}\boldsymbol{N}_1(s) &= \tfrac{1+\mathrm{e}^{-8\pi hs}}{2}\begin{bmatrix}1 & 0\\ 0 & 1\end{bmatrix} - \tfrac{(1-2\nu)(1-\mathrm{e}^{-8\pi hs})}{4(1-\nu)}\begin{bmatrix}0 & 1\\ 1 & 0\end{bmatrix}\\ &+\tfrac{\pi hs\mathrm{e}^{-8\pi hs}}{1-\nu}\left(\begin{bmatrix}-1 & 1\\ -1 & 1\end{bmatrix} + \tfrac{1}{3-4\nu}\begin{bmatrix}-1 & -1\\ 1 & 1\end{bmatrix} + \tfrac{8\pi hs}{3-4\nu}\begin{bmatrix}1 & 1\\ 1 & 1\end{bmatrix}\right),\\ \boldsymbol{N}_2(s) &= \cosh(4\pi hs)\left(\tfrac{2\pi hs}{1-\nu}\begin{bmatrix}0 & -1\\ 1 & 0\end{bmatrix} - \begin{bmatrix}1 & 0\\ 0 & 1\end{bmatrix}\right)\\ &+\sinh(4\pi hs)\left(\tfrac{2\pi hs}{1-\nu}\begin{bmatrix}-1 & 0\\ 0 & 1\end{bmatrix} + \tfrac{1-2\nu}{2(1-\nu)}\begin{bmatrix}0 & 1\\ 1 & 0\end{bmatrix}\right).\end{aligned}$$

Still consider $\phi_Y = \pi/2$ so that $\hat{\boldsymbol{t}}(s)$ is given by Eq. (5.12). Inserting Eq. (5.12) into Eq. (5.15) produces

$$\begin{cases}\bar{u}_r(\bar{r}) = -\dfrac{(1-2\nu)\gamma_l}{2\mu_s r_0}\displaystyle\int_0^\infty \dfrac{J_2(\bar{s})J_1(\bar{r}\bar{s})d\bar{s}}{f_{r1}(\bar{s},\tilde{r}_0)/c + f_{r2}(\bar{s},\tilde{r}_0)}\\ \bar{u}_z(\bar{r}) = -\dfrac{(1-\nu)\gamma_l}{\mu_s r_0}\displaystyle\int_0^\infty \dfrac{J_2(\bar{s})J_0(\bar{r}\bar{s})d\bar{s}}{\bar{s}/c + f_z(\bar{s},\tilde{r}_0)}\end{cases} \tag{5.17}$$

where $\tilde{r}_0 = r_0/h$, and

$$\begin{aligned} f_{r1}(\bar{s},\tilde{r}_0) &= \frac{\bar{s}\tilde{r}_0(1-2\nu)\left[4\bar{s} - \tilde{r}_0(3-4\nu)\sinh\frac{4\bar{s}}{\tilde{r}_0}\right]}{8\bar{s}^2 + \tilde{r}_0^2(1-2\nu)(3-4\nu)\left(1-\cosh\frac{4\bar{s}}{\tilde{r}_0}\right)}\\ f_{r2}(\bar{s},\tilde{r}_0) &= 1 - \frac{8(1-\nu)[(1-2\nu)(1-\nu)\tilde{r}_0^2 + 2\bar{s}^2]}{8\bar{s}^2 + \tilde{r}_0^2(1-2\nu)(3-4\nu)\left(1-\cosh\frac{4\bar{s}}{\tilde{r}_0}\right)}\\ f_z(\bar{s},\tilde{r}_0) &= \frac{-(5-12\nu+8\nu^2)\tilde{r}_0^2 - 8\bar{s}^2 - \tilde{r}_0^2(3-4\nu)\cosh\frac{4\bar{s}}{\tilde{r}_0}}{4\bar{s}\tilde{r}_0 - \tilde{r}_0^2(3-4\nu)\sinh\frac{4\bar{s}}{\tilde{r}_0}}\end{aligned} \tag{5.18}$$

It can be shown that as $\tilde{r}_0 \to 0$, i.e. $h \to \infty$, we have $f_{r1} \to s, f_{r2} \to 1$ and $f_z \to 1$, so that the Eq. (5.17) decays to Eq. (5.13), which indicates that the solution of finite-thick substrate recovers the solution of infinite-thick substrate as $h \to 0$.

5.2.3 Finite Element Model

Surface tension of the liquid/substrate interface is in general different from that of the vapor/substrate interface, i.e. $\gamma_{ls} \neq \gamma_s$ and $\phi_Y \neq \pi/2$. For this situation, methods used in Sections 5.1.1 and 5.1.2 are still applicable but results would be rather complicated. A finite element model is constructed in this section.

Following the process given in Hughes' book [77], the weak form of a droplet wetting an elastic substrate is found to be

$$a(\boldsymbol{w},\boldsymbol{u}) = (\boldsymbol{w},\boldsymbol{b}) + (\boldsymbol{w},\boldsymbol{q})_\Gamma \tag{5.19}$$

where $\boldsymbol{w}$ is the testing function, $\boldsymbol{b}$ is the body force, $\boldsymbol{q}$ remains the surface traction, and

$$\begin{gathered} a(\boldsymbol{w},\boldsymbol{u}) = \int w_{i,j}\sigma_{ij}d\Omega \\ (\boldsymbol{w},\boldsymbol{b}) = \int w_i b_i d\Omega \\ (\boldsymbol{w},\boldsymbol{q})_\Gamma = \sum_{i=1}^{3}\int w_i q_i d\,\Gamma_i^q \end{gathered} \tag{5.20}$$

where Γ_i^q represents the traction boundary involving q_i.

The corresponding discretization of Eq. (5.19) can be derived following the details in [77] , and won't be listed here. Instead, we focus on the contribution to the stiffness matrix due to surface tension. In Eq. (5.19), the only part that involves surface tension is

$$\begin{aligned} (\boldsymbol{w},\boldsymbol{q})_{\Gamma^s} = &\int_{\Gamma_1^s} w_i(\sigma_{ij}n_j)dA + \int_{\Gamma_2^s} w_i(\sigma_{ij}n_j)dA - w_r(r_0)\gamma_l\cos\phi_Y\, r_0 \\ &+ w_z(r_0)\gamma_l\sin\phi_Y\, r_0 \end{aligned} \tag{5.21}$$

where Γ^s denotes the substrate surface at $z = 0$, and Γ_1^s and Γ_2^s represent the liquid/substrate and vapor/substrate interfaces, respectively. Plugging Eq. (5.6) into Eq. (5.21), one obtains

$$\begin{aligned} (\boldsymbol{w},\boldsymbol{q})_{\Gamma^s} = &-\int_0^{r_0} w_z\Delta p r dr + \int_0^{r_0}(w_z\gamma_{ls}\nabla_\Gamma^2 u_z)rdr + \int_{r_0}^{\infty}(w_z\gamma_s\nabla_\Gamma^2 u_z)rdr \\ &- w_r(r_0)\gamma_l\cos\phi_l\, r_0 + w_z(r_0)\gamma_l\sin\phi_l\, r_0 \end{aligned} \tag{5.22}$$

where ∇_Γ^2 denotes the in-plane Laplacian operator, i.e.

$$\nabla_\Gamma^2 = \frac{\partial^2}{\partial r^2} + \frac{1}{r}\frac{\partial}{\partial r} \tag{5.23}$$

Note that, under infinitesimal deformation, one has

$$\left.\frac{\partial u_z}{\partial r}\right|_{r_0^-} \approx 0, \left.\frac{\partial u_z}{\partial r}\right|_{r_0^+} \approx 0 \tag{5.24}$$

so that

$$\begin{aligned}\int_0^{r_0}(w_z\gamma_{ls}\nabla_\Gamma^2 u_z)rdr &= -\gamma_{ls}\int_0^{r_0} r\frac{\partial w_z}{\partial r}\frac{\partial u_z}{\partial r}dr\\ \int_{r_0}^{\infty}(w_z\gamma_s\nabla_\Gamma^2 u_z)rdr &= -\gamma_s\int_{r_0}^{\infty} r\frac{\partial w_z}{\partial r}\frac{\partial u_z}{\partial r}dr\end{aligned} \tag{5.25}$$

Considering $w_z \to 0$ as $r \to \infty$, by substituting Eq. (5.25) into Eq. (5.21), $(\boldsymbol{w},\boldsymbol{q})_{\Gamma^s}$ can be rewritten in the following form

$$\begin{aligned}(\boldsymbol{w},\boldsymbol{q})_{\Gamma^s} = &-\int_0^{r_0} w_z\Delta p r dr - w_r(r_0)\gamma_l\cos\phi_Y\, r_0 + w_z(r_0)\gamma_l\sin\phi_Y\, r_0\\ &-\gamma_{ls}\int_0^{r_0} r\frac{\partial w_z}{\partial r}\frac{\partial u_z}{\partial r}dr - \gamma_s\int_{r_0}^{\infty} r\frac{\partial w_z}{\partial r}\frac{\partial u_z}{\partial r}dr\end{aligned} \tag{5.26}$$

After discretization, the first three terms on the right hand side of Eq. (5.26) go to residual force vector while the last two integrals set in stiffness matrix. In a four-node quadrilateral element (see Figure 5.1) with shape functions

$$\begin{aligned}N^1 &= \frac{1}{4}(1-\xi)(1-\eta), N^2 = \frac{1}{4}(1+\xi)(1-\eta),\\ N^3 &= \frac{1}{4}(1+\xi)(1+\eta), N^4 = \frac{1}{4}(1-\xi)(1+\eta)\end{aligned} \tag{5.27}$$

where $-1 \le \xi \le 1$ and $-1 \le \eta \le 1$, the position vector $\boldsymbol{r}$, displacement vectore $\boldsymbol{u}$ and the testing vector $\boldsymbol{w}$ for points over the element may be parametrized by (ξ,η) as

$$\begin{aligned}\boldsymbol{r}(\xi,\eta) &= \boldsymbol{N}(\xi,\eta)[r^e]^T = \boldsymbol{N}(\xi,\eta)[r_1\ z_1\ r_2\ z_2\ r_3\ z_3\ r_4\ z_4]^T\\ \boldsymbol{u}(\xi,\eta) &= \boldsymbol{N}(\xi,\eta)[u^e]^T = \boldsymbol{N}(\xi,\eta)[u_r^1\ u_z^1\ u_r^2\ u_z^2\ u_r^3\ u_z^3\ u_r^4\ u_z^4]^T\\ \boldsymbol{w}(\xi,\eta) &= \boldsymbol{N}(\xi,\eta)[w^e]^T = \boldsymbol{N}(\xi,\eta)[w_r^1\ w_z^1\ w_r^2\ w_z^2\ w_r^3\ w_z^3\ w_r^4\ w_z^4]^T\end{aligned} \tag{5.28}$$

where $(r_A,\ z_A)$, $(u_r^A,\ u_z^A)$, and $(w_r^A,\ w_z^A)$ $(A = 1,2,3,4)$ are the nodal value of positions, displacements, and testing functions, respectively, and $\boldsymbol{N}(\xi,\eta)$ is the matrix of shape function, i.e.

$$\boldsymbol{N}(\xi,\eta) = \begin{bmatrix} N_1 & 0 & N_2 & 0 & N_3 & 0 & N_4 & 0\\ 0 & N_1 & 0 & N_2 & 0 & N_3 & 0 & N_4\end{bmatrix} \tag{5.29}$$

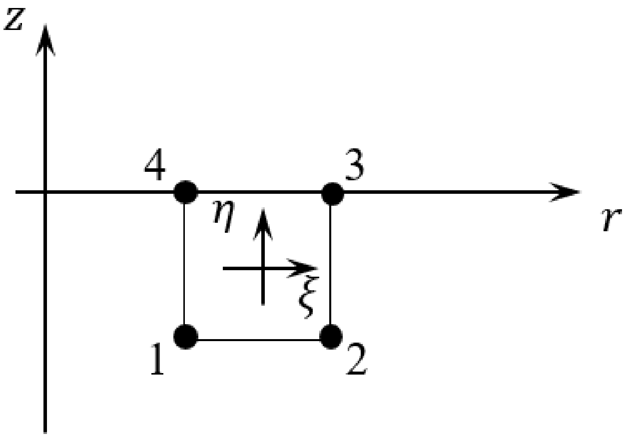

Figure 5.2 Schematic of a quadrilateral element on substrate surface

Also, on face 4-3, we have

$$\eta = 1 \text{ and } r = \frac{r_4 - r_3}{2}\xi + \frac{r_4 + r_3}{2} \tag{5.30}$$

If the element face formed by nodes 3 and 4 coincides with the substrate surface (Figure 5.2), for this particular element, the integral in Eq. (5.26) that involves surface tension can be written as

$$\begin{aligned}
&\int_{r_4}^{r_3} r\frac{\partial w_z}{\partial r}\frac{\partial u_z}{\partial r}dr = \int_{r_4}^{r_3} r\frac{\partial w_z^A N_A}{\partial r}\frac{\partial u_z^B N_B}{\partial r}dr \\
&= \int_{r_4}^{r_3} r w_z^A u_z^B \frac{\partial N_A}{\partial r}\frac{\partial N_B}{\partial r}dr \\
&= w_z^A \int_{-1}^{1}\left(\frac{r_4 - r_3}{2}\xi + \frac{r_4 + r_3}{2}\right)\frac{\partial \xi}{\partial r}\frac{\partial N_A(\xi,1)}{\partial \xi}\frac{\partial N_B(\xi,1)}{\partial \xi}d\xi\, u_z^B \\
&= [w^e]^T\left[k_\gamma^e\right][u^e]
\end{aligned} \tag{5.31}$$

where

$$\left[k_\gamma^e\right] = \frac{r_4 + r_3}{2(r_4 - r_3)}\begin{bmatrix} 0 & 0 & 0 & 0 & 0 & 0 & 0 & 0 \\ 0 & 0 & 0 & 0 & 0 & 0 & 0 & 0 \\ 0 & 0 & 0 & 0 & 0 & 0 & 0 & 0 \\ 0 & 0 & 0 & 0 & 0 & 0 & 0 & 0 \\ 0 & 0 & 0 & 0 & 0 & 0 & 0 & 0 \\ 0 & 0 & 0 & 0 & 0 & 1 & 0 & -1 \\ 0 & 0 & 0 & 0 & 0 & 0 & 0 & 0 \\ 0 & 0 & 0 & 0 & 0 & -1 & 0 & 1 \end{bmatrix} \tag{5.32}$$

Thus, when computing the stiffness matrix $[k^e]$ over each element, if the element is located on substrate surface, we need to add $\left[k_\gamma^e\right]$ to $[k^e]$ i.e.

$$\begin{gathered} [k^e] \leftarrow [k^e] + \gamma_{ls}\left[k_\gamma^e\right] \text{ if } r_4 \le r_0 \\ [k^e] \leftarrow [k^e] + \gamma_s\left[k_\gamma^e\right] \text{ if } r_3 \ge r_0 \end{gathered} \tag{5.33}$$

5.3 HYPER ELASTICITY

A droplet wetting soft substrate is the limit case of the body fluid induced blisters when the stiffness of the blister layer goes to zero, i.e. $\mu_f t_0 \to 0$. Thus, similar with the solving routine prescribed in Section 4.2, the boundary problem (Eqs. (5.1)-(5.3)) can be solved following the flow chart given in Figure 5.3.

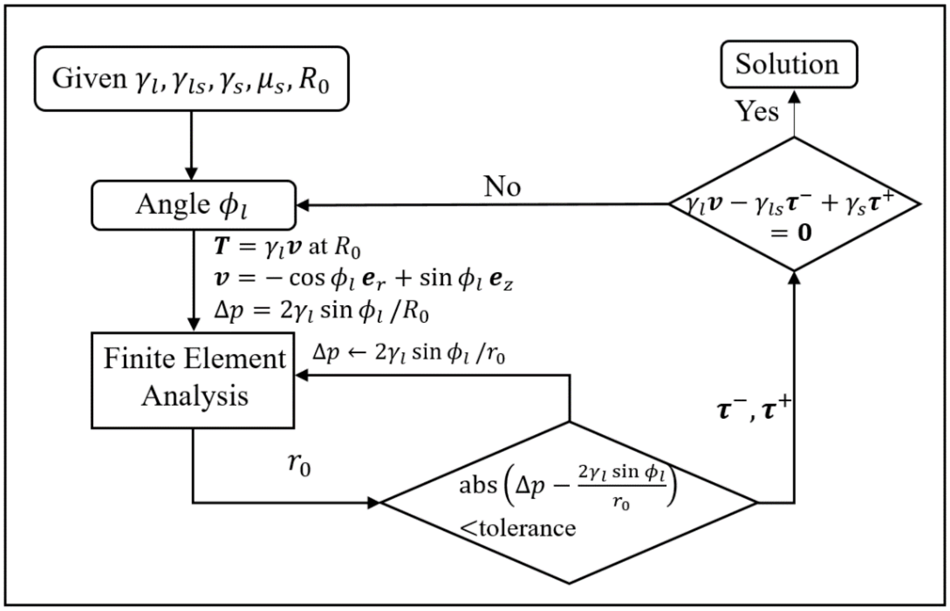

Figure 5.3 Flow chart for the solving routine of liquid droplet wetting soft substrate

5.4 RESULTS AND DISCUSSION

5.4.1 Linear Elasticity

In the case of a droplet wetting elastic substrate, when $\gamma_s = \gamma_{ls}$, according to Eqs. (5.13) and (5.17), displacement u_r and u_z linearly depend on γ_l/μ [76], and are also functions of $\gamma_s/(\mu_s r_0)$, as well as r_0/h when the substrate thickness is finite.

For infinite-thick substrate, Figure 5.4 plots the normalized displacement at $z = h$ with $c =$ 1, 10, 100 and 1000, and the out-of-plane displacement at contact line. According to Figure 5.4c, the height of the wetting ridge monotonically increases along with the increase of the dimensionless parameter c. In the analysis of Style and Dufresne [76], an asymptotically relation between $u_z(r_0, h)$ and c was given for $c \gg 1$, but with a typo. The correct relation is expressed as the following

$$\frac{u_z(r_0, h)\mu_s}{(1-\nu)\gamma_l} \approx \frac{\log c}{\pi^{1/4}} + const \tag{5.34}$$

where the power of π is 1/4, instead of 1. In Figure 5.4c, Eq. (5.*34*) is plotted without the constant term as the dashed curve.

For finite-thick substrate, Figure 5.5 displays the normalized displacement at $z = h$ with $\nu = 0.3$, $c = 10$ and $r_0/h =$ 0, 2 ,5 ,10, and the out-of-plane displacement at contact line. Here, $r_0/h =$ 0 represents infinite-thick substrate, i.e. $h \to \infty$. Due to the constrain $u_r = u_z = 0$ at $z = -h$ (bottom of the substrate), thinner substrate undergoes smaller out-of-plane deformation, as shown in Figure 5.5b. However, according to Figure 5.5c, height of the wetting ridge, i.e. the maximum out-of-plane displacement, is not sensitive to substrate thickness as only a small change is observed when the substrate thickness varies from infinity to 10% of the droplet size ($r_0/h =$ 10).

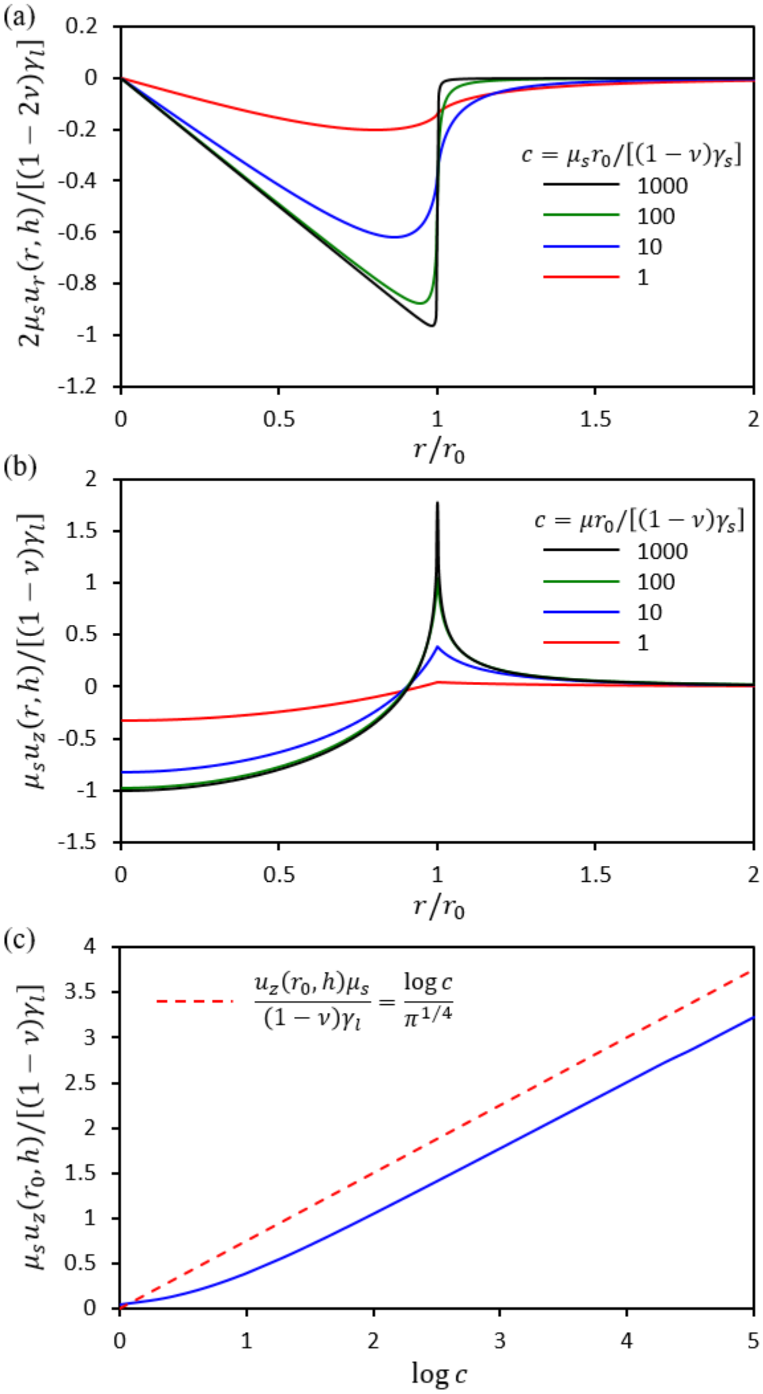

Figure 5.4 (a) and (b): deformation of the surface of an infinite-thick substrate with $c =$ 1, 10, 100, 1000. (c) The peak height of the wetting ridge (blue curve). The dashed curve plots the asymptote given by Eq. (5.34)

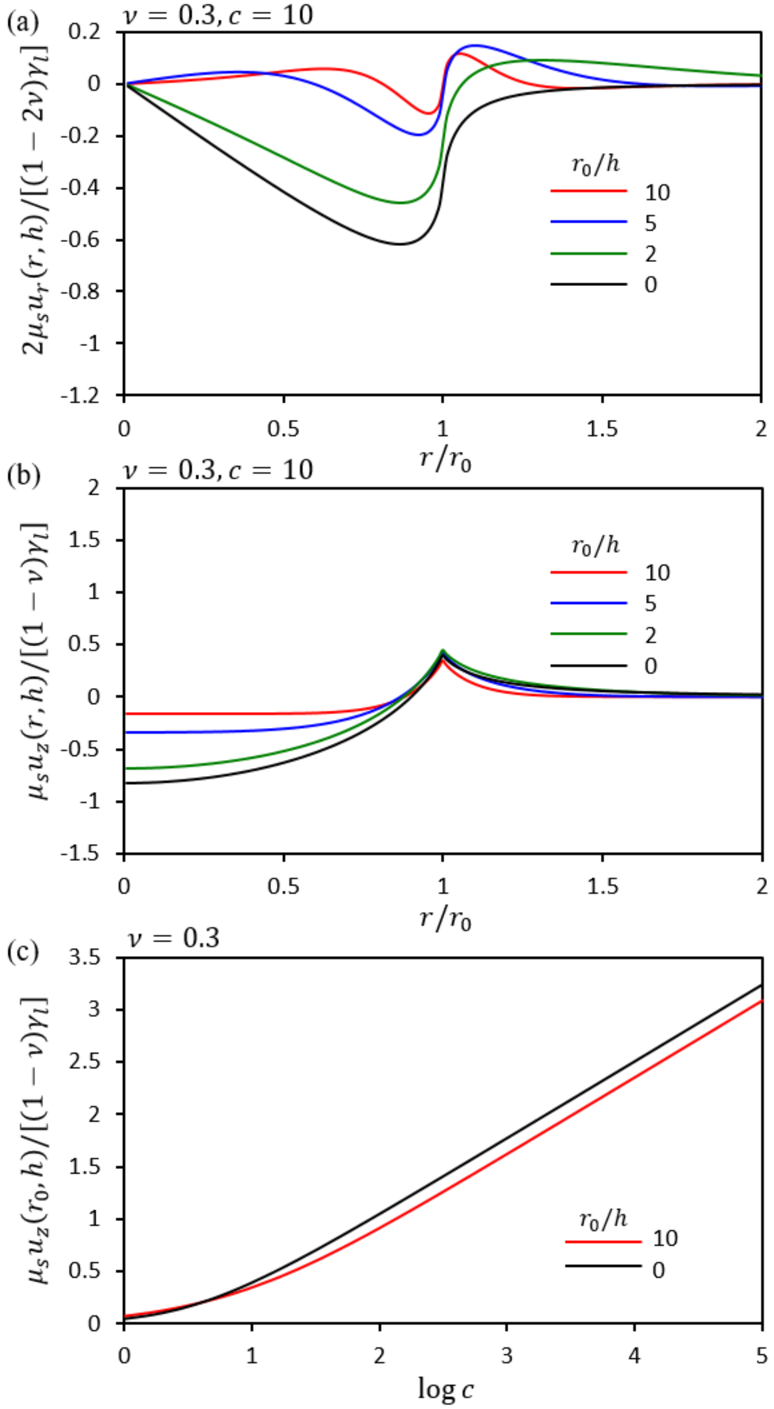

Figure 5.5 (a) and (b): deformation of the surface of a finite-thick substrate with $\nu = 0.3$, $c = 10$ and $r_0/h = 0, 2, 5, 10$. (c) The peak height of the wetting ridge for infinite-thick substrate (black) and finite-thick substrate (red).

Under linear elastic regime, a mixed formulation [77] was used in the linear finite element code described in Section 5.2.3, which is capable of representing both compressible ($\nu < 0.5$) and incompressible ($\nu = 0.5$) materials. The finite element simulation was first validated by comparing with analytical solutions at $\gamma_{ls} = \gamma_s$. To this end, we fixed $\nu = 0.5$, $r_0/h = 2$, and $\gamma_s/(\mu_s r_0) = 1$. when $\nu = 0.5$, the integrand in u_z (Eq. (5.17)) shows considerable oscillations and a double exponential oscillatory strategy [78] was applied to numerically obtain u_z. In both Figures 5.6a and 5.6b, the finite element results agree well with analytical results which validates our finite element code. At $r = r_0$, a slight fluctuation in u_r can be observed which is due to the different boundary conditions applied for $r < r_0$ and $r > r_0$. This fluctuation is sensitive to the mesh at contact line, and can be minimized by choosing smaller element size. Finite element results in Figure 5.6 correspond to element size $= 0.02r_0$. Figures 5.6c and 5.6d show contour plots of normalized displacement field obtained by using finite element simulation.

So far, analytical solutions are only available at $\gamma_{ls} = \gamma_s$ ($\phi_Y = \pi/2$) and they served as validations of our linear finite element method. Figure 5.6e shows finite element results of surface deflections at different ϕ_Y's. Note that under linear elastic regime, infinitesimal deformation is considered so that undeformed and deformed configurations are not differentiable. Therefore, though in deformed configuration contact line may advance of retract, the applied Laplacian extra pressure is fixed. Due to the same reason, surface tension γ_l is applied at contact line whose orientation does not depend on the shape of the wetting ridge. As a result, in deformed configuration, γ_l, γ_{ls} and γ_s may not satisfy the force balance relation at contact line (Eq. (5.3)).

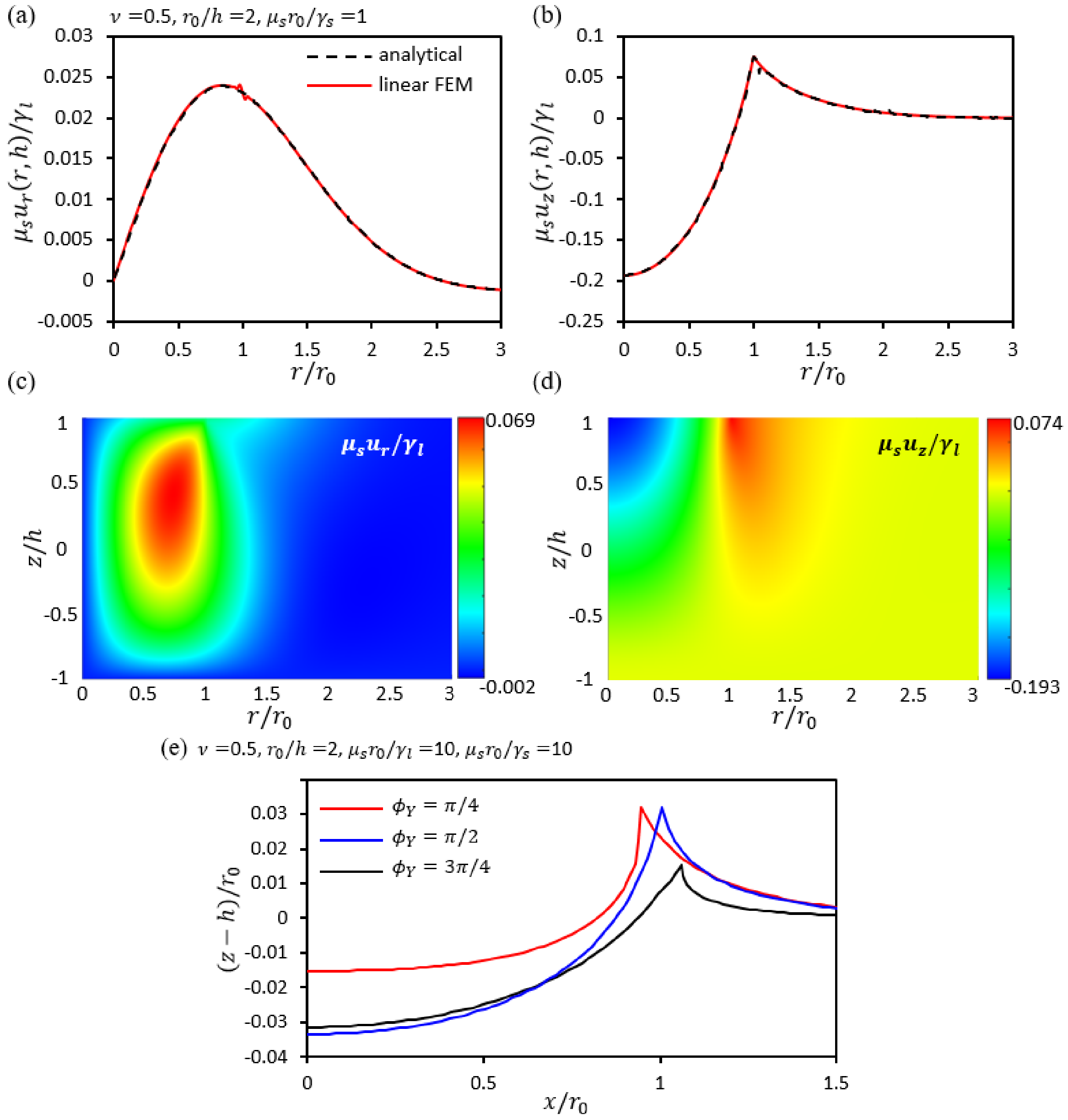

Figure 5.6 Computed (a) in-plane and (b) out-of-plane deformations of the surface of a finite-thick substrate with $\nu = 0.5$, $r_0/h = 2$, and $\mu_s r_0/\gamma_s = 1$. Analytical results are plotted as dashed black curves and finite element simulations as solid red curves. (c) & (d): contour plots of normalized displacement field obtained by using finite element method. (e) Finite element results of the deformed substrate surface with $\nu = 0.5$, $r_0/h = 2$, $\mu_s r_0/\gamma_s = \mu_s r_0/\gamma_l = 10$, and $\phi_Y = \pi/4, \ \pi/2, \ 3\pi/4$

5.4.2 Hyper Elasticity

Under hyper elasticity, large deformation is involved and we use (R, Z) and (r, z) to differentiate the spatial coordinates of a material point in undeformed and deformed configurations, respectively. R_0 is used to denote the droplet radius in undeformed status. The iterative method prescribed in Section 5.3 was applied in Abaqus to solve the B.V.P. given in Section 5.1. During each iteration, the position of the contact line, and the ridge shape are used to determine the Laplacian pressure and the orientation of surface tension γ_l for the next iteration, such that, at equilibrium, the Neumann's triangle (Eq. (5.3)) is satisfied. In Abaqus, the substrate was modeled as incompressible Neo-Hookean material and surface tension effect was implemented via a UEL[67-69].

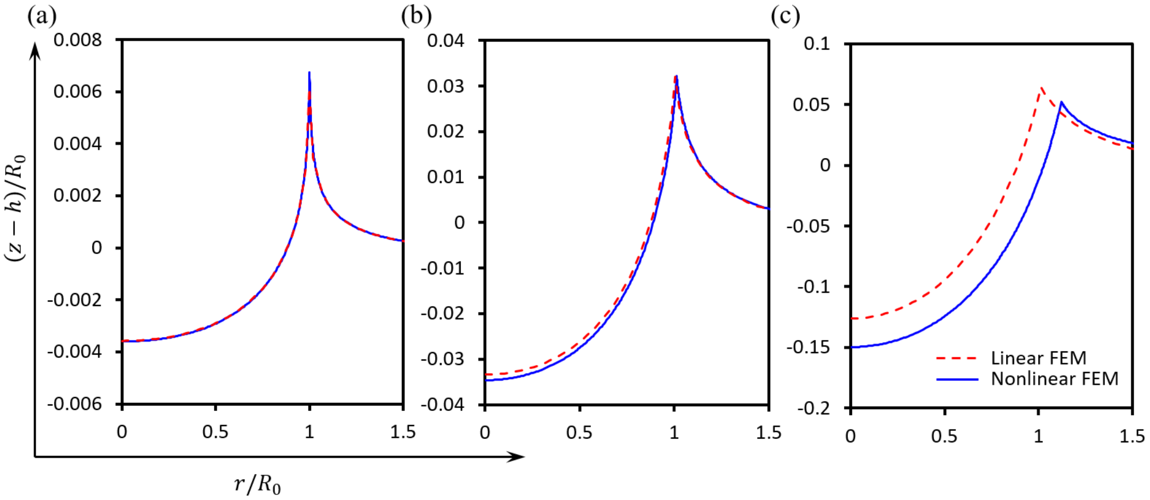

Figure 5.7 Normalized surface profiles of a substrate being wetted by droplets with $R_0/h = 2$. Results were computed by linear (dashed red curves; $\nu = 0.5$) and nonlinear (solid blue curves) finite element method (FEM) with (a)~(c): $\mu_s R_0/\gamma_l = \mu_s R_0/\gamma_s = \mu_s R_0/\gamma_{ls} =$ 0.01, 0.2 and 0.5

Figure 5.7 displays the normalized surface profiles of a substrate being wetted by droplets with $R_0/h = 2$. Results were computed by linear (dashed red curves; $\nu = 0.5$)

and nonlinear (solid blue curves) finite element method (FEM) with (a)~(c): $\mu_s R_0/\gamma_l = \mu_s R_0/\gamma_s = \mu_s R_0/\gamma_{ls} =$ 0.01, 0.2 and 0.5. According to Figure 5.7, under small surface tension ($\mu_s R_0/\gamma < 0.1$), nonlinear FEM produces the same results with linear FEM and we have $r_0 \approx R_0$. However, with large surface tension, e.g. $\mu_s R_0/\gamma \sim 0.5$, deformation of the wetting ridge is significant so that geometric and material nonlinearities become non-negligible. As a result, the contact line may advance or retract so that $r_0 \neq R_0$.

To validate the nonlinear FEM method, we compared the simulation results of wetting ridges with experimental measurements on various droplets/substrate combinations. In this area, researchers have developed different techniques to image the surface profile of wetting ridges, including confocal microcopy [73], optical profilometry [79], and X-ray microscopy [80]. In Figure 5.8, we adopted X-ray images of water droplets on a silicone gel (Figure 5.8a, Young's modulus $E =$ 3 kPa), and polydimethylsiloxane (PDMS) (Figure 5.8a, $E =$ 16 kPa) from [80], and confocal images of glycerol droplets on a silicone gel (Figure 5.8a, $E =$ 3 kPa) from [73]. Thickness of all substrates in Figures 5.8a~5.8c are ~50 μm. Radii of the droplets are measured to be (a)1 mm, (b) 1mm, and (c) (from left to right) 26.8, 74.5, 176.7, and 225.5 μm. Other parameters used in finite element simulations are all provided in the papers and are summarized in Table 5.1.

In Figures 5.8a and 5.8b, each computed profiles is translated by (x', z') so that the tip of the wetting ridge overlaps with the ridge tip from the image. We varied the substrate stiffness to look for best fitting results, and found that, in Figure 5.8a, $E = 6$ kPa (blue) can fit the ridge tip very well compared to the given $E =$ 3 kPa (black), while in Figure 5.8a, the given stiffness, $E = 16$ kPa (black), provides the best fitting. In general, the computed profiles of the wetting ridge agree well with the X-ray images, which validates of finite element methods in .

In Figures 5.8c and 5.8d, instead of the ridge tip, we look at the whole deformed surface of the substrate. Figure 5.8c are confocal profiles of a silicone gel substrate wetted by glycerol droplets with radii of 26.8, 74.5, 176.7, and 225.5 μm, whereas Figure 5.8d plots the corresponding nonlinear FEM results. Young's modulus of the substrate was measured to be $E = 3$ kPa, while the best fitting results were obtained at $E = 4.5$ kPa. Overall, the simulation profile is consistent with confocal measurements but with deviations at radus = 26.8 μm. The mismatch at small droplet size is due to the use of 26.8 μm, the droplet radius at deformed configuration (r_0), as droplet radius in undeformed configuration (R_0). In experiments, r_0 can be directly measured, whereas in simulations, R_0 is applied as one of the inputs. For large droplets, the misuse of r_0 causes only negligible difference in Laplacian pressure, so that the substrate deformation is not affected. However, for small droplets (e.g. $R_0 \sim 26.8\, \mu m$ for this case), replacing R_0 with r_0 induces considerable change in Laplacian pressure, leading to a deviation in substrate's surface profile. In addition, the incompressible Neo-Hookean law used in FEM may not be suitable to model the substrate material.

It has been found that the cusp shape of the wetting ridge is nearly independent with substrate stiffness or the ridge height [71, 73, 80]. With the parameters listed in Table 5.1, we also extracted the cusp angle, θ_s (see Figure 5.8a), of the wetting ridge for various droplet/substrate combinations. The computed θ_s's are plotted against experimental measurements in Figure 5.9. Again, the numerical and experimental results are in good agreement, which justify the use of our finite element strategy.

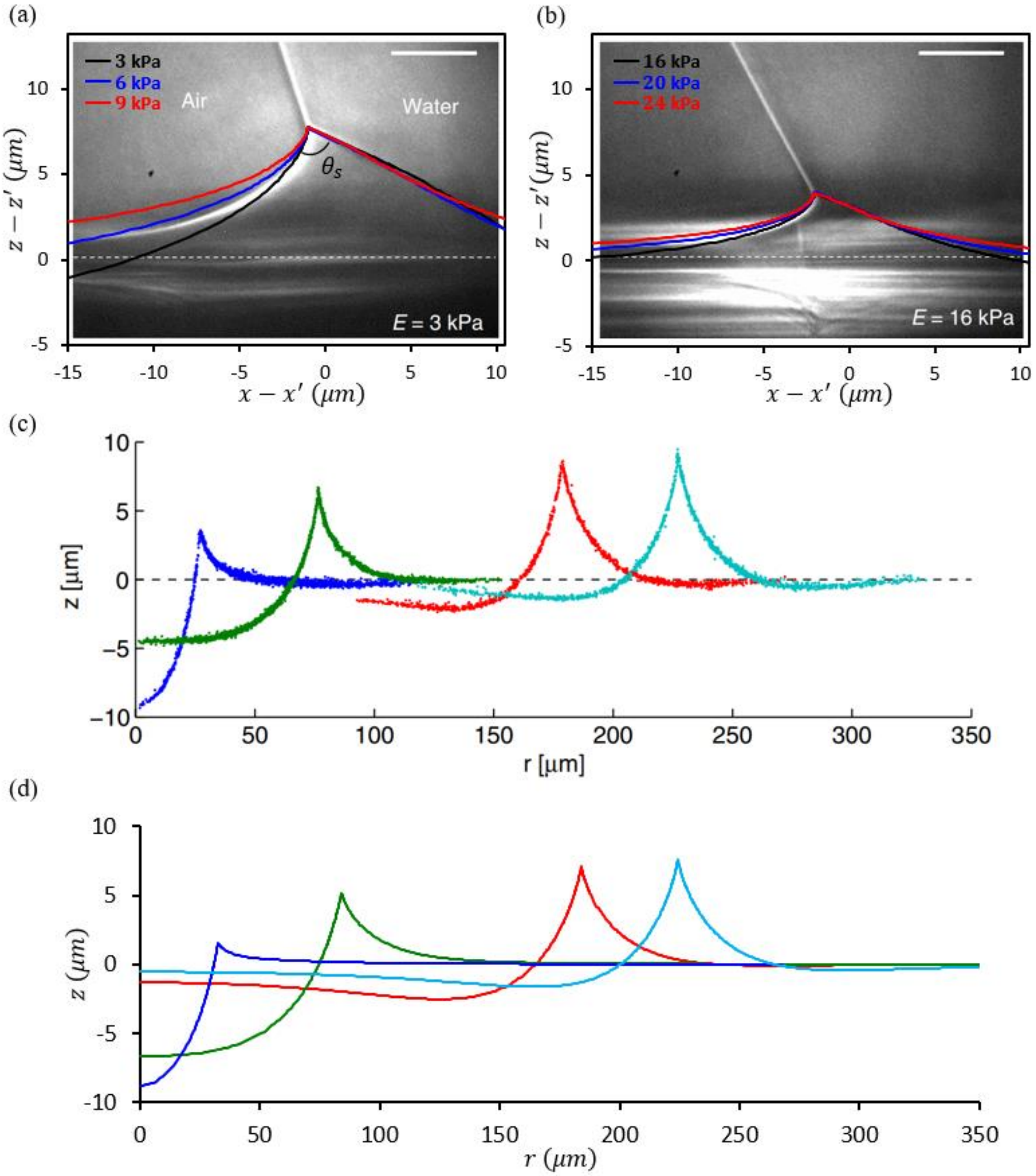

Figure 5.8 Comparisons of experimental measurements and nonlinear FEM results of the deformed wetting ridges for (a) water droplet on a silicone gel, (b) water droplet on a PDMS film, and (c) & (d) glycerol droplet on a silicone gel with (from left to right) radii of 26.8, 74.5, 176.7, and 225.5 μm. Scale bars in (a) and (b) represent 5 μm. Experimental images (a) and (b) are adopted with permissions from Ref. [80], and (c) from Ref. [73] Copyright (2013) by the American Physical Society.

	E (kPa)	R_0 (um)	Thickness (um)	γ_l (mN/m)	γ_s	γ_{ls}	ϕ_l (°)
water/pdms	16	1000	50	72	59	16	108.1
	20	1000	50	72	59	16	108.1
	24	1000	50	72	59	16	108.1
EG 40%/silicone gel	1.5	1000	50	58	42	23	92.3
	3	1000	50	58	42	23	92.3
	4.5	1000	50	58	42	23	92.3
glycerol/silicone gel	4.5	26.8	50	46	31	36	90
	4.5	74.5	50	46	31	36	90
	4.5	176.7	50	46	31	36	90
	4.5	225.5	50	46	31	36	90
glycerol/silicone gel flurinated-oil/silicone gel	3	200	23	17	28	16	40
	4.5	200	23	17	28	16	40
	6	200	23	17	28	16	40

Table 5.1 Parameters used in finite element simulations. Values for surface tension are all given with unit mN/m

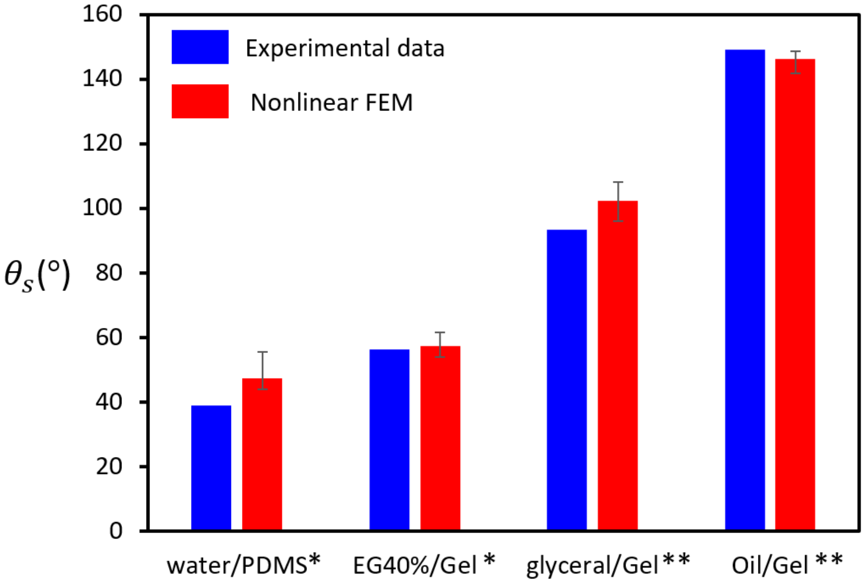

Figure 5.9 Summary of the micro angle θ_s of various droplet/substrate combinations obtained experimentally (blue) and numerically (red). "Gel" is short for "silicone gel" and its recipe is dependent on data resources

* from Ref. [80]
** from Ref. [73]

Chapter 6 Background and Motivations for Cratered Surfaces

This chapter discusses the background and motivations of for a cratered surface forming an interface with an unpatterned surface. Gecko-inspired dry adhesives have been widely studied but their adhesion is lost underwater and the large-aspect-ratio microfibrils are not robust enough for repeated use. Reversible adhesives with engineered surface craters have been reported with good reusability and strong adhesive strength under both dry and wet conditions. They are also capable of providing pressure-dependent adhesion. Mechanistic understanding of suction forces generated by cratered surfaces is pivotal for adhesion prediction as well as crater design.

6.1 BACKGROUND

Adhesives that can stick and unstick repeatedly are called reversible or reusable adhesives. Ideally, the temporary bounds formed by reusable adhesives can be removed without damaging or leaving any residues on the adherend. Commonly used adhesives include Post-it® notes and medical tapes. Reversible adhesives can also find many applications such as wall mounts, foot pads for robots, wafer handlers, and bio-integrated electronics [9, 81-86].

6.1.1 Gecko-inspired Reversible Adhesives

In nature, geckos are capable of running upside down because they are endowed with anatomic features functioning as reusable adhesives that, on the one hand, can support a large weight, and, on the other hand, allow for a quick and easy release. Experimental observations revealed that toe pads of geckos feature intricate hierarchical fibrillary structures as shown in Figure 6.1a. Those structures results in the adhesive strength close to 100 kPa [87, 88], which is comparable to that of a 3M scotch tape (200 kPa). A lot of progress has been made toward the fundamental understanding of the gecko fibrillary structure and it has been revealed that the adhesion of microfibrils come from van der Waals interactions [89, 90]. Contact mechanics has been applied to explain the enhanced adhesion when the fibril diameters decrease [91]. Extensive efforts have been made to produce gecko-inspired artificial microfibrils (Figure 6.1b) as reusable adhesives [92-94]. However, their adhesion strength is fixed once fabricated unless extra engineering is incorporated [95-97]. It’s also reported that wet surfaces or underwater environment may impair the performance of microfibrils-enabled adhesives [98-100]. Therefore, alternative mechanisms are required for reversible adhesives with tunable adhesion in air and underwater.

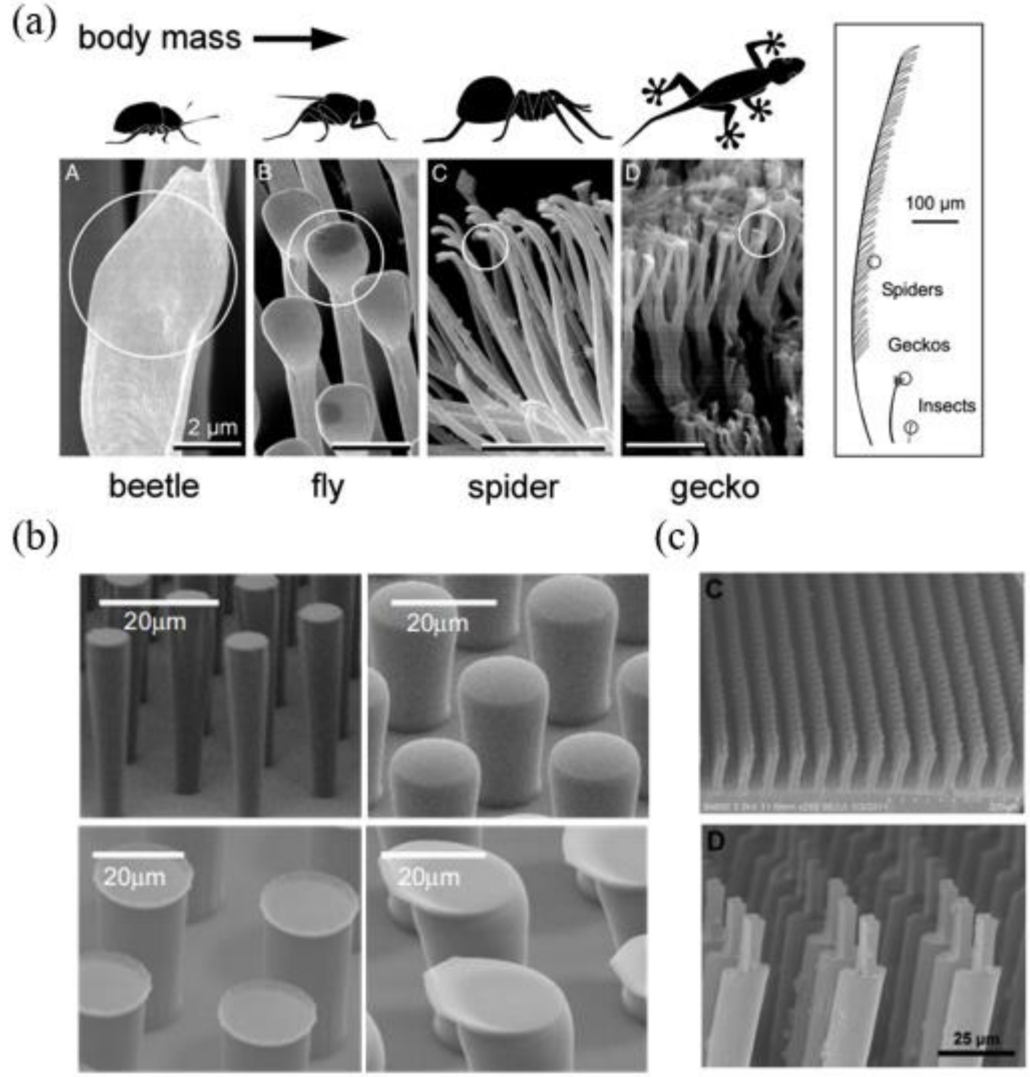

Figure 6.1 (a) Spatula-like terminal elements in insect, fly, spider and gecko (adopted with permission from Ref. [90], Copyright (2011) National Academy of Sciences). (b) & (c) Various designs of gecko-inspired artificial microfibrils used as reusable adhesives ((b) is adopted with permission from Ref. [101], Copyright (2007) Wiley-VCH Verlag GmbH & Co. KGaA; (c) is adopted with permission from Ref. [93], Copyright (2012) American Chemical Society)

6.1.2 Octopus-inspired Reversible Adhesives

While commercial use of engineered hierarchical fibrillary structures is at its infancy, low-cost fixtures in the form of suction cups have been widely used in numerous applications, such as wall/window-mounting suction hooks (Figure 6.2a) and skin-mounting suction electrodes. Adhesion of suction cups is enabled by vacuum generated inside the cup upon compressive loading and unloading, as inspired by octopus suckers. Similarly, adhesion can also be generated on cratered surfaces which are surfaces with engineered dimples (Figure 6.2b).

Both thin-walled structured suction cups and cratered surfaces are attractive since they combine high strength and quick release. However, under micro scale, implementation of suction cups requires the combination of concave geometries with fibrillary structures [86, 102], which involves expensive and labor-intensive fabrication process, whereas cratered surfaces can be easily molded in large scale. Recently, emerging studies start to focus on reversible adhesives enabled by array of micro-craters. For example, in 2016, Choi et al. fabricated 1-μm-diameter craters on the surface of polydimethylsiloxane (PDMS) (Figure 6.2d) and measured the adhesive shear strength of 1.6 kPa, which exceeds the adhesive strength of the same PDMS with both flat surfaces and surface pillars [9]. Closely packed sub-micron-sized surface dimples on UV resin [82] were reported with adhesive shear strength of 750 kPa with a preload of 3 N, which is very competitive among Gecko-inspired dry adhesives [103]. Octopus suckers equipped with a layer of thermoresponsive hydrogel show switchable adhesion and thus, can be used for transfer printing of semiconducting nanomembranes [83]. Octopus-inspired micro-craters with built-in protuberance structure demonstrated load-dependent adhesion both in dry and wet conditions [25], distinct from that of gecko-like adhesives. In addition, PDMS nanosucker arrays are flexible and generate strong adhesion even when applied on irregular surfaces [86].

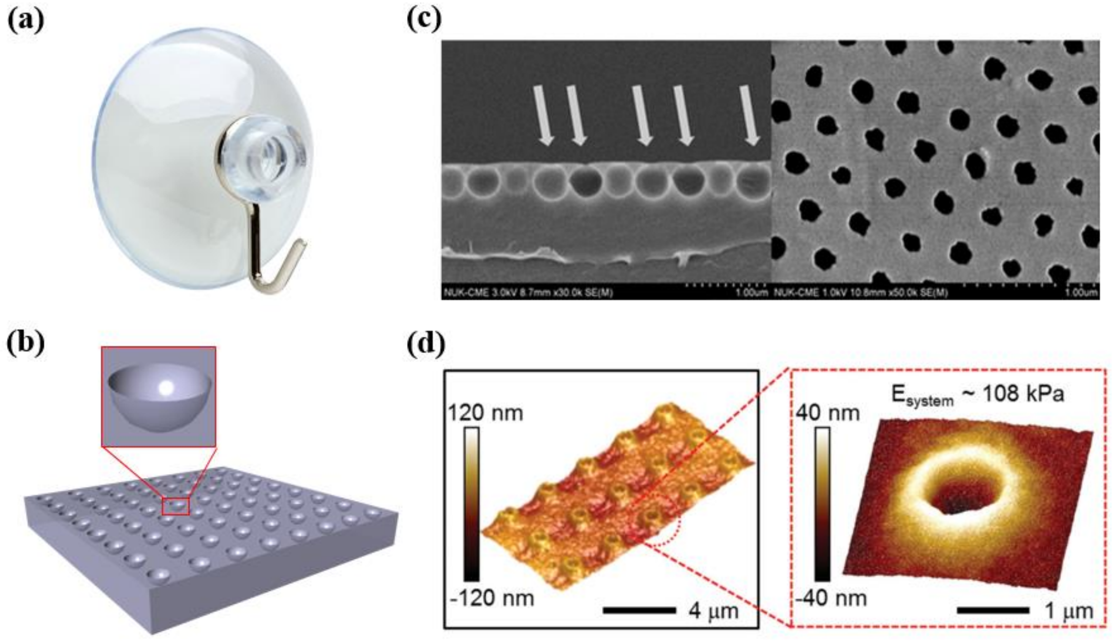

Figure 6.2 (a) A thin-walled suction cup fixture. (b) A 3D schematic of a cratered surface. (c) SEM images of closely packed sub-micron-sized surface dimples on UV resin (adopted with permission from Ref. [82], Copyright (2014) American Chemical Society). (d) AFM images of 1-µm-diameter craters on the surface of polydimethylsiloxane (PDMS) (adopted with permission from Ref [9], Copyright (2015) Wiley-VCH Verlag GmbH & Co. KGaA).

6.2 MOTIVATIONS

Unlike the abundant theoretical understandings for microfibrils [91, 104-106], cratered surfaces are emerging physical adhesives that little analysis is available at this moment. Although thin-walled suction cups have been modeled before [107, 108], surface craters [9, 25, 82, 83, 109] are surrounded by thick walls and therefore demand different analysis. Spolenak et al investigated various suction effect in pillars with concaved tip [91], but the pressure drop in the suction cup was considered to be constant. In Baik et al (2017), the authors presented a closed-form solution for the adhesion strengths of cratered surfaces. However, the analysis is based on the prior work of Afferrante et al [110] and Tramacere et al [111], which is applicable to suction cups rather than craters.

Fundamental understanding of the mechanical behavior of cratered surfaces is critical to the design of cratered surfaces, including optimal selection of material properties, crater shape, and preload. In Chapters 7 and 8, we established a theoretical framework to analyze isolated craters in both ambient condition and underwater condition, obtained nonlinear solutions to preload-dependent suction forces, and validated our solutions by experiments. We regard this study as an essential step toward developing a comprehensive framework for quantitative characterization of cratered surface.

In Chapters 7 and 8, in order to achieve suction effect, craters are incorporated with vent holes to help craters vent fluid inside the crater to ambient environment, which is not applicable in many situations. Real suction cups of octopus vulgaris contains two chambers that are connected through an orifice. The adhesion mechanism of octopus vulgaris suckers involve fluid exchanges between the two chambers, as explained in [112]. Baik and his colleague created passive double-chamber craters by adding protuberance to cylindrical-shaped-craters, and observed significantly improved adhesion strength. In Chapter 9, we looked into double-chamber craters, and implemented the numerical approach developed in Chapters 7 and 8 to study the fluid exchange and suction force of double-chamber craters. This implementation can also be extended to study craters with multiple chambers.

Chapter 7 Isolated Craters in Ambient Environment[3]

In this chapter, we analyze isolated craters in ambient environment and identify those leading to maximum adhesion. We first focus on hemi-spherical craters and establish a framework involving experimental, computational, and analytical characterizations of isolated macroscopic craters. Then, we consider spherical-cap-shaped (SCS) craters, establish the suction-preload dependence, and identify optimal geometric and material properties, as well as the minimum preload necessary to attain the maximum suction force. In the course of our studies, we find that materials suitable for many applications are too soft for optimal SCS craters. To this end, we consider SCS craters reinforced with thin stiff layers, and we discover reinforced craters that perform beyond our expectations. In the process, size effects associated with surface phenomena are neglected.

---

[3] Qiao S, Wang L, Jeong H, Rodin GJ, Lu N. Suction effects in cratered surfaces. *Journal of The Royal Society Interface*. 2017 Oct 1;14(135):20170377. (Conducted the numerical simulations, experiments and wrote the analysis section in the paper)

7.1 PROBLEM DESCRIPTION

Consider a specimen containing a hemi-spherical crater with radius a (Figure 7.1). The specimen rests on a flat rigid substrate. We suppose that the specimen is made of rubber, that is, it is capable of sustaining large elastic strains. The air inside the crater is the same as in the ambient environment, and it is characterized by the atmospheric pressure p_a, volume V_0, and molecules N_0 (Figure 7.1a). The suction effect is realized in two stages:

1. The specimen is compressed, so that the air is squeezed out of the crater; at the end of this stage, the remaining air in the crater is characterized by the triplet (p_1, V_1, N_1) (Figure 7.1b).
2. The specimen is unloaded, so that the crater springs back. This action results in a pressure drop associated with the suction effect. At the end of this stage, the air in the crater is characterized by the triplet (p_2, V_2, N_2) (Figure 7.1c).

Accordingly, the pressure drop is

$$-\Delta p = p_1 - p_2 \tag{7.1}$$

and the suction force is

$$F = -\Delta p A_2 \tag{7.2}$$

where A_2 is the projected area of the crater at the end of Stage 2.

A complete analysis of the two-stage process requires one to model the airflow dynamics. In this paper, we avoid this task by adopting the following assumptions:

1. The air flows freely out of the crater upon loading, so that $p_1 = p_a$.
2. No air exchange takes place upon unloading, so that $N_1 = N_2$.
3. The entire process is isothermal and the air is an ideal gas, so that $p_1 V_1 = p_2 V_2$.

As a result, the expression for the suction force becomes

$$F = \left(1 - \frac{V_1}{V_2}\right) p_a A_2 \tag{7.3}$$

With the adopted assumptions, the dynamics of airflow is regarded as a sequence of static equilibrium states. Consequently, it becomes sufficient to analyze the two-stage process in the context of solid mechanics, as it is explained in Section 2.3.

In the remainder of this chapter, we describe an experimental setup designed to conform with the adopted assumptions. Further, we show that the experimental results can be accurately predicted using nonlinear elasticity theory alone, which means neglecting the airflow dynamics appears to be a good assumption.

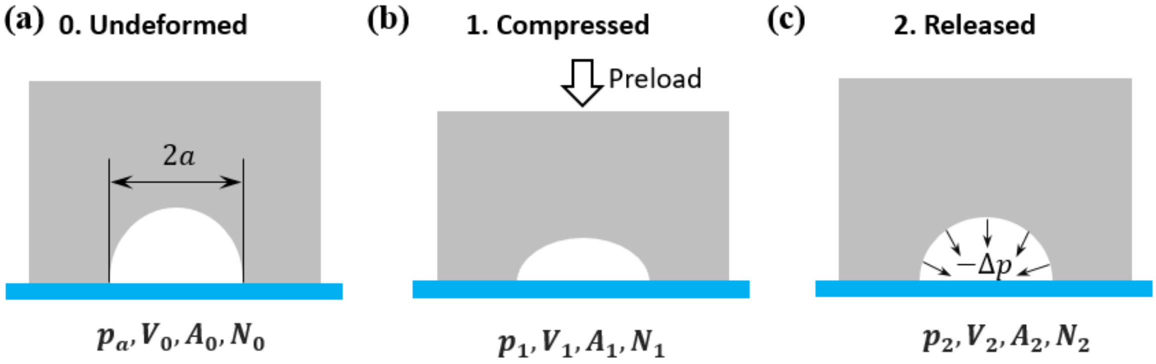

Figure 7.1 A loading-unloading cycle that produces the suction effect: (a) A specimen with an isolated hemi-spherical crater of radius a resting on a flat plate (blue); (b) The specimen is preloaded in compression and the air is squeezed out of the crater; (c) The preload is released, and the springback induces vacuum in the crater. The symbols p, V and N denote the pressure, volume, and number of molecules of air inside the crater at each state

7.2 HEMI-SPHERICAL CRATERS

In this section, we use experimental, computational, and analytical approaches to study isolated hemi-spherical macroscopic craters filled with air. The computational framework established in this section will be applicable to more general classes of isolated macroscopic craters.

7.2.1 Experimental Measurements

The experimental setup was designed so that it realizes the two-stage process under conditions that well represent the adopted assumptions. We choose polydimethylsiloxane (PDMS, Sylgard 184 Dow Corning) to make our specimens as it is a quintessential rubber with negligible rate-dependence in the time-temperature range in our experiments [113]. Cylindrical specimens with diameter 25.40 mm and height 35.13 mm was molded from PDMS with the base-to-curing-agent mass ratio equal to 30:1, and then cured at 70℃ for 12 hours. A hemi-spherical crater of diameter 12.70 mm was placed at the center of a circular face.

Pure rectangular prisms without crater were also made for identifying material properties. The dimensions of the prisms were $25\times25\times40$ mm^3. To this end, we conducted a uniaxial compression test using a Dynamic Mechanical Analyzer (DMA) (RSA-G2, TA Instruments). The top and bottom surfaces of the specimen were lubricated by performance oil (Fellowes Powershred Performance Shredder Oil) such that the specimen was under uniaxial stress. The loading velocity was set at 3 mm/min, which corresponds to a nominal strain rate of 1.25×10^{-3} s^{-1}, so that the deformation was dominated by rubber elasticity. The axial load-displacement data were converted into the nominal stress σ versus the principal stretch λ data and fitted by the incompressible Neo-Hookean model

$$\sigma = \mu\left(\lambda - \frac{1}{\lambda^2}\right) \tag{7.4}$$

where the shear modulus μ is the small strain shear modulus as well as a fitting parameter. As shown in Figure 7.2, this model fits the experimental data very well for $\mu = 47.3$ kPa.

Direct measurements of the suction force upon unloading are difficult. Therefore we performed the loading-unloading experiments on the specimens and measured the pull-off force rather than suction force. These data can be used for calculating the suction force. We conducted a series of uniaxial compression tests using the DMA and a Mechanical Testing System (MTS Servohydraulic load frame with Instron 8500R controller). The loading cell in our DMA has good resolution (0.00001 N) but limited loading range (up to 35 N), whereas the loading cell in MTS has sufficient loading range (up to 250 N) but low resolution. Thus, experiments with loading force greater than 35 N were performed with the MTS, while the rest were done by using DMA.

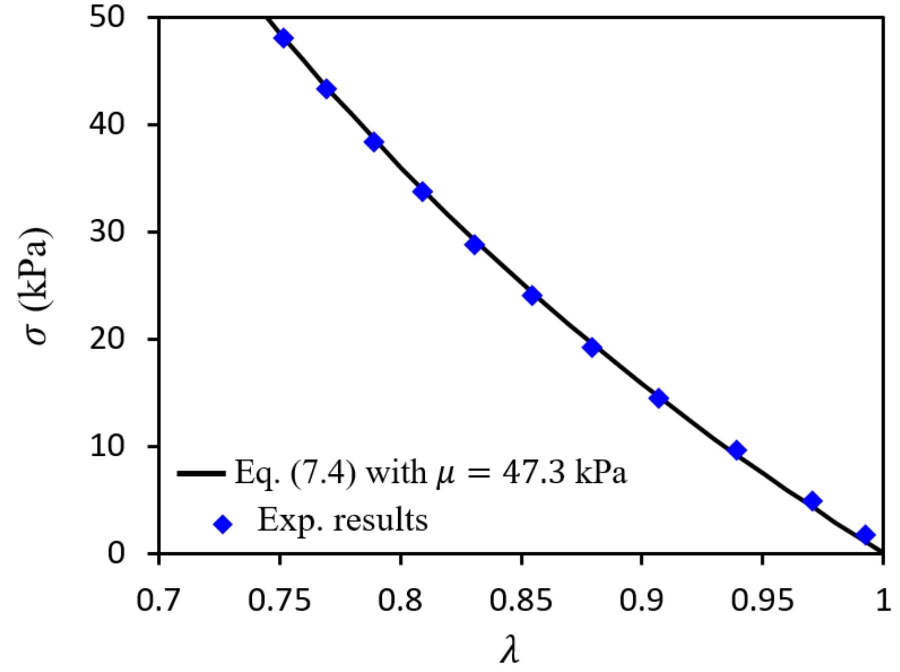

Figure 7.2 Nominal stress σ versus the principal stretch λ. The data were obtained using pure rectangular specimens subjected to uniaxial compression, and fitted based on the incompressible Neo-Hookean model (Eq. (7.4)) for μ=47.3 kPa.

In both testing systems, the top and bottom surfaces of the specimen were still lubricated by performance oil such that the specimen was free of friction and loaded under uniaxial stress.

To realize experimental conditions that well represent the adopted assumptions, we built a special platform as illustrated by a schematic in Figure 7.3a and a photograph in Figure 7.3b. The cratered specimen was compressed against a stiff acrylic platform. At the platform center, we drilled a ventilation hole with diameter of 0.8 mm, which was used for releasing and trapping the air in the crater. During the first stage, consistent with the first assumption, the vent hole was kept open. During the second stage, consistent with the second assumption, the hole was sealed. Both stages were realized under a 3 mm/min loading velocity. To measure the pull-off force, the second stage involved not only unloading but also retraction. That is, during the second stage, the specimen was stretched beyond the unloading point, until the cratered surface was pulled off the platform. This pull-off force is denoted as F'. To extract the suction force, we performed the same loading-unloading experiments with the vent hole open throughout the test and the collected pull-off force is denoted as F''. Representative load-displacement curves for both cases are plotted in Figures 7.3c and 7.3d. There we identify the loading, unloading, and retraction stages, as well as the pull-off force. Note that the two sets of data are qualitatively similar. Nevertheless quantitative differences are significant enough to identify the suction effect.

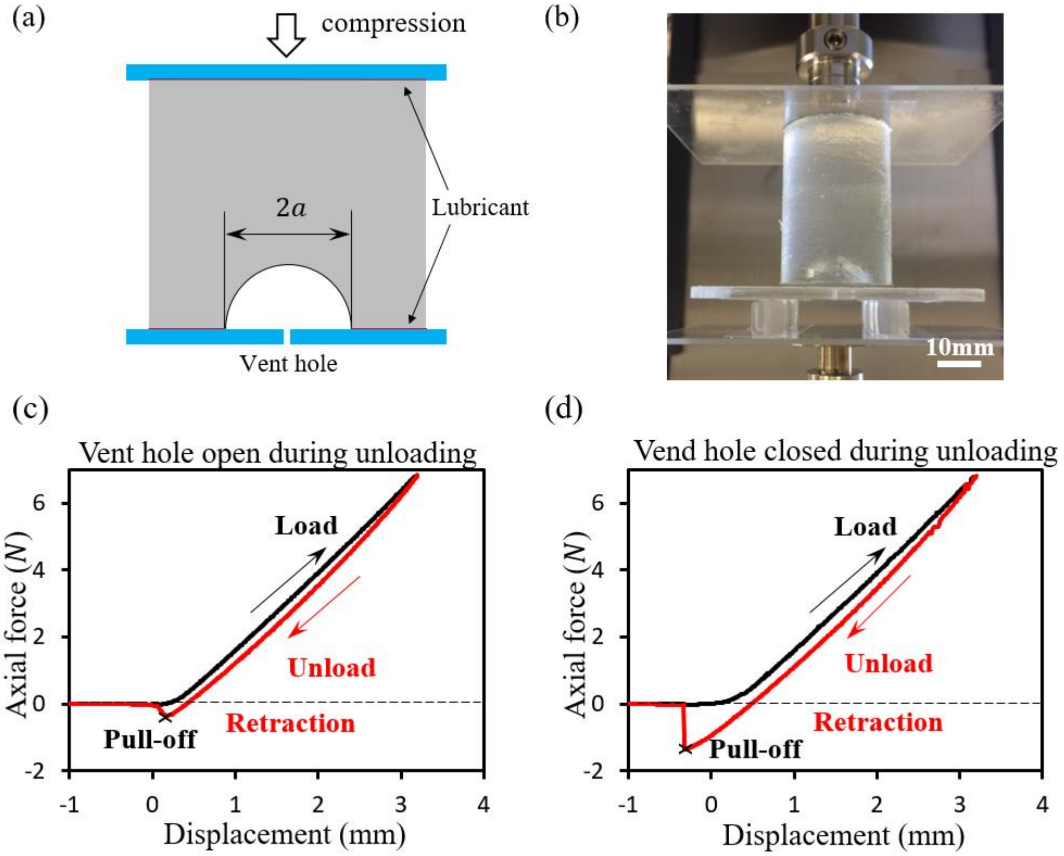

Figure 7.3 A schematic drawing (a) and a photograph (b) of the experimental platform. The small ventilation hole drilled in the bottom plate is open during loading and closed during unloading. Load-displacement curves with vent hole open (c) and closed (d) during unloading. Peak compressive strain was 10%. Loading, unloading, retraction stages, and the pull-off points are identified.

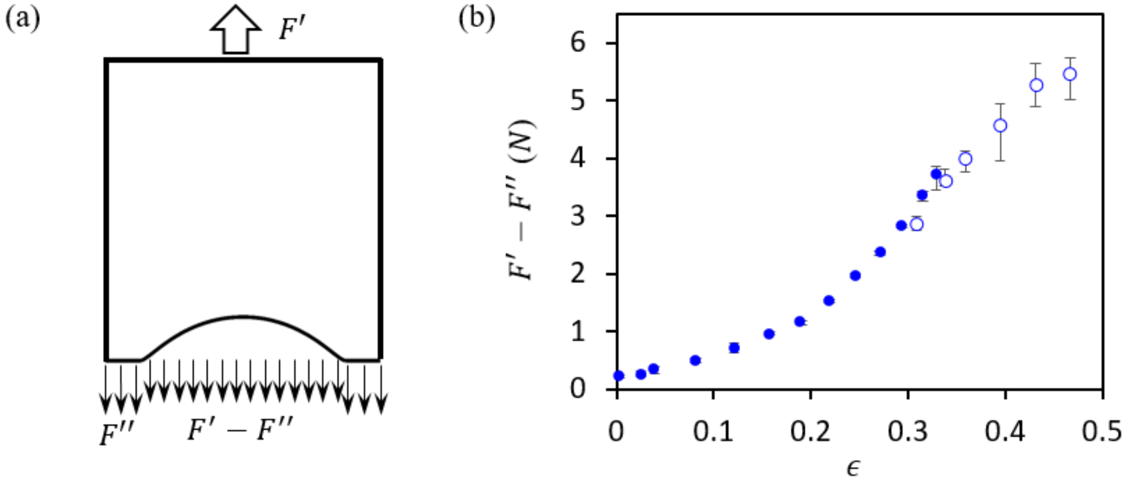

Figure 7.4 (a) A schematic of the free body diagram of a specimen at pull-off. (f) Experimentally measured suction forces ($F'-F''$) of air-filled craters. Data obtained by DMA are represented by solid dots and MTS by hollow circles.

The experimentally collected pull-off force F' is a resultant force of the adhesion strength over the specimen/platform interface and the suction force over the crater, whereas F'' only consists of the interface adhesion. Thus, the difference in value

$$F = F' - F'' \tag{7.5}$$

produces the suction force inside the crater at pull-off as illustrated by the free body diagram in Figure 7.4a. In Figure 7.4b, the suction force $F' - F''$ is plotted against the preload ϵ, which is the peak macroscopic axial strain defined as

$$\epsilon = -\Delta L/L \tag{7.6}$$

where L is the specimen axial length. Solid dots denote results measured are by DMA while hollow dots are measured by MTS. In general, craters can produce stronger suction force when larger compression is applied. Note that experimental results from DMA were limited to $0 \leq \epsilon \leq 0.32$, which is associated with the allowable load of the DMA used in the experiments. At $\epsilon \approx 0.32$, we measured pull-off forces by both DMA and MTS, and the corresponding results are in good agreement which justifies the consistence between the experiments performed via DMA and MTS.

7.2.2 Finite Element Analysis

Following experimental data for the pure prismatic specimens, we assumed that the constitutive behavior of the cratered specimens is described by the incompressible Neo-Hookean constitutive model with $\mu =$ 47.3 kPa. To simplify the analysis, we applied axisymmetry, and the specimen/substrate interface was assumed to be frictionless (Figure 7.5a). Also we neglected any surface tension effects simply because

$$\frac{\gamma}{a\mu} \approx \frac{2 \times 10^{-2}\, N/m}{(10^{-2}\, m) \times (4 \times 10^{4}\, N/m^{2})} = 5 \times 10^{-5} \ll 1 \qquad (7.7)$$

where γ is the surface tension of PDMS [114].

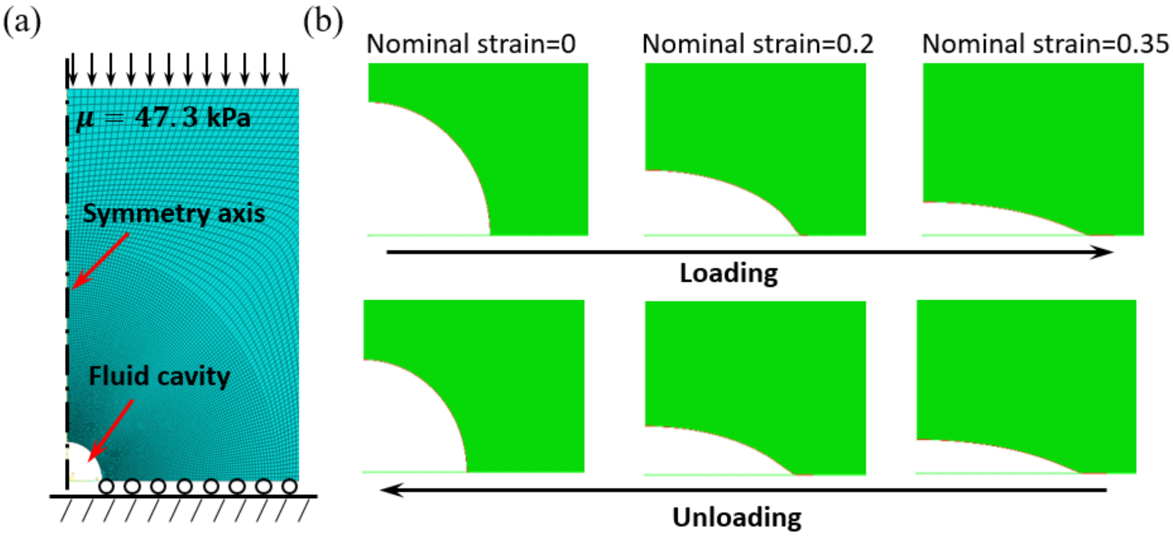

Figure 7.5 (a) A finite element mesh for an axisymmetric crater model. (b) A deformation sequence of a specimen in a loading-unloading test: top row for loading stage and bottom row for unloading stage

Following the third assumption, the gas inside the crater was assumed to be ideal, and its pressure during the second stage was controlled by the crater volume. Since the solid is assumed to be incompressible, one can define the reference state for the solid as the one in which the specimen is uniformly compressed with the ambient pressure p_a.

We used finite element simulations to compute the relationship between the suction force $F = -\Delta p A_2$ and the preload ϵ. All simulations were conducted using Abaqus. The finite element mesh formed by CAX4H elements is shown in Figure 7.5a; this mesh was selected using basic convergence tests. We used the option *FLUID CAVITY which is ideal for modeling both stages of the gas-solid interactions.

Figure 7.5b shows a sequence of deformed configurations of a specimen with hemi-spherical crater in a loading-unloading test. The first panels in top and bottom rows are the initial (before loading) and final (end of unloading) configurations, respectively. The third panel in each row corresponds to the end of loading with $\epsilon = 0.35$, and the rest are intermediate states. At the end of the unloading, the finite element results indicate that the crater maintains the spherical symmetry.

7.2.3 Linear Elasticity Analysis

In this section, we present linear elasticity analysis of the problem based on Eshelby's formalism [115]. We treat the crater as an isolated hemi-spherical crater in a semi-infinite specimen, and take advantage of the assumption that the contact between the specimen and the substrate is frictionless. This allows us to replace the problem for semi-infinite specimen containing a hemi-spherical crater with an infinite specimen containing a spherical cavity. This problem is straightforward to analyze using Eshelby's formulism

According to Eq. (7.3), we need to calculate V_1, V_2, and A_2. Note that according to classical linear elasticity, the quantities $\Delta V_1 = V_1 - V_0$, $\Delta V_2 = V_2 - V_0$, and $\Delta A_2 =$

$A_2 - A_0$ are infinitesimal. This allows us to replace A_2 with A_0. However, computing ΔV_1 and ΔV_2 is essential for meaningful calculation of the suction force.

To compute ΔV_1, we subject the infinite specimen to remote uniaxial compressive strain ϵ. For this case, Eshelby's formulism yields

$$\Delta V_1 = -\frac{3}{2}(1-\nu)\epsilon V_0 \tag{7.8}$$

where ν is the Poisson's ratio of the specimen material, and for incompressible material, we have $\nu = 1/2$.

To compute ΔV_2, we subject the cavity to the surface traction

$$\boldsymbol{t} = (p_1 - p_2)\boldsymbol{n} = (p_a - p_2)\boldsymbol{n} = -\Delta p\,\boldsymbol{n} \tag{7.9}$$

where $\boldsymbol{n}$ is the outward normal. As far as ΔV_2 is concerned, this problem is equivalent to the superposition of two problems. In the first problem, the specimen is uniformly loaded by $-\Delta p$ on both cavity and remote surfaces. In the second problem, the cavity surface is traction-free and the remote surface is subjected to Δp. As a result, we obtain

$$\Delta V_2 = \frac{3}{4}\frac{\Delta p}{\mu}V_0 \tag{7.10}$$

where

$$\Delta p = -\left(1 - \frac{V_1}{V_2}\right)p_a \tag{7.11}$$

Combing Eqns. (7.8), (7.10), and (7.11), one can the resulting suction force

$$F = \frac{1}{2}\left[\left(1 + \frac{4\mu}{3p_a}\right) - \sqrt{\left(1 + \frac{4\mu}{3p_a}\right)^2 - 8(1-\nu)\frac{\mu}{p_a}\epsilon}\,\right]p_a A_0 \tag{7.12}$$

7.2.4 Results

In this section, we first look into finite element simulations of hemi-spherical craters, and then compare experimental, computational, and analytical results.

In Figure 7.6, we still consider hemi-spherical craters with μ =47.3 kPa. Different system parameters upon unloading as functions of ϵ are plotted: (a) normalized volume change $(V_0 - V_2)/V_0$, (b) normalized pressure drop $-\Delta p/p_a$, (c) normalized projected area A_2/A_0, and (d) normalized suction force

$$\tilde{F} = -\Delta p A_2/(p_a A_0) \tag{7.13}$$

Figures 7.6a and 7.6b show that when filled with ideal gas, the hemi-spherical crater experiences increase in volume change and pressure drop with growing ϵ. In Figure 7.6b, the lateral dashed line represents the critical pressure drop Δp_c under which the spherical symmetry of the recovered hemi-spherical crater breaks down upon unloading. This critical load $-\Delta p_c$ is found to be $0.83p_a$ by looking into the surface instability of a spherical void in an infinitely large block made of incompressible Neo-Hookean material [116, 117]. And the corresponding critical preload ϵ_c is 0.43 according to Figure 7.6b (dashed blue line). As observed in finite element simulations, once the spherical symmetry breaks down upon unloading, the recovered crater shows shallower but wider profile, which results in increased projected area, i.e. larger A_2. This agrees with the increasing trend of A_2/A_0 for $\epsilon > \epsilon_c$, as plotted in Figure 7.6c.

Figure 7.6d plots the normalized suction $\tilde{F}$, which is mutually produced by the enhanced pressure drop and the compromised projected area. Full closure of the crater is reached at $\epsilon = 0.47$ as indicated by vertical dash black lines in Figures 7.6a~7.6d, respectively. At full closure, craters can reach maximum $\tilde{F}$ which is less than 1 because of the impaired A_2 upon unloading. It is clear that the suction forces no longer changes for $\epsilon > 0.47$.

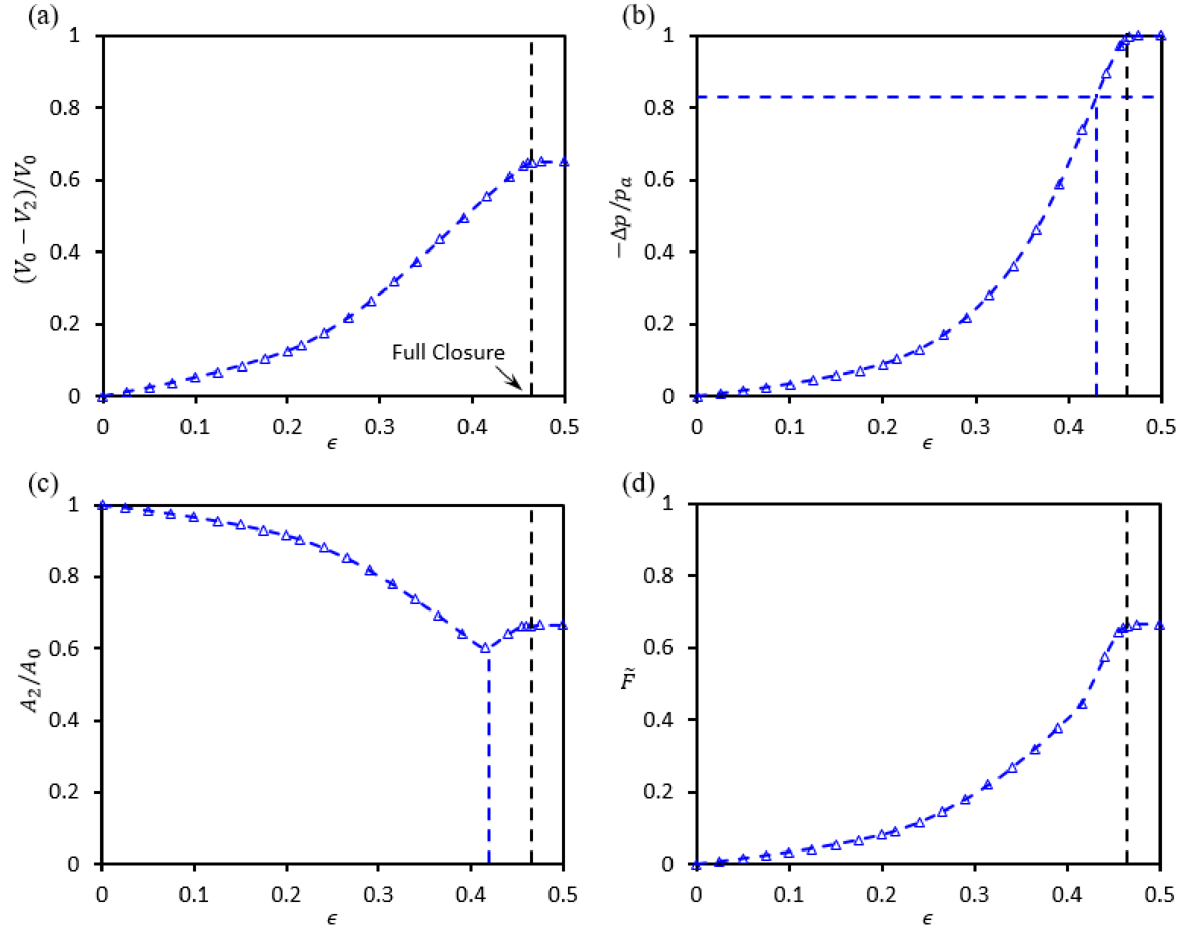

Figure 7.6 End results of the loading-unloading test are computed and plotted as functions of the preload ϵ: (a) normalized volume change $(V_0 - V_2)/V_0$, (b) normalized pressure drop $-\Delta p/p_a$, (c) normalized projected area A_2/A_0, and (d) normalized suction force $\tilde{F} = -\Delta p A_2/(p_a A_0)$

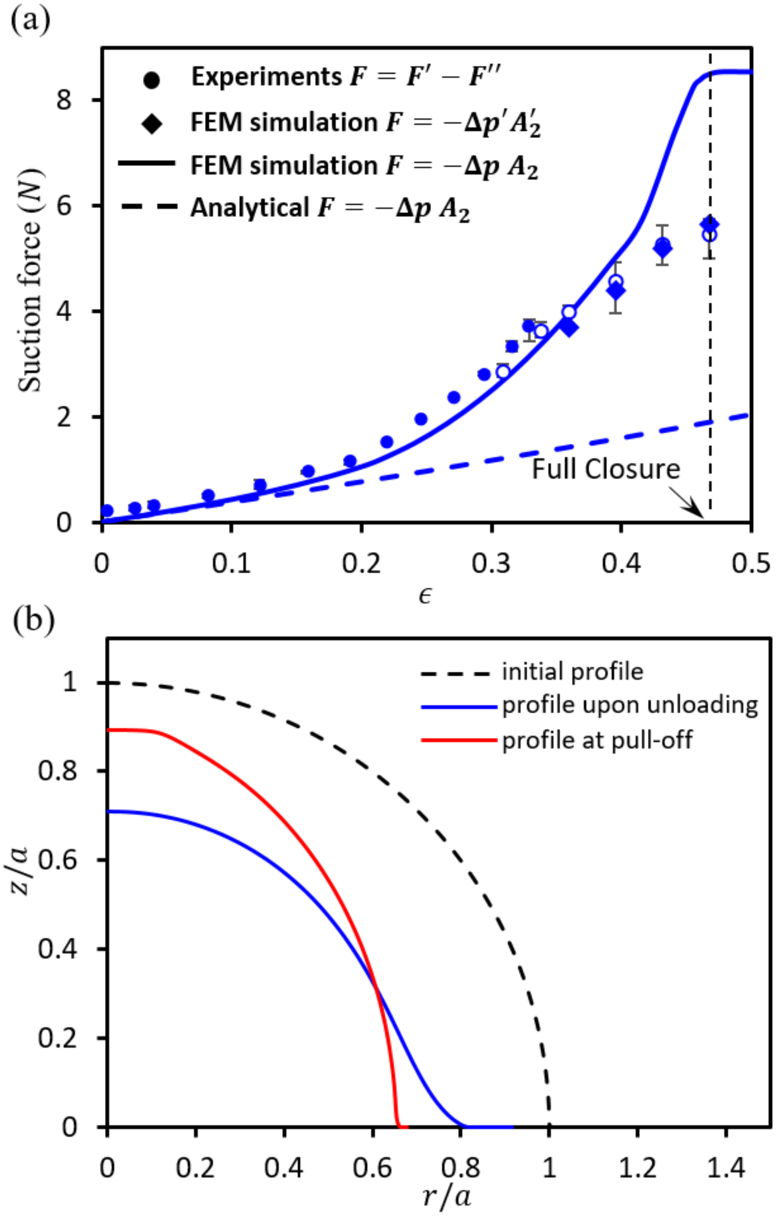

Figure 7.7 (a) Comparisons of suction forces obtained by experimental measurements (circular markers), analytical modeling (dashed curves) and finite element simulation (solid curves and diamond markers). (b) Finite element simulation results of crater profiles upon unloading (blue curve) and at pull-off (red curve) with preload $\epsilon=\epsilon_m$. Dashed curve represents the initial profile of the hemi-spherical crater

Comparisons of experimental (circular markers), simulation (solid curve), and analytical (dashed curve) results are shown in Figure 7.7a, where the suction force is plotted versus the preload ϵ. In the range of $0 \leq \epsilon \leq 0.36$, experimental and simulation results are in good agreement, which validates the use of the modeling assumptions, as well as extending the simulations for characterizing more general situations under loading range $0 \leq \epsilon \leq 0.36$. The calculated suction force $-\Delta p A_2$ using linear elasticity analysis is plotted as the dashed blue curve in Figure 7.7a. It is clear that the linear analysis is only valid for small strains, and deviates significantly from the experimental and simulation results for $\epsilon > 0.1$, and therefore its usefulness is rather limited.

Under large preload, especially when craters reach full closure upon loading, finite element simulation shows considerable discrepancy from experimental results. One source of the discrepancy comes from the different definitions of suction force used in experiments and simulations. In experiments, $F' - F''$ represents the suction force inside the crater at pull-off, while in simulations, $-\Delta p A_2$ is the suction force at the end of unloading and before retraction. At small preload, it is fair to argue that the crater has similar configuration at pull-off point and upon unloading, such that

$$F' - F'' \approx -\Delta p A_2 \tag{7.14}$$

is expected. This is true under loading range $0 \leq \epsilon \leq 0.36$ based on the observation from Figure 7.7a. However, the approximation in Eq. (7.14) will no longer hold once significant difference exists between the pull-off status and the fully unloading status. In finite element simulations, experimentally measured retraction strain at pull-off, ϵ_t, can be applied after unloading. Resulted suction forces, $F = -\Delta p' A_2'$, are plotted as blue diamonds in Figure 7.7a, where $\Delta p'$ and A_2' represent the finite element results of pressure drop inside the crater and the projected area of the crater at “pull-off”, respectively. It is found that $\Delta p'$ does not differ from Δp significantly (relative error < 1%), but A_2' is considerably smaller than A_2, as shown in Figure 7.7b. In Figure 7.7a, the good agreement between $F = -\Delta p' A_2'$ and $F' - F''$ indicates that, for air-filled craters, the discrepancy between finite element simulation and experimental results can be fully explained by the difference in $-\Delta p A_2$ and $F' - F''$.

Thus, to accurately predict the suction force at pull-off, one needs the traction-separation behavior of the specimen/platform interface, which is out of our focus. So, we would focus on the study of the suction force $-\Delta p A_2$ upon unloading for the rest of this chapter.

7.3 SPHERICAL-CAP-SHAPED CRATERS

In this section, we extend the simulation approach developed for hemi-spherical craters to spherical-cap-shaped (SCS) craters. Our focus is on maximizing the suction force $-\Delta p A_2$ by optimizing the crater shape and specimen mechanical properties. Since our analysis is limited to large specimens, the only dimensionless geometric parameter involved is

$$\alpha = \frac{b}{a} \tag{7. 15}$$

where a is crater base radius and b is the crater height (Figure 7.8). The dimensionless stiffness parameter is defined as

$$\beta = \frac{\mu}{p_a} \tag{7. 16}$$

Note that the Greek symbols α and β were also used in Chapter 3 for different purpose, and readers should not be confused with the reuse of symbols α and β in succeeding text.

In the previous section, these parameters were fixed at $\alpha = 1$ and $\beta = 0.47$. Further, in the previous section, the preload ϵ was varied. In contrast, in this section, this parameter is set to be ϵ_m, which is the preload so that the crater attains a full closure and realizes complete vacuum. With this provision, we have $V_1 = 0$, and the suction force is computed from Eq. (7.3) as

$$F = \left(1 - \frac{V_1}{V_2}\right) p_a A_2 = p_a A_2 \tag{7. 17}$$

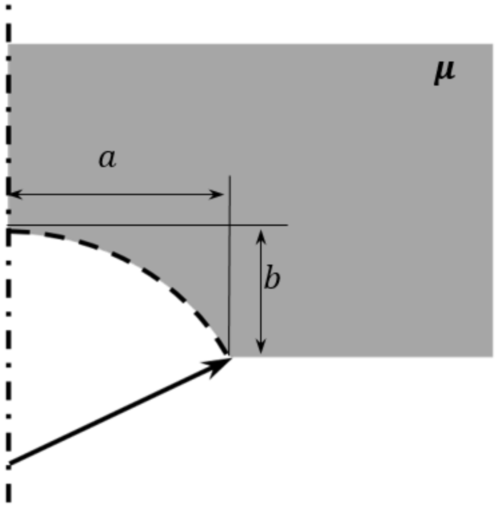

Figure 7.8 A schematic of the spherical-cap-shaped (SCS) crater

The normalized suction force $\tilde{F}$ as a function of α and β can be produced using finite element simulations, and is presented as a contour plot in Figure 7.9a. This plot clearly demonstrates that large $\tilde{F}$'s are realized by specimens with large α and β. But the dependence of $\tilde{F}$ on α and β is not monotonic. Further, for sufficiently stiff specimens, the dependence on α is relatively weak. We identify "good" specimens as those for which $\tilde{F} > 0.8$; the rest of the specimens are regarded as "bad". This (arbitrary) classification is represented by the black curve in Figure 7.9a. In Figure 7.9b, we present ϵ_m as a function of α; apparently ϵ_m is independent of β. As expected, deep craters require large ϵ_m.

To gain further insight into simulation results in Figure 7.9a, we present the deformed shape of twelve specimens upon full unloading corresponding to $\alpha =$ 0.25, 0.5, 0.75, 1 and $\beta =$ 0.5, 1, 10 (Figure 7.10). The dashed lines show the initial craters. According to Figure 7.10, it is clear that stiff specimens with deep craters are capable of recovering in a way that $A_2 \approx A_0$, and therefore, for such specimens $\tilde{F} \approx 1$. In contrast, soft specimens with shallow craters result in $A_2 \ll A_0$ and therefore $\tilde{F}$ is very small.

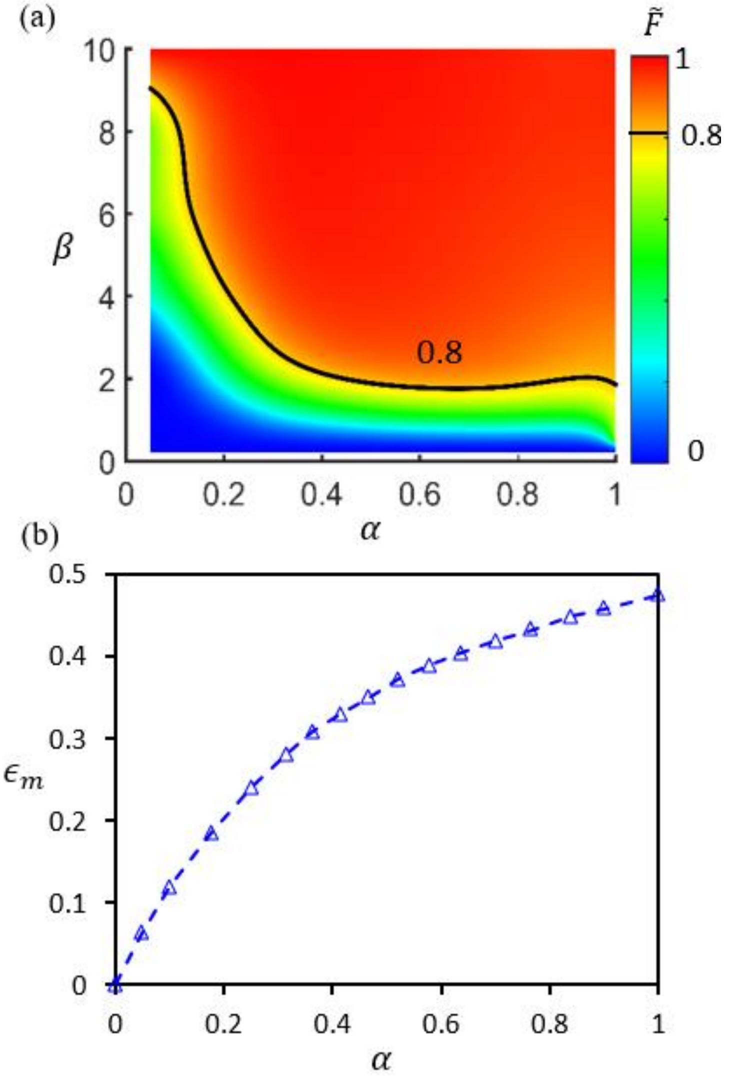

Figure 7.9 (a) A contour plot for the normalized achievable suction force $\tilde{F}$ as a function of α and β. (b) Minimum preload strain for closure ϵ_m as a function of α

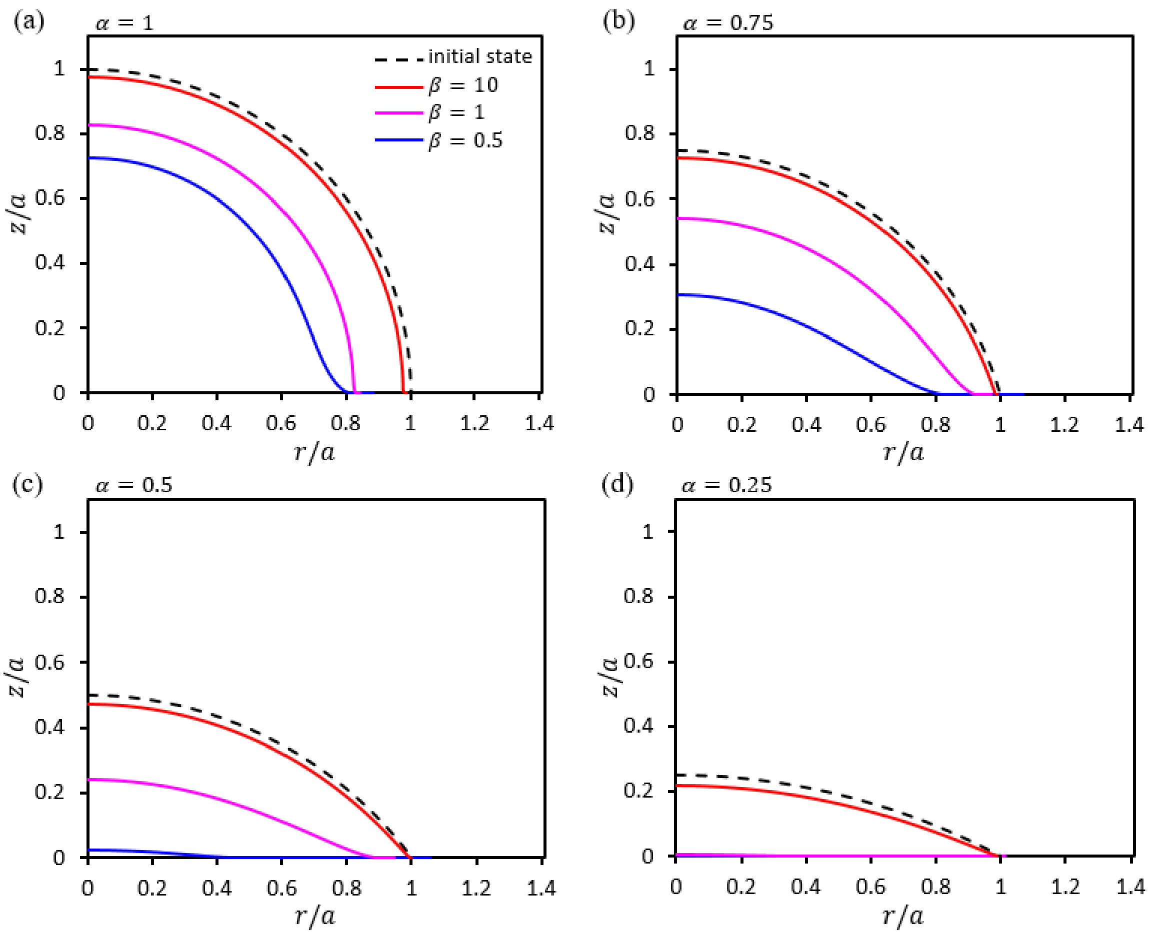

Figure 7.10 Deformed (solid lines) and undeformed (dashed lines) shapes of craters. The deformed shapes correspond to complete unloading

7.4 REINFORCEMENT LAYER

While stiff specimens with deep craters result in large suction forces, many biomedical applications involve soft polymers for which $\beta \approx 1$. According to Figure 7.9a, such specimens are classified as bad ones. To address this issue we consider soft specimens with craters reinforced by thin stiff layers (Figure 7.11a), with the expectation that such layers would result in the recovered base area $A_2 \approx A_0$. Such layers are straightforward to manufacture. For example, PDMS with the base-to-curing-agent mass ratio equal to 10:1 has shear modulus around 1 MPa, and thus, can be used to reinforce a cratered specimen made of Ecoflex® 0300 (Smooth-On, Inc.) whose shear modulus is about 27 kPa [118]. In what follows, the stiff layers added to the surface of the craters are called reinforcement layers, which should not be confused with the bulk reinforcement.

We considered reinforcement layers made of incompressible Neo-Hookean materials, so that the layers were characterized by the dimensionless parameters

$$\alpha' = \frac{t}{a} \text{ and } \beta' = \frac{\mu_l}{\mu} \tag{7. 18}$$

where t and μ_l are the layer thickness and shear modulus, respectively. To reduce the size of the parametric space, we limited our studies to $\beta = 1$. As a result, the optimal search involved three parameters only: α, α' and β'; as in the simulations for unreinforced craters, the preload was equal to ϵ_m.

First, we set $\alpha = 1$ and examined the $\alpha' - \beta'$ parametric space. We determined that the best craters were characterized by $0.015 < \alpha' < 0.045$ and $10 < \beta' < 50$. In this parametric domain, the normalized suction force was $0.99 < \tilde{F} < 1.09$. It is remarkable that one can achieve $\tilde{F} > 1$ Upon further inspection of simulation results, we determined that all cases resulting in $\tilde{F} > 1$ involved crater surface instabilities. In most cases, $\tilde{F} > 1$ was associated with instabilities upon unloading only. In some cases, we observed instabilities both upon loading and unloading. To visualize relationships between instabilities and the normalized suction force, we present a three-color map in the $\alpha' - \beta'$ parametric space (Figure 7.11b). The green color corresponds to craters that exhibit instabilities upon both loading and unloading, the red color corresponds to craters that exhibit instabilities upon unloading only, and the blue color corresponds to stable craters. The yellow box is the boundary of the domain inside which $\tilde{F} > 1$. This map was constructed on the basis of a coarse grid in the $\alpha' - \beta'$ parametric space, and therefore the map boundaries are somewhat approximate.

Next, we set $\alpha' = 0.03$ and $\beta' = 30$ and examined the dependence of $\tilde{F}$ on α; note that the chosen α' and β' are the centers of the respective optimal parametric intervals identified in the previous set of simulations. Simulation results for $\tilde{F}$ versus α are shown in Figure 7.11c. The peak force of $\tilde{F} = 1.17$ is achieved for $\alpha = 0.85$. This value exceeds the force for the unreinforced specimen with $\alpha = 0.85$ by a factor of 1.17/0.80≈1.46. Note that the optimal unreinforced crater is characterized by $\alpha = 0.7$ rather than $\alpha = 0.85$; in this case $\hat{F} = 0.84$ and the amplification factor is 1.17/0.84≈1.39.

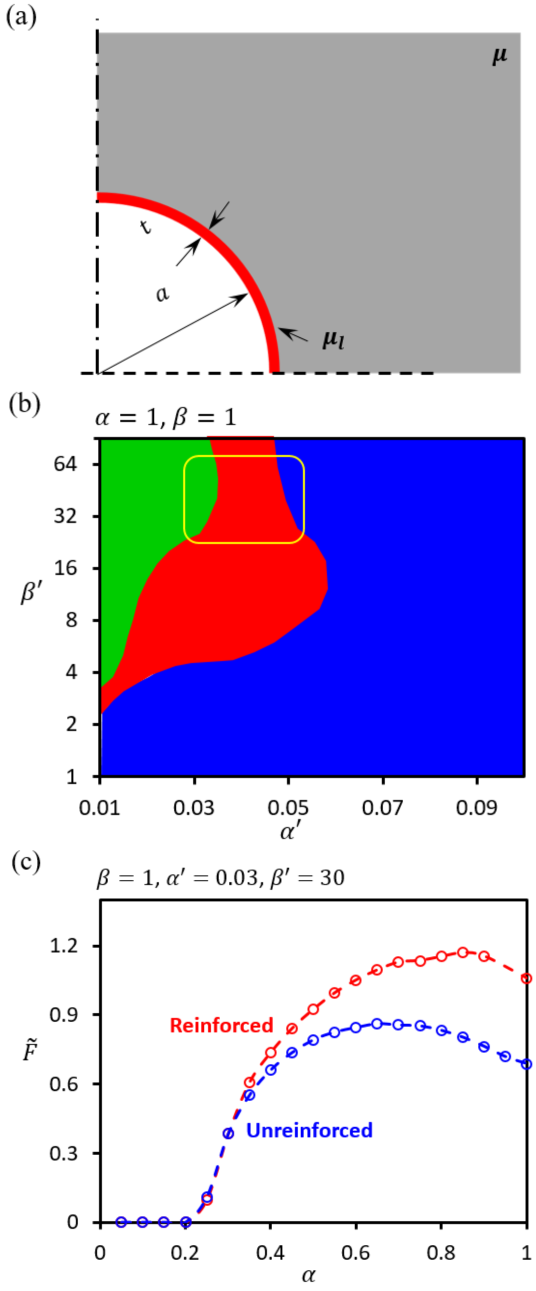

Figure 7.11 (a) A schematic of a hemi-spherical crater reinforced by a thin stiff layer (red). (b) A three-color map in the α'–β' parametric space for specimens with $\alpha = \beta = 1$. The green zone is for craters exhibiting instabilities upon both loading and unloading, the red zone is for craters exhibiting instabilities upon unloading only, and the blue zone is for stable craters. The interior of the yellow line is for craters with $\tilde{F} > 1$. (c) Comparison of the reinforced and unreinforced craters

7.5 DISCUSSION

In this section, we look into instabilities in reinforced craters, and discuss the gas permeation issue in our experiments. Before setting into these topics, the following point is worth noting. In this chapter, optimization studies involve preloads which completely close the crater. In practice, such preloads may be impossible to apply, and therefore the optimization procedure may be different. For example, if the preloading device can exert a maximum force insufficient for attaining ϵ_m, as it was the case in our experiments, then the optimization procedure must include this condition as a constraint. That is, the optimal parameters must be determined under the constraint that the preloading force cannot exceed a prescribed value dictated by the preloading device.

7.5.1 Instabilities Occurring in Reinforced Craters

While the main focus of this work is on identifying craters that maximize the suction force, it is important to appreciate that mechanical behavior of reinforced craters is rather complex. Due to the stiffness mismatch between the reinforcement layer and specimen matrix, instabilities may occur during both loading and unloading. Understanding of relationships between the suction force and the underlying deformation mechanisms for reinforced craters is difficult. At this stage, we perform finite element simulations using various reinforcement layers and summarize the deformation of reinforced craters into four types. Representative cases of reinforced craters for each type are presented in Figure 7.12. In all cases, the craters are characterized by $\alpha = \beta = 1$, that is, all craters are hemi-spherical with $\mu = p_a$.

The crater in Figure 7.12a can be described as weakly reinforced because the reinforcement layer is thin ($\alpha' = 0.015$) and not very stiff ($\beta' = 2$). This weak reinforcement is inadequate, as it results in $\tilde{F} = 0.70$ only. The six figures in the first row are instances of the loading-unloading cycle. The first and last figures in this sequence are the initial and final configurations, respectively. The third figure corresponds to full closure, and the rest are intermediate states. Note that in the final configuration, the projected area is significantly smaller than the initial one, which explains the low value of $\tilde{F}$ It is clear that the deformation of this crater does not involve surface instabilities.

In contrast to the first case, the crater in Figure 7.12b involves a strong reinforcement with $\alpha' = 0.055$ and $\beta' = 40$. This strong reinforcement results in $\tilde{F} = 0.94$, which is an improvement over the weakly-reinforced crater, but still suboptimal, as far as reinforced craters are concerned. The corresponding six figures (the second row) show that the loading-unloading cycle involves long-wavelength instabilities, which disappear upon unloading.

The third case involves a thin ($\alpha' = 0.015$) but very stiff ($\beta' = 80$) reinforcement layer (Figure 7.12c). This is an excellent reinforcement resulting in $\tilde{F} = 1.07$. The loading-unloading cycle is prone to short-wavelength instabilities which do not disappear upon complete unloading. Note that instabilities form upon loading, near the equator, and disappear at full closure. Instabilities reemerge at the equator upon unloading, and propagate toward the pole. This pattern of instabilities suggest that design of optimal reinforced craters could be challenging.

The fourth case with $\alpha' = 0.03$ and $\beta' = 80$ (Figure 7.12d) involves a moderate reinforcement which results in $\tilde{F} = 0.91$. We included this case to demonstrate that, in contrast to the third case, instabilities arising upon loading and unloading can be quite different. In particular, the loading stage involves long-wavelength instabilities, if at all, whereas the unloading stage is characterized by short-wavelength instabilities.

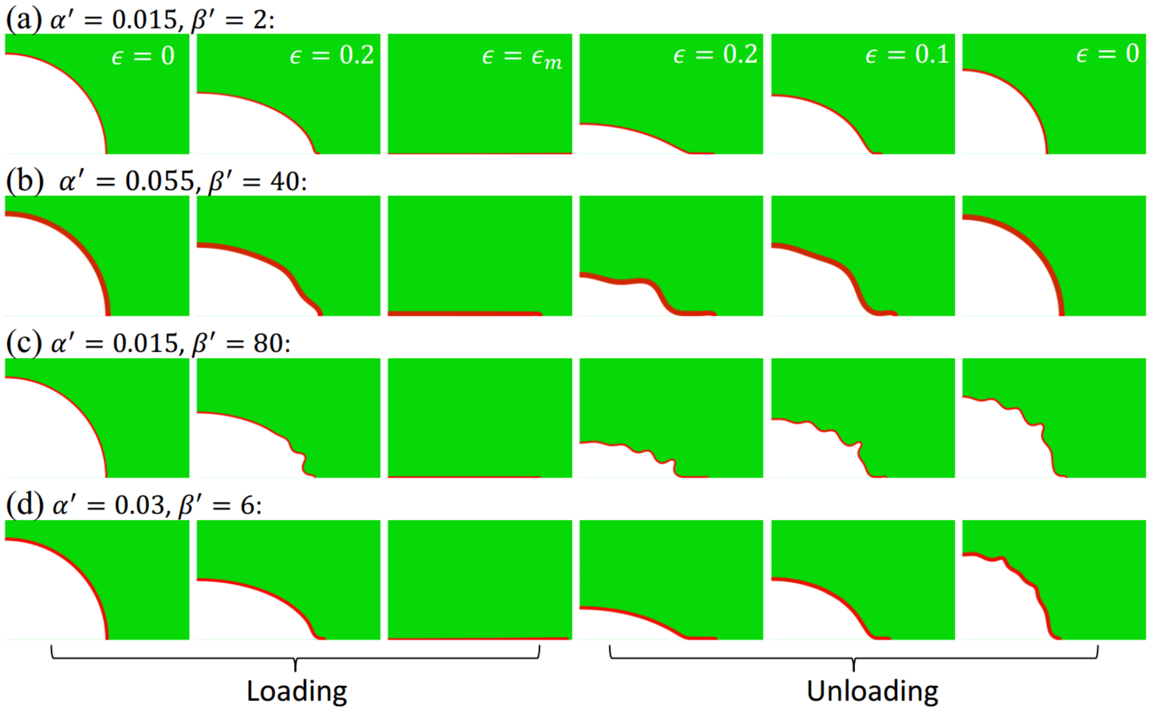

Figure 7.12 Four representative reinforced craters with ($\alpha = \beta = 1$): (a) no instability during either loading or unloading, (b) long-wavelength instabilities during both loading and unloading, (c) short-wavelength instabilities during both loading and unloading, and (d) short-wavelength instabilities during unloading only. For each case, the frames at $\epsilon =$ 0, 0.2 and ϵ_m represent the loading stage, and the frames at $\epsilon =$ 0.2, 0.1 and 0 represent the unloading stage

7.5.2 Effect of Gas Permeation

Gas permeation is important in structures made of PDMS, especially for ones in micro size whose area-to-volume ratios are high. For bulk PDMS specimens, the solution-diffusion model is usually applied [119], in which the Henry permeability, $P_{Henry} = DS$, characterizes the gas permeability, where D is the diffusion coefficient and S is the solubility. In a loading-unloading cycle, gas permeation only occurs in the unloading step driven by the pressure drop Δp inside the crater. Note that Δp is negative. The relative gas leakage is expressed as the following:

$$\frac{J}{V_0} = \int_0^{t_0} \frac{T}{T_0} \frac{-\Delta p(t) P_{Henry} A}{V_0 l} dt \tag{7. 19}$$

where J is the air flux volume, V_0 is the initial volume of the crater, A is the area of air/PDMS interface, T is the environment temperature, $T_0 = 273.15$ K, $\Delta p(t)$ is the pressure drop inside the crater that depends on time t, and t_0 is the time period of unloading. l represents the PDMS membrane thickness in common permeation tests. For cratered specimen, we choose $l = 6$ mm which is the shortest distance from crater surface to outer PDMS surface. In the experiments, we have $T = 20\,℃$, $A = 2\pi a^2$, $V_0 = 2\pi a^3/3$, $\alpha = 0.635$ mm, $\max(-\Delta p) \approx 0.2$ atm and $t_0 \leq 200$ s. According to [120],

$$P_{Henry} = \left(22.4 \frac{\mathrm{L}}{\mathrm{mol}}\right) \left(2 \times 10^{-12} \frac{\mathrm{mol}}{\mathrm{m \cdot s \cdot Pa}}\right) \tag{7. 20}$$

for CO_2/PDMS, which is usually higher than that of N_2/PDMS and O_2/PDMS based on the study of PDMS membranes in [121], and thus, can be used to estimate the upper bound of the relative gas leakage. However, this permeability is for PDMS with base-to-curing-agent mass ratio equal to 10:1. Considering the effect of curing agent ratio characterized in [122], we multiply P_{Henry} by a factor of 3 to approximate the gas permeability for PDMS with base-to-curing-agent mass ratio equal to 30:1. Herein, the estimated relative air flux is

$$\frac{J}{V_0} \leq \frac{T}{T_0} \frac{\max(-\Delta p)\, 3P_{Henry} A}{V_0 l} t_0 \approx 0.05 \ll 1 \tag{7. 21}$$

and therefore, the effect of gas permeation on suction force in our experiments is considered as negligible.

Chapter 8 Isolated Underwater Craters[4]

In this chapter, we follow the framework developed in Chapter 7 to analyze isolated craters underwater. We firstly focus on hemi-spherical craters. By using experimental, computational, and analytical methods, we characterize the relation between suction force and preload for liquid-filled hemi-spherical craters. For the sake of simplicity, we consider water as incompressible liquid, and apply the fluid cavity behavior in finite element simulation. However, by comparing experimental and simulation results, we find that, under large preload, the numerical control of the fluid cavity is no longer capable to model liquid-filled craters.

---

[4] Qiao S, Wang L, Ha K, Lu N. Suction Effects of Cratered Surfaces Underwater. to be submitted (Conducted the numerical simulations, experiments and wrote the analysis section in the paper)

8.1 PROBLEM DESCRIPTION

Similarly with air-filled craters, we consider a specimen containing a hemi-spherical crater with radius a at its bottom (Figure 8.1). The specimen rests on the flat bottom of a rigid container. The liquid inside the crater is the same as in the ambient environment, and it is characterized by the volume V_0, molecules N_0 and the hydrostatic pressure p_0 which can be written as

$$p_0 = p_a + \gamma_w h \tag{8.1}$$

where p_a is still the atmospheric pressure, γ_w is the specific weight of the liquid, and h is the distance from the cratered surface to the liquid surface. The suction effect of liquid-filled craters is realized in two stages as described in Section 7.1.

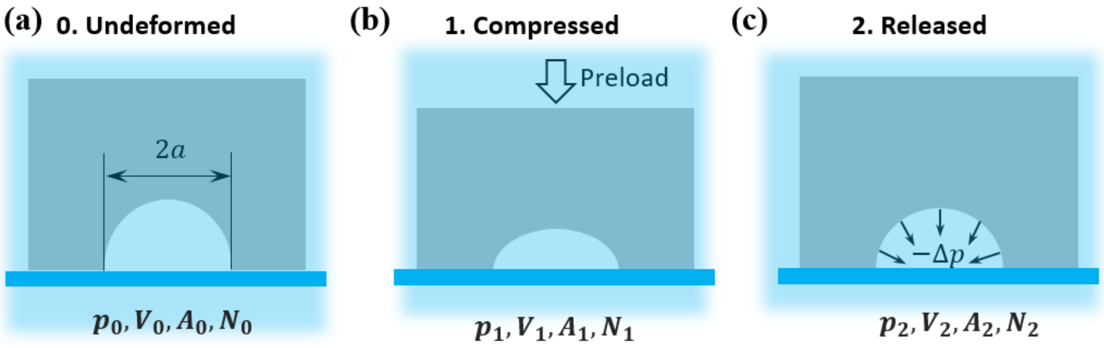

Figure 8.1 A loading-unloading cycle that produces suction force underwater: (a) A specimen with an isolated hemi-spherical crater of radius a resting on the flat bottom of a tank filled with liquid (blue); (b) The specimen is preloaded in compression and the liquid is squeezed out of the crater; (c) The preload is released, and the crater springs back, resulting in pressure drop in the crater. The symbols p, V, A and N denote the pressure, volume, projected area, and number of liquid molecules inside the crater at each state

A complete analysis of the two-stage process requires one to model the liquid flow. We avoid this task by adopting the following assumptions:

1. The liquid flows freely out of the crater upon loading, so that $p_1 = p_0$.
2. No liquid exchange takes place upon unloading, so that $N_1 = N_2$.
3. The entire process is isothermal and the liquid is incompressible, so that $V_1 = V_2$.

Note that the first two assumptions are essentially the same with those for air-filled craters.

8.2 HEMI-SPHERICAL CRATERS

In this section, following the analysis of air-filled craters, we use experimental, computational, and analytical approaches to study isolated hemi-spherical macroscopic craters filled with liquid.

8.2.1 Experimental Measurements

Since we are interested in characterizing the suction force induced by pressure drop inside the crater, which does not depend on the ambient environment, we filled the crater with incompressible liquid and performed the measurement in air. Using the same experimental setups for air-filled craters, we collected pull-off forces F' and F'' for liquid-filled craters at different preload ϵ.

In Figure 8.2, the suction force $F' - F''$ is plotted against the preload ϵ. Results corresponding to liquid-filled craters are plotted in red, and for comparison, results of air-filled craters are included and plotted in blue. Solid dots denote results measured by DMA while hollow dots are measured by MTS. For the same specimen, craters can produce stronger suction force when filled with liquid, or when larger compression is applied. At $\epsilon \approx 0.32$, for liquid-filled craters, we measured pull-off forces by both DMA and MTS, and the corresponding results are again in good agreement, which further justifies the consistence between the experiments performed via DMA and MTS.

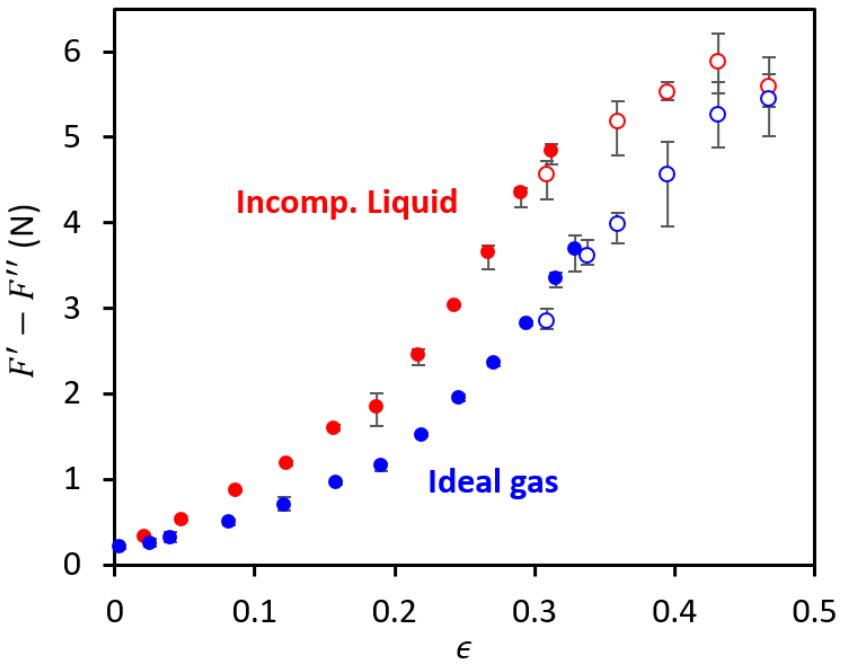

Figure 8.2 Comparisons of experimentally measured suction forces ($F' - F''$) of air-filled (blue markers) and liquid-filled (red markers) craters. Data obtained by DMA are represented by solid dots and MTS by hollow circles.

8.2.2 Finite Element Analysis

Following the framework developed in Chapter 7, we use incompressible Neo-Hookean model with shear modulus $\mu =$ 47.3 kPa to describe the specimen material. According to the third assumption, the liquid inside the crater was assumed to be incompressible, and its pressure during the second stage was controlled by the crater volume upon loading.

The finite element mesh formed by CAX4H elements is the same as shown in Figure 7.5a. When using the option *FLUID CAVITY, hydraulic behavior with infinity bulk modulus is applied.

In finite element analysis, during unloading, liquid-filled craters recover differently from air-filled craters, as shown in Figure 8.3. Figure 8.3 lists two sequences of deformed specimens in a loading-unloading test with ideal gas vs. liquid fillings. In the two sequences, craters are hemi-spherical with μ =47.3 kPa. The first and last panels in each sequence are the initial (before loading) and final (end of unloading) configurations, respectively. The third panels correspond to the end of loading with ϵ =0.35, and the rest are intermediate states. At the end of unloading, the finite element results indicate that the crater filled with ideal gas maintains the spherical symmetry, whereas the crater filled with incompressible fluid does not.

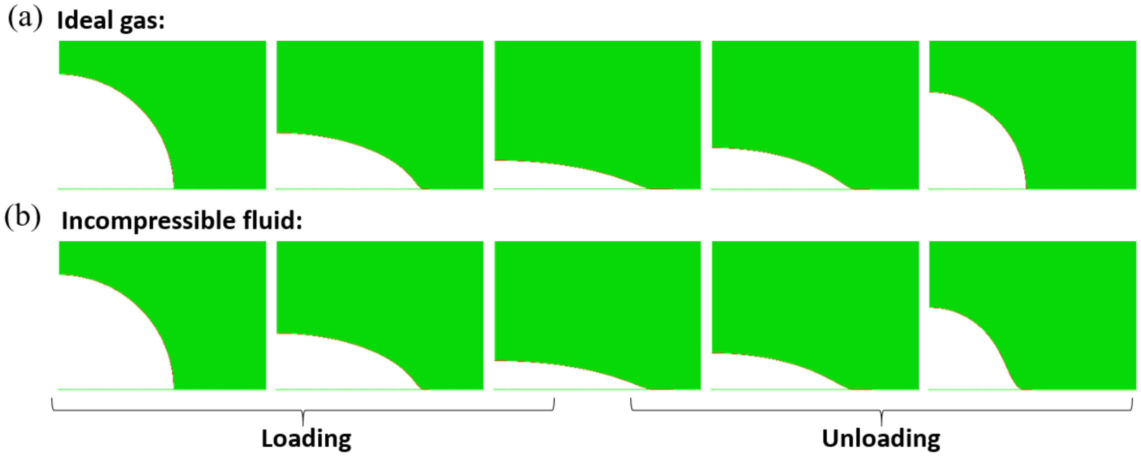

Figure 8.3 Deformation sequences of specimens in a loading-unloading test filled with (a) ideal gas, and (b) incompressible fluid

8.2.3 Linear Elasticity Analysis

In this section, we present linear elasticity analysis of suction force in liquid-filled craters based on Eshelby's formalism [115]. Applying the simplification used in Section 7.2.3, we consider a spherical cavity in an infinite specimen.

The computations of ΔV_1 and ΔV_2 are independent of fillings in the crater, which means for liquid-filled craters, we still have

$$\Delta V_1 = -\frac{3}{2}(1-\nu)\epsilon V_0 \tag{8.2}$$

and

$$\Delta V_2 = \frac{3}{4}\frac{\Delta p}{\mu}V_0 \tag{8.3}$$

where Poisson's ratio $\nu = 1/2$ is used.

Since the fluid in the cavity is incompressible and there is no fluid exchange during unloading, we have

$$\Delta V_1 = \Delta V_2 \tag{8.4}$$

Combing Eqns. (8.2) ~ (8.4), one obtains the pressure drop in the crater upon unloading

$$\Delta p = -\epsilon\mu \tag{8.5}$$

so that the resulting suction force upon unloading is

$$F = \epsilon\mu A_0 \tag{8.6}$$

8.2.4 Results

Consider hemi-spherical craters with μ =47.3 kPa. Different system parameters upon unloading as functions of ϵ are plotted in Figure 8.4: (a) normalized volume change $(V_0 - V_2)/V_0$, (b) normalized pressure drop $-\Delta p/p_a$, (c) normalized projected area A_2/A_0, and (d) normalized suction force $\tilde{F}$. Figures 8.4a and 8.4b show that craters of both fillings experience increase in volume change and pressure drop with growing ϵ, while the liquid-filled crater shows higher growth, which is a result of the stronger constraint of volume conservation, i.e. $V_1 = V_2$.

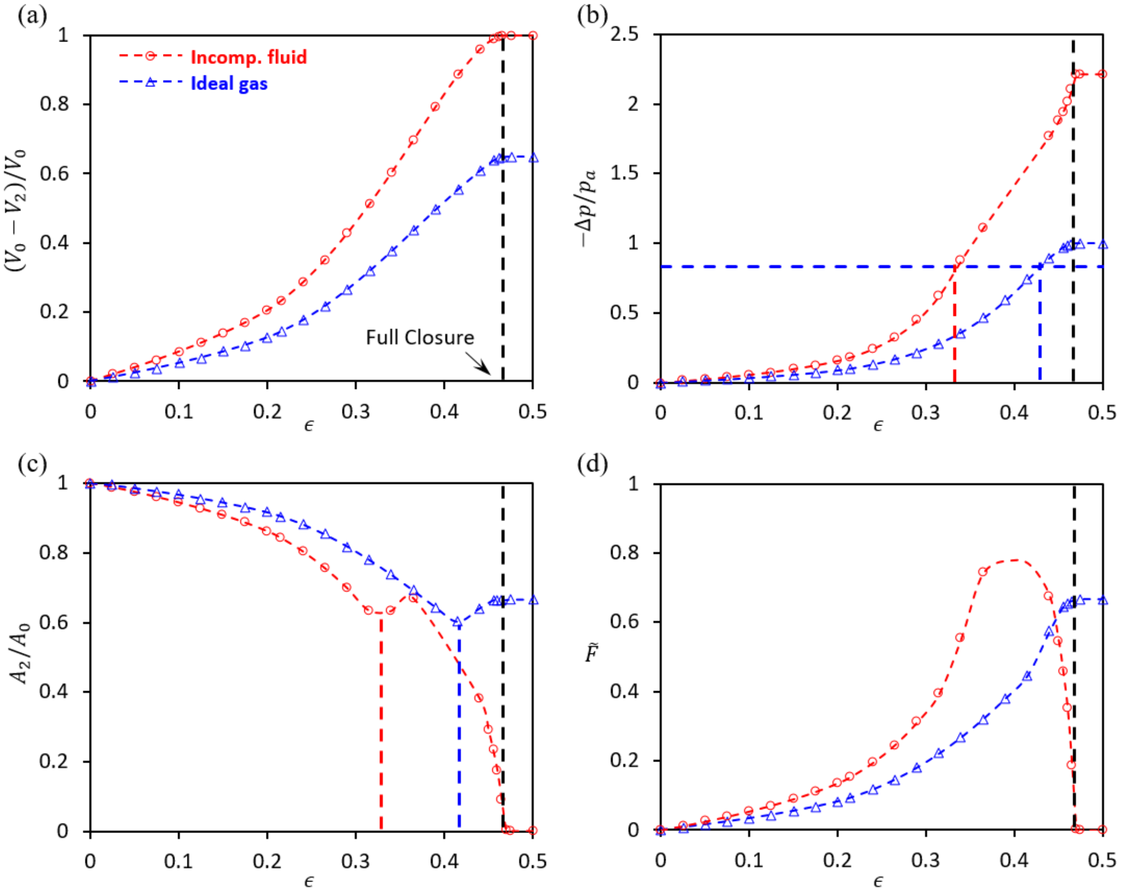

Figure 8.4 End results of the loading-unloading test are computed and plotted as functions of the preload ϵ: (a) normalized volume change $(V_0 - V_2)/V_0$, (b) normalized pressure drop $-\Delta p/p_a$, (c) normalized projected area A_2/A_0, and (d) normalized suction force $\tilde{F} = -\Delta p A_2/(p_a A_0)$. Craters filled with incompressible fluid are represented by red dotted curves and ideal gas by blue

At critical pressure drop Δp_c, the spherical symmetry of the recovered hemispherical crater breaks down upon unloading for both air-filled craters and liquid-filled craters. The corresponding critical preload ϵ_c is 0.33 for liquid-filled craters, as indicated by vertical dashed red lines in Figures 8.4b and 8.4c, respectively, which is smaller than that for air-filled craters. At $\epsilon = \epsilon_c$, an increasing trend of A_2/A_0 is observed for both liquid-filled and air-filled craters (Figure 8.4c). However, unlike air-filled craters, the instability induced increase in A_2 does not last for liquid-filled craters, since the volume conservation constraint also becomes more and more stronger with increasing preload ϵ, and eventually overwhelms other factors, leading to smaller and smaller projected area, as shown in Figure 8.4c.

When plotting the normalized suction force $\tilde{F}$, the enhanced pressure drop and the compromised projected area mutually produce a $\tilde{F}$ that varies non-monotonically with ϵ in liquid-filled craters (Figure 8.4d). Full closure of the crater is reached at $\epsilon = 0.47$ for both air-filled craters and liquid-filled craters, as indicated by vertical dash black lines in Figures 8.4a ~ 8.4d, respectively. At full closure, zero suction force is produced in liquid-filled crater, whereas air-filled crater can reach maximum suction force $\tilde{F}$ (Figure 8.4d). The drastic difference of the suction force between air and liquid-filled craters at full closure originates from the different pressure-volume behaviors of the two types of fluids.

Comparisons of experimental (circular markers), simulation (solid curves) and analytical (dashed curves) results of suction force are shown in Figure 8.5, in which results corresponding to liquid-filled craters are plotted in red, and air-filled craters are in blue. For $0 \leq \epsilon \leq 0.3$, experimental and simulation results are in good agreement for craters filled with both liquid and air, which validates the use of the modeling assumptions. Similar with air-filled craters, analytical result of liquid-filled craters only agrees well with experimental measurements under small preload, say $\epsilon < 0.1$.

Under large preload, especially when craters reach full closure upon loading, finite element simulation shows considerable discrepancy from experimental results for liquid-filled craters. In Section 7.2.4, we discovered that, for air-filled craters, the discrepancy between finite element simulation and experimental results can be fully explained by the difference in $-\Delta p A_2$ and $F' - F''$. However, this explanation is not enough for liquid-filled craters.

For liquid-filled craters, at full closure ($\epsilon > 0.47$), suction force $-\Delta p A_2$ is found to be zero in finite element simulation, whereas $F' - F'' = 5.6\,\mathrm{N}$ is obtained from experiment. In experiments, full closure upon loading indicates vacuum inside the crater. During unloading, the crater simply springs back subjected to vacuum, which creates finite A_2. Under vacuum, the recovery of the crater does not depend on what fillers are once inside the crater, which explains the similar $F' - F''$ at full closure for both air-filled craters and liquid-filled craters. However, in finite element simulation, the incompressible fluid assumption is ensured throughout a loading-unloading cycle of liquid-filled craters, so that at full colure, $V_1 = 0$ is achieved which leads to $V_2 = 0$, $A_2 = 0$, and therefore, suction force $-\Delta p A_2 = 0$, which is contradictory to experiments. This contradiction suggests that, the numerical control, $V_1 = V_2$, is not applicable at full closure. In addition, vaporization of the liquid at large $-\Delta p$ may also break the incompressible assumption [123], and causes discrepancy between finite element simulation and experimental results. Thus, for liquid-filled craters, the use of finite element simulation under large preload is limited. For the specimens used in our studies, the deviation between finite element simulation and experiments occurs at $\epsilon \approx 0.3$. One should note that the deviation may occur at different preload ϵ if the specimens are made of different materials.

Compared to air-filled craters, besides the traction-separation behavior of the specimen/platform interface, one also needs a complete model of the liquid under low pressure, in order to accurately predict the suction force of liquid-filled craters at pull-off. This task is out of the focus of our study. So, in the rest of this chapter, we still apply volume conservation $V_1 = V_2$ in finite element simulations, and neglect vaporization in liquid-filled craters. Readers should be aware of that, by doing so, the simulation results may not be accurate at large preload.

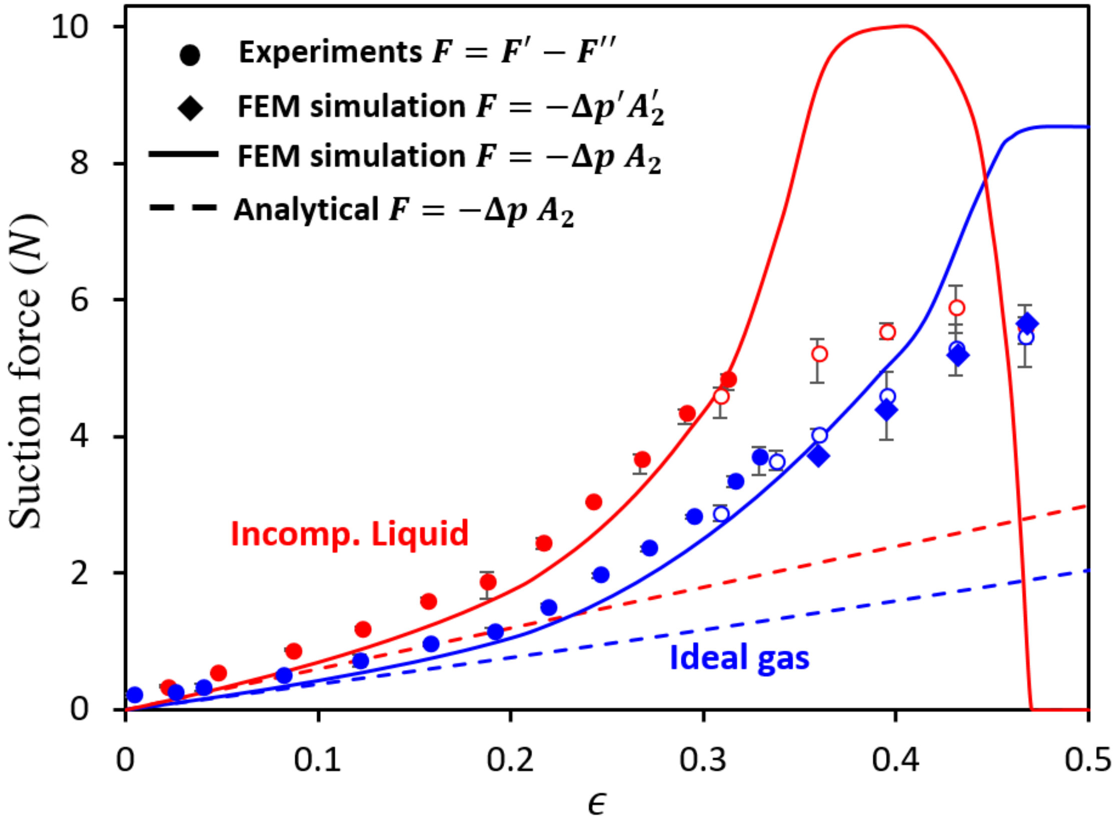

Figure 8.5 Comparisons of suction forces obtained by experimental measurements (circular markers), analytical modeling (dashed curves) and finite element simulation (solid curves and diamond markers). Craters filled with incompressible fluid are represented by red and ideal gas by blue

8.3 SPHERICAL-CAP-SHAPED CRATERS

In this section, we extend the simulation approach to spherical-cap-shaped (SCS) craters (Figure 8.6a) that are filled with incompressible liquid.

According to dimensional analysis, when the crater is filled with incompressible fluid, Δp is proportional to the specimen stiffness μ. Instead of applying the normalization used for air-filled craters (Eq. (7.13)), we normalize the suction force upon unloading as the following

$$\hat{F} = -\frac{\Delta p A_2}{\mu A_0} \tag{8.7}$$

where A_0 is the projected area of the crater at initial status. Notice that $\hat{F}$ only depends on the crater aspect ratio α ($\alpha = b/a$) and preload ϵ. Thus, our focus is on maximizing the suction force $\hat{F}$ by optimizing the crater shape and preload.

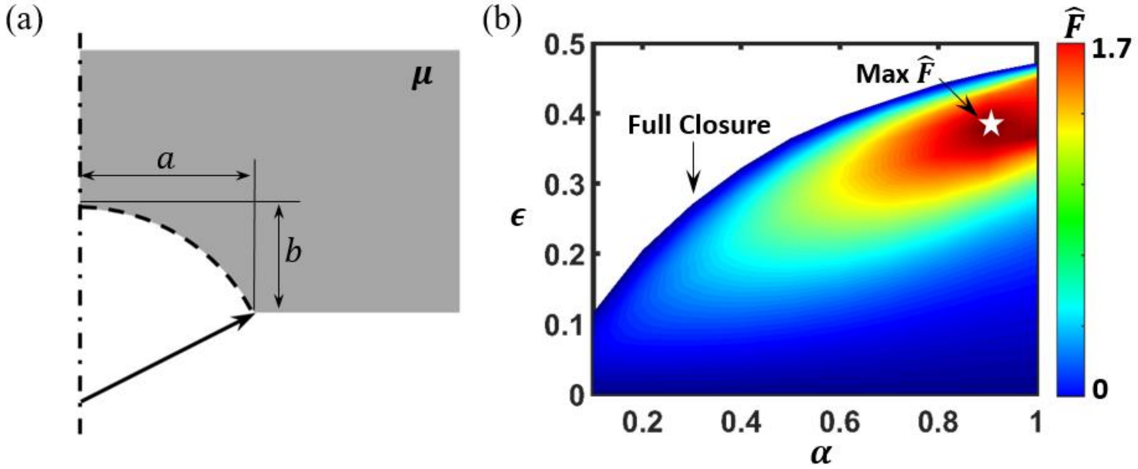

Figure 8.6 (a) A schematic of the spherical-cap-shaped (SCS) crater. (b) A contour plot for the normalized suction force $\hat{F}$ as a function of α and ϵ

A contour plot for the normalized suction force $\hat{F}$ as a function of α and ϵ is presented in Figure 8.6b. This plot was generated using finite element simulation results. The plot clearly demonstrates that large $\hat{F}$'s are realized by specimens with large aspect ratio α and moderate preload ϵ. The dependence of $\hat{F}$ on α and ϵ is not monotonic. For sufficiently large ϵ, craters go to full closure upon loading that leads to

$$V_1 = V_2 = 0, \text{ and } A_2 = 0 \tag{8.8}$$

such that $\hat{F} = 0$ by definition. Further increasing the preload beyond this point will not help. The optimal suction force $\hat{F}$ is characterized by α =1 under ϵ =0.4. Again, at full closure, incompressible fluid in finite element simulation is no longer accurate to model realistic liquids.

8.4 REINFORCEMENT LAYER

According to Eq. (8.7), we have $F = \hat{F}\mu A_0$ so that stiff specimens result in large suction forces. However, it also takes more effort to achieve the same preloaded compression ϵ with stiff specimen. Besides, many biomedical applications involve soft polymers. To resolve this issue, similar with what we did for air-filled craters, we consider soft specimens with craters reinforced by thin stiff layers (Figure 8.7a), with the expectation that such layers would result in the larger $\hat{F}$.

We considered reinforcement layers made of incompressible Neo-Hookean materials, so that the layers were characterized by the dimensionless parameters $\alpha' = t/a$ and $\beta' = \mu_l/\mu$, where t and μ_l are the layer thickness and shear modulus (Figure 8.7a), respectively.

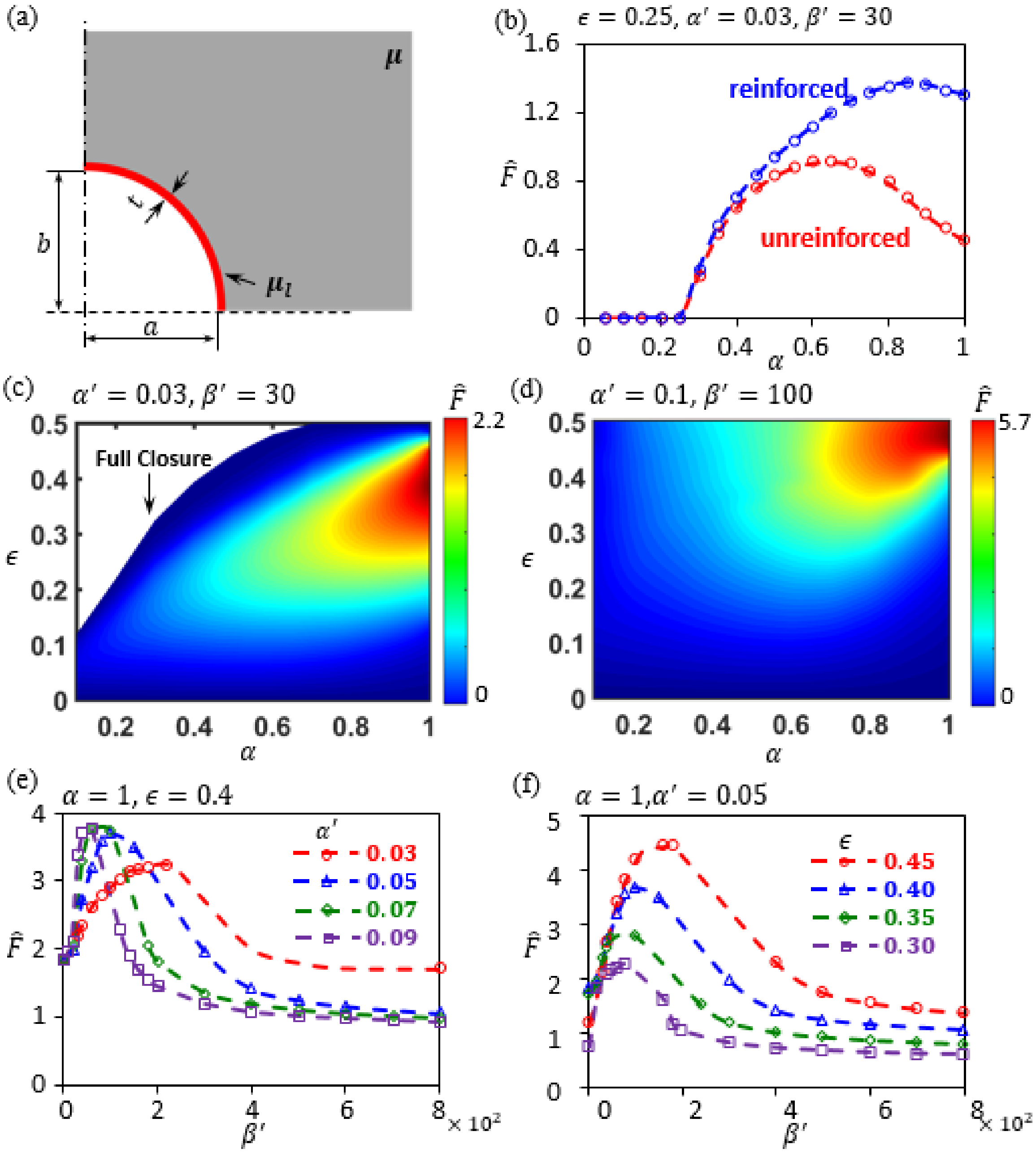

Figure 8.7 (a) A schematic of a SCS crater reinforced by a thin stiff layer (red). (b) A comparison of suction forces $\hat{F}$ of unreinforced (red) and reinforced (blue) craters. Contour plots of $\hat{F}$ of reinforced SCS craters with different reinforcing layers: (c) t/a =0.03 and μ_l/μ =30, and (d) b/a =0.05 and μ_l/μ = 100. Suction forces $\hat{F}$ of reinforced hemi-spherical craters as functions of μ_l/μ with (e) t/a =0.03, 0.05, 0.07 and 0.09 under ϵ =0.4, and (f) t/a =0.5 under ϵ =0.30, 0.35, 0.40 and 0.45

To illustrate the effectiveness of the reinforcement layer, we first compared the normalized suction force between reinforced and unreinforced SCS craters with aspect ratios varying from 0.1 to 1. The numerical simulation results of $\hat{F}$ are presented as circular markers with dashed guiding lines in Figure 8.7b. Specimens are loaded with $\epsilon = 0.25$, and the chosen reinforcement layer has $\alpha' = 0.03$ and $\beta' = 30$. In this comparison, significant enhancement can be obtained through reinforcement, especially for deep craters ($0.6 \leq \alpha \leq 1$). Note that at fixed ϵ, the normalized suction force $\hat{F}$ of both reinforced and unreinforced craters behaves non-monotonically against the crater aspect ratio α; optimized $\hat{F}$ is achieved at $\alpha =0.65$ with $\hat{F} = 0.91$ for unreinforced craters, and at $\alpha =0.85$ with $\hat{F} =1.38$ for reinforced craters. An amplification factor 1.38/0.85≈1.62 was achieved for this case.

To reduce the size of the parametric space, we chose two different reinforcing layers to obtain contour plots of $\hat{F}$ for reinforced SCS craters numerically. In Figures 8.7c and 8.7d, we limit ϵ to be $0 \leq \epsilon \leq 0.5$, and set $\alpha =0.03$ and $\beta =30$, and $\alpha =0.05$ and $\beta =100$, respectively. Comparing with Figure 8.6b, the reinforcing layers lead to higher ϵ to achieve fully closed craters upon loading, while upon unloading, reinforced craters are capable of producing higher suction force, especially in Figure 8.7d, whose reinforcement is significantly strong. For the chosen reinforcing layers, optimal suction forces are characterized by $\alpha = 1$ under $\epsilon = 0.39$ and 0.47 in Figures 8.7c and 8.7d, respectively. Note that the optimal suction force $\hat{F}$ of unreinforced SCS craters is characterized by $\alpha =1$ under $\epsilon =0.4$.

To further study the effect of reinforcement, we focus on hemi-spherical craters, i.e. $\alpha =1$, and constructed different sets of reinforcing layers with various β'. Figure 8.7e shows comparisons of suction forces $\hat{F}$ as functions of β' with $\alpha' =0.03$, 0.05, 0.07 and 0.09 under $\epsilon =0.4$. We see that large $\hat{F}$ only involves reinforcing layer with stiffness

$30 < \beta' < 300$. This is because reinforcing layers are too soft to reach optimal $\hat{F}$ when $\beta' < 30$, and are too stiff to deform during loading when $\beta' > 300$. Besides, thick reinforcing layers require relatively softer stiffness to achieve optimal $\hat{F}$. By setting $\alpha' =$0.05 and $\epsilon =$0.30, 0.35, 0.40 and 0.45, we obtained similar $\hat{F}{\sim}\beta'$ relations with different magnitude of $\hat{F}$. In the chosen range of ϵ, stronger compression in the loading stage results in larger $\hat{F}$.

Chapter 9 Double-Chamber Craters

In Chapters 7 and 8, we considered isolated craters with single chamber, which requires vent hole to generate suction. Compared with such craters, double-chambered craters were proposed in the literature in which case vent holes are no longer needed in producing suction force, which broadens potential applications of cratered surfaces. In this chapter, we implement the numerical approach developed for single-chamber craters to study double-chamber craters. The geometry of double-chamber craters used in this chapter is adopted from the work of Baik et al (2017). We conclude from our nonlinear finite element modeling that such double chamber crater design is not able to generate meaningful suction forces, which contradicts with the literature. But no settlement is available at this point.

9.1 MECHANISM OF DOUBLE-CHAMBER CRATERS

An essential step in producing suction force in single-chamber craters is squeezing fluid out of the crater in loading stage, which creates potential of pressure drop inside the crater in unloading stage. This is realized in Chapters 7 and 8 by incorporating the specimen with vent holes. However, incorporating craters with vent holes may not be possible in many applications.

Real suction cups of octopus vulgaris contain two chambers that are connected through an orifice as shown in Figure 9.1. For the sake of simplicity, we use C_1 and C_2 to denote the acetabulum chamber (upper chamber), and the infundibulum chamber (lower chamber), respectively. The boxed area in Figure 9.1a shows a protuberance locates on the acetabular roof, which plays an important role in the sucker adhesion and detachment. In the work of Tramacere et al (2013) [112], a four-phase process was proposed to explain the adhesion mechanism in octopus vulgaris suckers, as illustrated in Figure 9.2 and summarized by the following:

Phase 1: forming of a tight seal that prevents water from leaking at the rim.

Phase 2: contraction (black arrows) of acetabular radial muscles creates suction and moves water from C_1 toward C_2 (blue arrows).

Phase 3: meridional muscles of acetabulum contract (black arrows), allowing the protuberance make contact with the side walls of the orifice; meanwhile, the acetabular radial muscles are still contracted (gray arrow). A torus of water is created in C_2 around the protuberance itself.

Phase 4: acetabular radial and meridional muscles stop to contract. The protuberance is passively kept in contact with the upper part of the side walls of the orifice, due to the cohesive force and friction, which balance the elastic restoring force of acetabular protuberance.

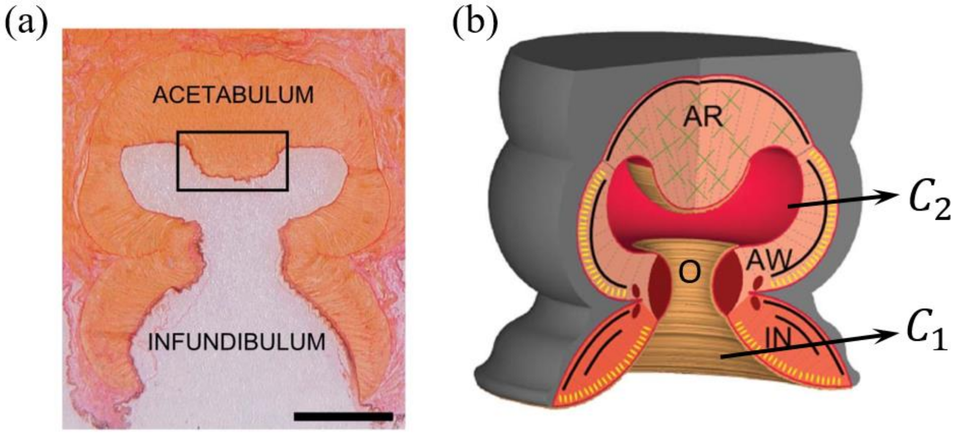

Figure 9.1 (a) Histological transversal sections of octopus vulgaris sucker (the scale bar equals 2.5 mm) (b) 3D schematic of the octopus suckers (AR, acetabular roof; AW, acetabular wall; IN, infundibulum; O, orifice) (adopted from Ref. [112] with permission)

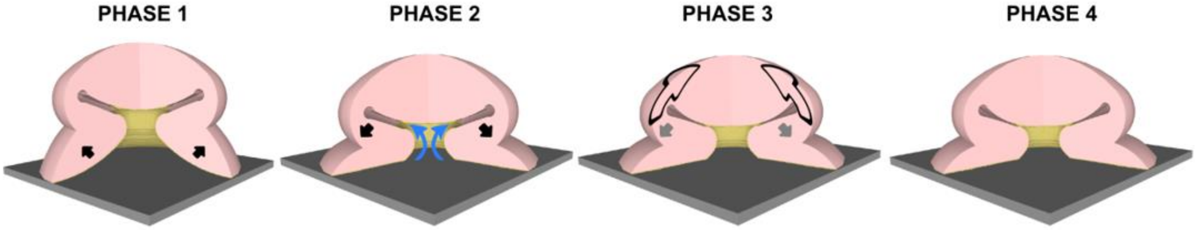

Figure 9.2 Schematic views, in four phases, of the adhesion mechanism proposed for the octopus vulgaris sucker by Tramacere et al (adopted form Ref. [112] with permission)

According to this process, the amount of water in chambers C_1 and C_2 is fixed once contact with substrate is made. Instead of being vented out of the sucker, water is vented form C_1 into C_2 by contraction of acetabular radial in Phase 2. By the end of Phase 4, due to elastic restoring, pressure drops in C_1 but increases in C_2, which results the suction force over the interface between chamber C_1 and substrate. Since the orifice connecting chambers C_1 and C_2 is blocked by the protuberance in Phase 3, pressure increase in C_2 does not affect the pressure drop in C_1.

In 2017, Baik and his colleagues created passive double-chamber craters on polymer layers by adding protuberance to cylindrical-shaped-craters (Figure 9.3), and observed significantly improved adhesion strength in the cratered surface. Unlike octopus vulgaris suckers, whose deformation is actively controlled through contraction/relaxation of muscles, artificial craters only deform under external load. Thus, the explanation of the adhesion mechanism of passive double-chamber craters differs from that of active craters. The adhesion mechanism given by Baik et al is illustrated in Figure 9.4 and summarized by the following (similarly, the upper and lower chambers in the design of Baik are also named as C_1 and C_2, respectively):

Stage I: forming contact with a substrate through an applied preload.

Stage II: under compressive load, the crater deforms and water flows from chamber C_1 into chamber C_2.

Stage III: remove the applied load; meanwhile, elastic restoring induces pressure drop in chamber C_1 and increase in chamber C_2.

Following this process, we implement a numerical approach in Abaqus to study the relation between suction force produced in chamber C_1 and preload ϵ.

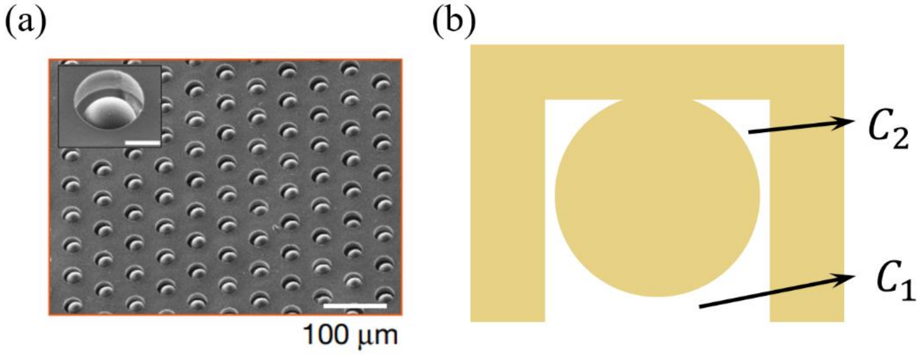

Figure 9.3 (a) SEM image of an array of micro-craters with protuberance-like dome-shaped structures (scale bar in the inset represents 15 µm) (adopted from Ref. [25] with permission, Copyright (2017) Springer Nature) (b) Side view of the double-chamber crater designed by Baik et al

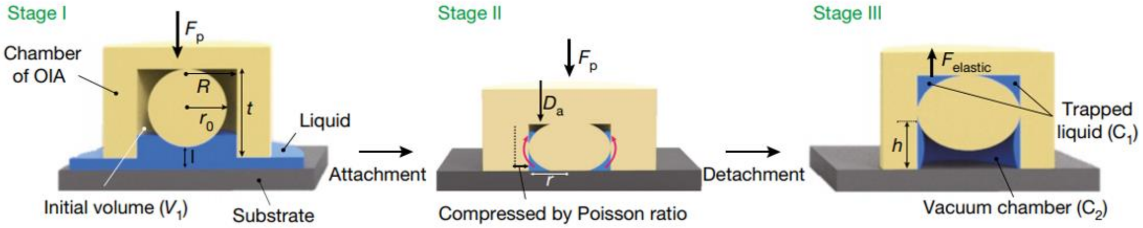

Figure 9.4 Schematic views, in three stages, of the adhesion mechanism proposed for the passive double-chamber craters by Baik et al (adopted from Ref. [25] with permission, Copyright (2017) Springer Nature)

9.2 FINITE ELEMENT ANALYSIS

This section provides details of simulating double-chamber craters in Abaqus. The crater design is adopted from Baik et al (2017). A finite element mesh formed by CAX4H elements is shown in Figure 9.5, where the crater is cylindrical shape with height H and radius r_0, and the protuberance is spherical shape with radius R_0 and separation s from the substrate. The specimen/substrate interface is considered to be friction in order to model the adhesion process in Figure 9.4.

First, we apply compression from far field in Z direction, and identify ϵ_a, the nominal strain in Z direction, at which contact of the protuberance and the sidewall occurs. During this step, before the contact sets in, chambers C_1 and C_2 are connected, and thus, are treated as a single fluid cavity. At $\epsilon_z = \epsilon_a$, the contact sets in, and the closest two nodes from surfaces of the protuberance and the sidewall are identified as Node-1 and Node-2, respectively, as given in Figure 9.6.

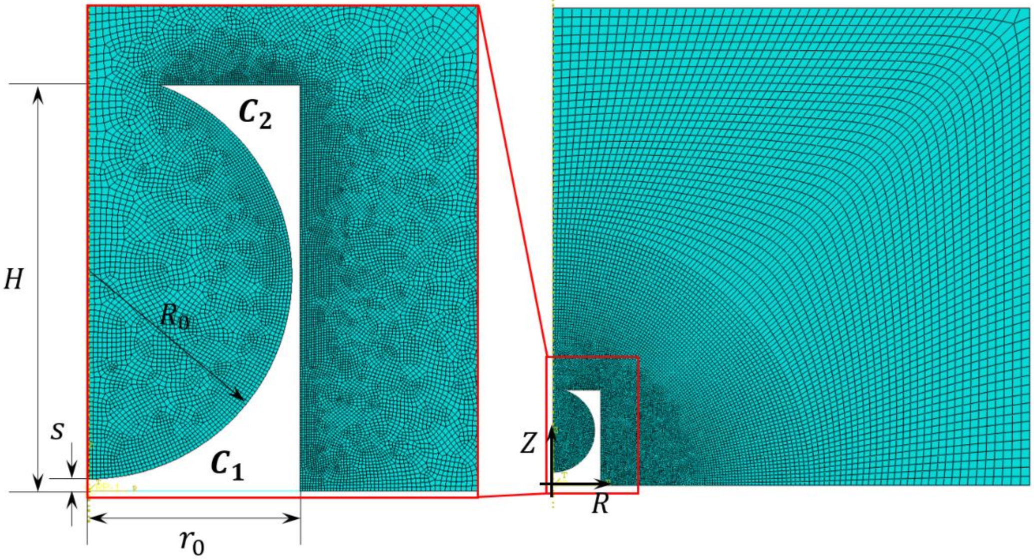

Figure 9.5 A finite element mesh for an axisymmetric double-chamber crater with protuberance

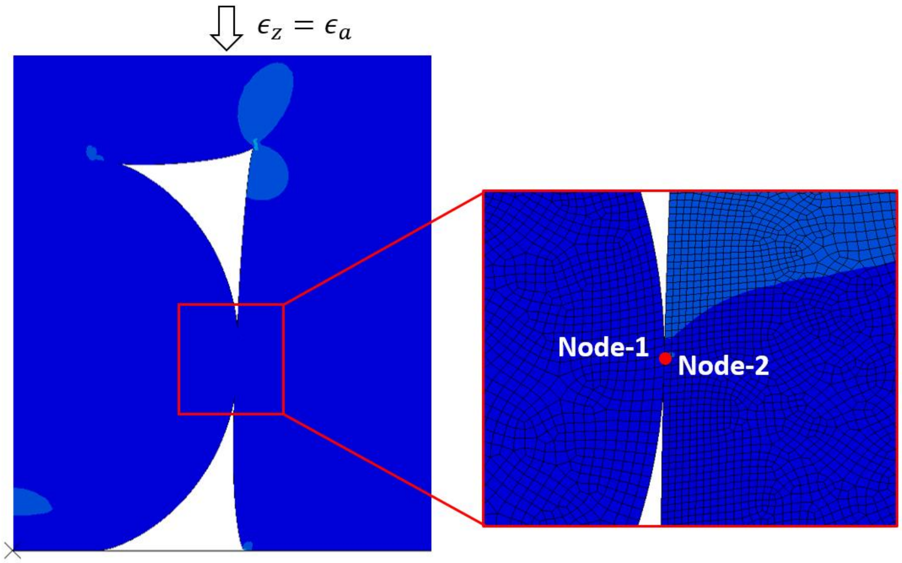

Figure 9.6 At $\epsilon_z = \epsilon_a$, the contact between the protuberance and the sidewall occurs

Second, we create another model with the same mesh, and an extra membrane element connecting Node-1 and Node-2, as shown in Figure 9.7. The membrane element acts as a virtual surface that separates chambers C_1 and C_2. By using *FLUID CAVITY option, the magenta edges in Figure 9.8 define the boundaries of two fluid cavities representing chambers C_1 and C_2, respectively. "RF-i" denotes the reference point of the fluid cavity of chamber C_i ($i = 1, 2$). To make the connectivity between chambers C_1 and C_2 switchable, fluid exchange is defined between the two chambers which follows

$$(p_{c1} - p_{c2})A = C_V \dot{m} \tag{9.1}$$

where p_{ci} is the pressure in chamber C_i, A is the predefined effective exchange area, C_V is the fluid exchange coefficient, and $\dot{m}$ is the mass exchanging rate. In addition, the membrane element stiffness is set to be small enough to minimize its mechanical effect.

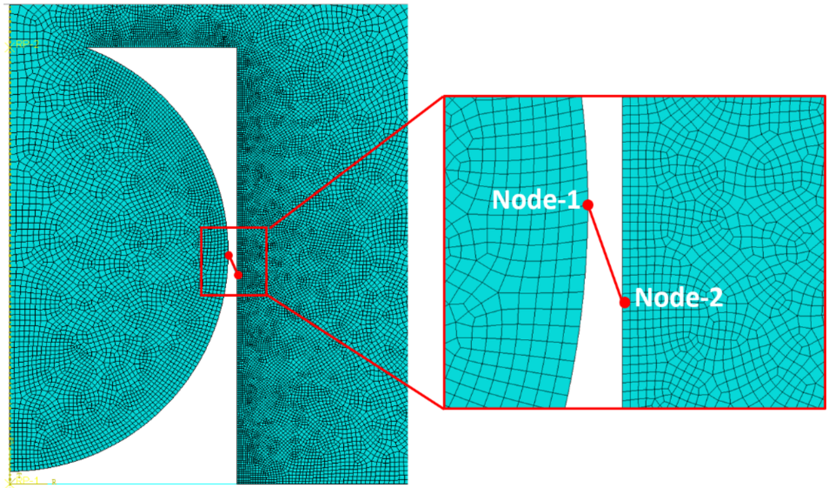

Figure 9.7 A second model with a membrane element defined by Node-1 and Node-2

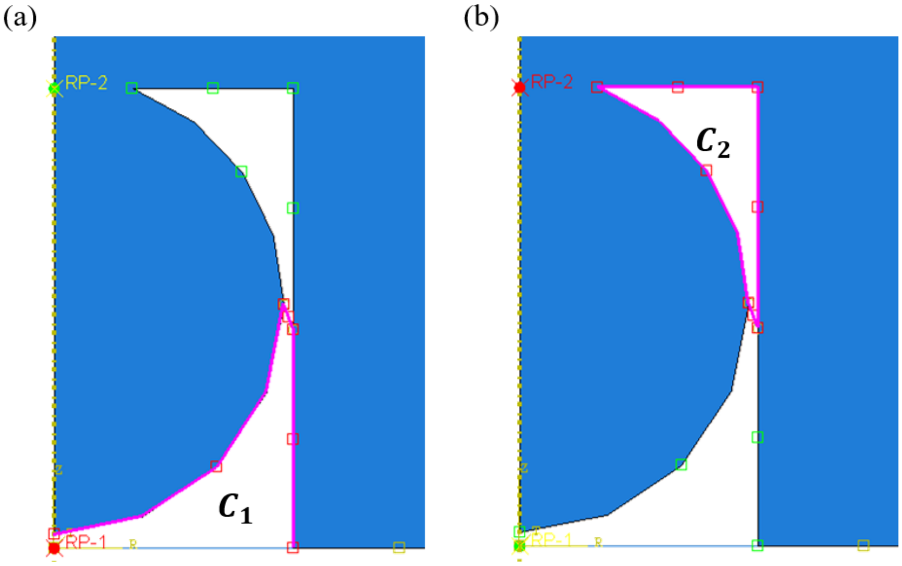

Figure 9.8 Schematic of definition of fluid cavities for (a) chamber C_1, and (b) chamber C_2 in Abaqus. Magenta edges define the boundaries of each cavity, and "RF-i" defines the reference point of chamber C_i ($i = 1,2$)

A loading-unloading cycle of the double-chamber crater is realized in Abaqus through the following steps:

Step 1: ramp compression strain ϵ from 0 to ϵ_0 ($\epsilon_0 \geq \epsilon_a$). Set $C_V \ll 1$ for $\epsilon < \epsilon_a$, and $C_V \gg 1$ for $\epsilon \geq \epsilon_a$, so that the two chambers behave as being connected before the protuberance and the sidewall contacts, and as being disconnected after the contact blocks fluid exchange.

Step 2: unload the specimen from ϵ_0 to 0 with $C_V \gg 1$.

In Step 1, fluids flows freely from chamber C_1 to chamber C_2 when $\epsilon < \epsilon_a$, and we have $p_{c1} \approx p_{c2}$ since $C_V \ll 1$. Once the contact between the protuberance and the sidewall occurs, the two chambers are disconnected by setting $C_V \gg 1$, and fluid pressure changes independently in each chamber, i.e. $p_{c1} \neq p_{c2}$. In Abaqus, the contact between protuberance and sidewall is defined as frictionless in tangential direction of the surface, and non-separable in the normal direction of the surface.

9.3 DISCUSSIONS ON FLUID EXCHANGE

According to Eq. (9.1), $C_V \ll 1$ implies $p_{c1} \approx p_{c2}$ so that chambers C_1 and C_2 are effectively "connected". Also, $C_V \gg 1$ indicates $\dot{m} \approx 0$ so that chambers C_1 and C_2 are effectively "disconnected". To validate it, we studied 3 double-chamber craters with the same mesh but different settings in Abaqus:

1. A double-chamber crater without the membrane element. Chambers C_1 and C_2 are defined as a single fluid cavity.
2. A double-chamber crater with the membrane element. Chambers C_1 and C_2 are defined as two fluid cavities, but fluid exchange between them is deactivated.
3. A double-chamber crater with the membrane element. Chambers C_1 and C_2 are defined as two fluid cavities, and fluid exchange between them is activated.

The first two models corresponds to situations that chambers C_1 and C_2 are connected and disconnected, respectively. Based the aforementioned method, by setting $C_V = 0$ or $C_V \gg 1$, the third model should recovery the first and the second model, respectively.

In these Abaqus models, we chose $R_0 = 0.5H$, $r_0 = 0.52H$, $s = 0.03H$, and modeled the specimen using incompressible Neo-Hookean material law with $\mu = p_a$. Fluid behavior follows ideal gas law in each fluid cavity. A compressive strain $\epsilon_z = 0.2$ was applied, and its corresponding critical load ϵ_a was found to be 0.13. At $\epsilon_z = 0.2$, $(p_{c1} - p_{c2})/p_a$ and $(V_{c1} - V_{c2})/V$ were collected from the three models and plotted in Figure 9.9, where V_{ci} represents the volume of chamber C_i, and V is the initial volume the crater. The dashed green and red lines represent results obtained from Model 1 and Model 2, respectively. Figure 9.9 shows that Model 3 recovers Model 1 when $C_V \leq 0.1$ and Model 2 when $C_V \geq 10^4$, respectively, which agrees with our analysis, and thus, validates our use of fluid exchange.

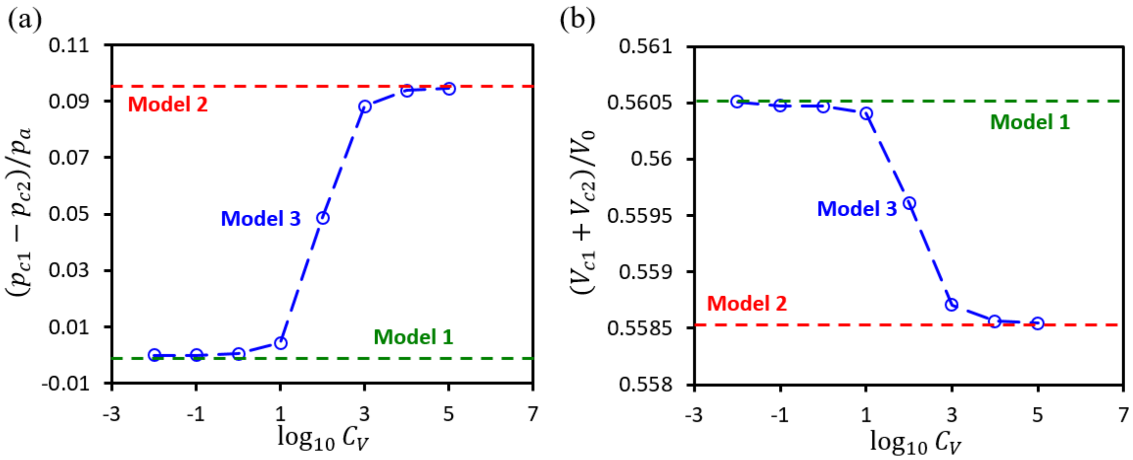

Figure 9.9 Comparison of (a) $(p_{c1} - p_{c2})/p_a$ and (b) $(V_{c1} - V_{c2})/V$ at $\epsilon_z = \epsilon_a$ from the three models with the same mesh but different settings in fluid cavities and fluid exchange property

9.4 RESULTS

In this section, we implement the loading-unloading cycle of the double-chamber crater in Abaqus. The crater is designed with $R_0 = 0.5H$, $r_0 = 0.52H$, $s = 0.03H$, and the specimen is modeled as incompressible Neo-Hookean material law with $\mu = p_a$. Fluid behavior follows ideal gas law. The applied maximum compression strain is 0.14, greater than its ϵ_a which is 0.13.

Figure 9.10a plots the computed pressure change in each chamber against external load ϵ_z. Figure 9.10b shares the same content with Figure 9.10a but displays smaller range of ϵ_z: $0 \leq \epsilon_z \leq 0.05$. Red and blue arrows in Figure 9.10b denote the pressure change in loading and unloading steps, respectively. Both chambers start with $p_{ci} = p_a$. $C_V = 0.01$ is used for $\epsilon_z < \epsilon_a$ in loading step, and $C_V = 10^4$ is for $\epsilon_z > \epsilon_a$ as well as the whole unloading step. Upon unloading, one obtains $p_{c1} = 0.985p_a$ and $p_{c2} = 1.02p_a$ which agrees with our analysis that pressure drops in chamber C_1 whereas increases in chamber C_2. However, the corresponding suction force $\tilde{F}$ is only $0.015 \ll 1$, which is too small.

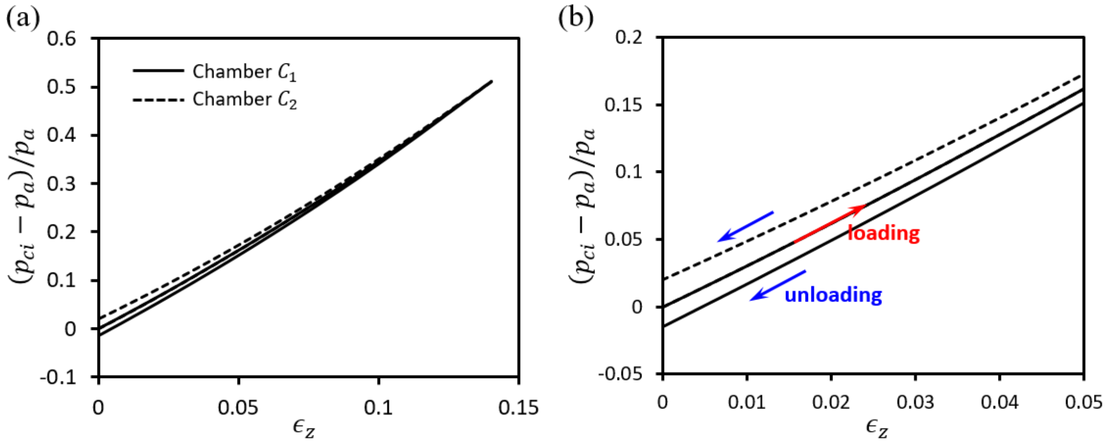

Figure 9.10 (a) Computed pressure change $(p_{ci}-p_a)/p_a$ in chambers C_1 (solid curve) and C_2 (dashed curve) against external load ϵ_z. (b) Same content with (a) but smaller range of ϵ_z. Red and blue arrows denote the loading and unloading steps, respectively.

The computed $\tilde{F}$ implies that suction force is successfully produced through the double-chamber design proposed by Baik et al. However, the resulted suction force is too weak to be applicable, which contradicts to the observation in [25]. This may be induced by the followings:

1. Contact between the protuberance and the sidewall is defined as non-separable which may differ from that in experiments from [25].
2. In the Abaqus model, fluid exchange is not allowed once contact between the protuberance and the sidewall sets in. However, in experiments, fluid exchange may still occur if small channels are developed over the protuberance/sidewall interface.

Chapter 10 Conclusions and Outlook

The last chapter summarizes this thesis work and proposes suggested directions for future research.

10.1 SUMMARY AND CONCLUDING REMARKS

In this dissertation, we work on fundamental studies of fluid-induced large deformation at soft material interfaces. Two topics are included: blisters where both the blister layer and substrate are soft materials, and dry adhesives enabled by cratered surfaces on soft matrices.

Blisters on soft material interfaces break the conformal contact between the blister layer and substrate which degrade the functionality in applications of thin film electronics. For example, sweating or bleeding induced blisters in epidermal or in-vivo electronics may lead to higher noise-to-signal ratio and even dysfunction of the device. We presented a nonlinear membrane theory to model the elastic layer and various types of boundary conditions were studied for blisters on rigid substrate. To characterize blisters on soft substrate, we formulated the corresponding boundary value problem and developed a numerical approach to solve it. We validated our numerical approach by studying the elasto-capillary wetting problem, which represents the situation that the blister layer has zero stiffness. Special attention was paid to the delamination propagation of a blister. It was found that, for blister layers made of non-strengthening material, delamination propagation can be avoided.

Cratered surfaces in soft matrices are capable of producing suction-enabled adhesion, which can be used as reusable adhesives. The good reusability may allow researchers in thin film electronics to reuse their devices, and therefore, dramatically lower the cost. We analyzed the suction-enabled adhesion of cratered surfaces both in ambient and underwater. Both experimental and simulation results focused on specimens resting on frictionless substrates. We restricted ourselves to isolated macroscopic craters, for which surface tension and other microscopic mechanisms were assumed to be negligible. We found that

- Craters are capable of producing stronger suction force underwater rather than in air.
- In stiff matrix, one can realize large suction forces by choosing deep craters and applying moderate preload.
- In soft matrix, large suction forces require crater reinforcement.
- Reinforced craters capable of realizing large suction forces often involve moderately stiff reinforcing layers.

10.2 SUGGESTIONS FOR FUTURE WORK

Theoretical Modeling of Blisters

In application, the initial delamination of a blister may not be circular, so that the axisymmetry is no longer applicable, and a 3D formulation is needed. In addition, the adhesion between the blister layer and substrate may be neither isotropic, nor homogeneous. Thus, instead of being constant, the interface energy density $\Delta\gamma$ should be considered as a function of position, i.e.

$$\Delta\gamma = \Delta\gamma(\boldsymbol{x}) \qquad \forall \boldsymbol{x} \in \Gamma_0^{\mathrm{s}} \tag{10.1}$$

Besides, the presented nonlinear membrane theory is derived by using the deflection of the middle layer (r, z) to calculate the total strain energy stored in the blister layer, i.e.

$$U_f = 2\pi t_0 \int_0^{R_0} W\left(r_f, z_f, r_f', z_f'\right) R dR \tag{10.2}$$

where only the first order derivatives of deflection functions, $r_f'(R)$ and $z_f'(R)$, are involved. The corresponding kinetic relations lead to

$$W\left(r_f, z_f, r_f', z_f'\right) = W(\lambda_r, \lambda_\theta) \tag{10.3}$$

in which bending energy vanishes. However, for thick layers, bending energy could be comparable with stretching energy even at large central deflection. In order to take bending energy into consideration, higher order derivatives of $r_f(R)$ and $z_f(R)$ are required, i.e.

$$U = 2\pi t_0 \int_0^{R_0} W\left(r_f, z_f, r_f', z_f', r_f'', z_f''\right) R dR \tag{10.4}$$

Cratered Surfaces

For cratered surfaces, craters may be compactly arranged so that the interaction among craters could be significant. For the compactly-arranged cratered surface, the area filling factor of craters plays an important role in generating suction force, and is worth studying. To achieve it, a complete 3D model of the unit cell with periodic boundary conditions is required.

Also, the fluid vaporization under low pressure is worth taking into account in the numerical simulation of liquid-filled craters.

Besides, the implementation of double-chamber craters in Abaqus requires more experimental calibrations in order to fully understand the adhesion mechanism of double-chamber craters.

References

[1] Li, J., Celiz, A., Yang, J., Yang, Q., Wamala, I., Whyte, W., Seo, B., Vasilyev, N., Vlassak, J., and Suo, Z., 2017, "Tough adhesives for diverse wet surfaces," Science, 357(6349), pp. 378-381.

[2] Jin, L., Chen, D., Hayward, R. C., and Suo, Z., 2014, "Creases on the interface between two soft materials," Soft Matter, 10(2), pp. 303-311.

[3] Kim, D.-H., Lu, N., Ma, R., Kim, Y.-S., Kim, R.-H., Wang, S., Wu, J., Won, S. M., Tao, H., and Islam, A., 2011, "Epidermal electronics," science, 333(6044), pp. 838-843.

[4] Kabiri Ameri, S., Ho, R., Jang, H., Tao, L., Wang, Y., Wang, L., Schnyer, D. M., Akinwande, D., and Lu, N., 2017, "Graphene electronic tattoo sensors," ACS nano, 11(8), pp. 7634-7641.

[5] Yang, S., Chen, Y. C., Nicolini, L., Pasupathy, P., Sacks, J., Su, B., Yang, R., Sanchez, D., Chang, Y. F., and Wang, P., 2015, " “Cut‐and‐Paste” Manufacture of Multiparametric Epidermal Sensor Systems," Advanced Materials, 27(41), pp. 6423-6430.

[6] Viventi, J., Kim, D.-H., Vigeland, L., Frechette, E. S., Blanco, J. A., Kim, Y.-S., Avrin, A. E., Tiruvadi, V. R., Hwang, S.-W., and Vanleer, A. C., 2011, "Flexible, foldable, actively multiplexed, high-density electrode array for mapping brain activity in vivo," Nature neuroscience, 14(12), p. 1599.

[7] Wang, Y., Qiu, Y., Ameri, S. K., Jang, H., Dai, Z., Huang, Y., and Lu, N., 2018, "Low-cost, μm-thick, tape-free electronic tattoo sensors with minimized motion and sweat artifacts," npj Flexible Electronics, 2(1), p. 6.

[8] Son, D., Lee, J., Qiao, S., Ghaffari, R., Kim, J., Lee, J. E., Song, C., Kim, S. J., Lee, D. J., and Jun, S. W., 2014, "Multifunctional wearable devices for diagnosis and therapy of movement disorders," Nature Nanotechnology, 9(5), pp. 397-404.

[9] Choi, M. K., Park, O. K., Choi, C., Qiao, S., Ghaffari, R., Kim, J., Lee, D. J., Kim, M., Hyun, W., Kim, S. J., Hwang, H. J., Kwon, S.-H., Hyeon, T., Lu, N., and Kim, D.-H., 2016, "Cephalopod-Inspired Miniaturized Suction Cups for Smart Medical Skin," Advanced Healthcare Materials, 5(1), pp. 80-87.

[10] Park, J., Choi, S., Janardhan, A. H., Lee, S.-Y., Raut, S., Soares, J., Shin, K., Yang, S., Lee, C., and Kang, K.-W., 2016, "Electromechanical cardioplasty using a wrapped elasto-conductive epicardial mesh," Science translational medicine, 8(344), pp. 344ra386-344ra386.

[11] Choi, C., Choi, M. K., Liu, S., Kim, M. S., Park, O. K., Im, C., Kim, J., Qin, X., Lee, G. J., and Cho, K. W., 2017, "Human eye-inspired soft optoelectronic device using high-density MoS 2-graphene curved image sensor array," Nature communications, 8(1), p. 1664.

[12] Kim, D.-H., Lu, N., Huang, Y., and Rogers, J. A., 2012, "Materials for stretchable electronics in bioinspired and biointegrated devices," MRS bulletin, 37(3), pp. 226-235.

[13] Kim, D.-H., Ghaffari, R., Lu, N., Wang, S., Lee, S. P., Keum, H., D’Angelo, R., Klinker, L., Su, Y., and Lu, C., 2012, "Electronic sensor and actuator webs for large-area complex geometry cardiac mapping and therapy," Proceedings of the National Academy of Sciences, 109(49), pp. 19910-19915.

[14] Yeo, W. H., Kim, Y. S., Lee, J., Ameen, A., Shi, L., Li, M., Wang, S., Ma, R., Jin, S. H., and Kang, Z., 2013, "Multifunctional epidermal electronics printed directly onto the skin," Advanced Materials, 25(20), pp. 2773-2778.

[15] Jeong, J. W., Yeo, W. H., Akhtar, A., Norton, J. J., Kwack, Y. J., Li, S., Jung, S. Y., Su, Y., Lee, W., and Xia, J., 2013, "Materials and Optimized Designs for Human‐Machine Interfaces Via Epidermal Electronics," Advanced Materials, 25(47), pp. 6839-6846.

[16] Choi, S., Park, J., Hyun, W., Kim, J., Kim, J., Lee, Y. B., Song, C., Hwang, H. J., Kim, J. H., and Hyeon, T., 2015, "Stretchable heater using ligand-exchanged silver nanowire nanocomposite for wearable articular thermotherapy," ACS nano, 9(6), pp. 6626-6633.

[17] Hong, S., Lee, H., Lee, J., Kwon, J., Han, S., Suh, Y. D., Cho, H., Shin, J., Yeo, J., and Ko, S. H., 2015, "Highly stretchable and transparent metal nanowire heater for wearable electronics applications," Advanced materials, 27(32), pp. 4744-4751.

[18] Bandodkar, A. J., Molinnus, D., Mirza, O., Guinovart, T., Windmiller, J. R., Valdés-Ramírez, G., Andrade, F. J., Schöning, M. J., and Wang, J., 2014, "Epidermal tattoo potentiometric sodium sensors with wireless signal transduction for continuous non-invasive sweat monitoring," Biosensors and bioelectronics, 54, pp. 603-609.

[19] Huang, X., Liu, Y., Chen, K., Shin, W. J., Lu, C. J., Kong, G. W., Patnaik, D., Lee, S. H., Cortes, J. F., and Rogers, J. A., 2014, "Stretchable, wireless sensors and functional substrates for epidermal characterization of sweat," Small, 10(15), pp. 3083-3090.

[20] Qiao, S., Gratadour, J.-B., Wang, L., and Lu, N., 2015, "Conformability of a thin elastic membrane laminated on a rigid substrate with corrugated surface," IEEE Transactions on Components, Packaging and Manufacturing Technology, 5(9), pp. 1237-1243.

[21] Wang, L., and Lu, N., 2016, "Conformability of a thin elastic membrane laminated on a soft substrate with slightly wavy surface," Journal of Applied Mechanics, 83(4), p. 041007.

[22] Wang, L., Qiao, S., Ameri, S. K., Jeong, H., and Lu, N., 2017, "A Thin Elastic Membrane Conformed to a Soft and Rough Substrate Subjected to Stretching/Compression," Journal of Applied Mechanics, 84(11), p. 111003.

[23] Wang, S., Li, M., Wu, J., Kim, D.-H., Lu, N., Su, Y., Kang, Z., Huang, Y., and Rogers, J. A., 2012, "Mechanics of epidermal electronics," Journal of Applied Mechanics, 79(3), p. 031022.

[24] Qiao, S., Wang, L., Jeong, H., Rodin, G. J., and Lu, N., 2017, "Suction effects in cratered surfaces," Journal of The Royal Society Interface, 14(135), p. 20170377.

[25] Baik, S., Park, Y., Lee, T.-J., Bhang, S. H., and Pang, C., 2017, "A wet-tolerant adhesive patch inspired by protuberances in suction cups of octopi," Nature, 546(7658), pp. 396-400.

[26] Won, S. M., Kim, H.-S., Lu, N., Kim, D.-G., Del Solar, C., Duenas, T., Ameen, A., and Rogers, J. A., 2011, "Piezoresistive strain sensors and multiplexed arrays using assemblies of single-crystalline silicon nanoribbons on plastic substrates," IEEE Transactions on Electron Devices, 58(11), pp. 4074-4078.

[27] Mei, H., 2011, "Fracture and delamination of elastic thin films on compliant substrates: modeling and simulations."

[28] Evans, A., and Hutchinson, J., 1984, "On the mechanics of delamination and spalling in compressed films," International Journal of Solids and Structures, 20(5), pp. 455-466.

[29] Gioia, G., and Ortiz, M., 1997, "Delamination of compressed thin films," Advances in applied mechanics, 33(08), pp. 119-192.

[30] Dannenberg, H., 1958, "Measurement of adhesion by a blister method," Journal of Polymer Science Part A: Polymer Chemistry, 33(126), pp. 509-510.

[31] Jensen, H. M., 1991, "The blister test for interface toughness measurement," Engineering Fracture Mechanics, 40(3), pp. 475-486.

[32] Wan, K.-T., 1999, "Fracture mechanics of a shaft-loaded blister test–transition from a bending plate to a stretching membrane," The Journal of Adhesion, 70(3-4), pp. 209-219.

[33] Allen, M. G., and Senturia, S. D., 1988, "Analysis of critical debonding pressures of stressed thin films in the blister test," The Journal of Adhesion, 25(4), pp. 303-315.

[34] Gent, A., and Lewandowski, L., 1987, "Blow ‐ off pressures for adhering layers," Journal of Applied Polymer Science, 33(5), pp. 1567-1577.

[35] Hohlfelder, R., Luo, H., Vlassak, J., Chidsey, C. D., and Nix, W., 1996, "Measuring interfacial fracture toughness with the blister test," MRS Online Proceedings Library Archive, 436.

[36] Cao, Z., Tao, L., Akinwande, D., Huang, R., and Liechti, K. M., 2015, "Mixed-mode interactions between graphene and substrates by blister tests," Journal of Applied Mechanics, 82(8), p. 081008.

[37] Jensen, H. M., 1998, "Analysis of mode mixity in blister tests," International journal of fracture, 94(1), p. 79.

[38] Wagner, T. J., and Vella, D., 2013, "The 'sticky elastica': delamination blisters beyond small deformations," Soft Matter, 9(4), pp. 1025-1030.

[39] De Pascalis, R., Napoli, G., and Turzi, S. S., 2014, "Growth-induced blisters in a circular tube," Physica D: Nonlinear Phenomena, 283, pp. 1-9.

[40] Lu, T., Cai, S., Wang, H., and Suo, Z., 2013, "Computational model of deformable lenses actuated by dielectric elastomers," Journal of Applied Physics, 114(10), p. 104104.

[41] Liang, X., and Cai, S., 2015, "Shape bifurcation of a spherical dielectric elastomer balloon under the actions of internal pressure and electric voltage," Journal of Applied Mechanics, 82(10), p. 101002.

[42] Xie, Y.-X., Liu, J.-C., and Fu, Y., 2016, "Bifurcation of a dielectric elastomer balloon under pressurized inflation and electric actuation," International Journal of Solids and Structures, 78, pp. 182-188.

[43] Wang, F., Yuan, C., Lu, T., and Wang, T., 2017, "Anomalous bulging behaviors of a dielectric elastomer balloon under internal pressure and electric actuation," Journal of the Mechanics and Physics of Solids, 102, pp. 1-16.

[44] Reddy, N. H., and Saxena, P., 2017, "Instabilities in the axisymmetric magnetoelastic deformation of a cylindrical membrane," International Journal of Solids and Structures.

[45] Love, A. E. H., 1888, "The small free vibrations and deformation of a thin elastic shell," Philosophical Transactions of the Royal Society of London. A, 179, pp. 491-546.

[46] Timoshenko, S. P., and Woinowsky-Krieger, S., 1959, Theory of plates and shells, McGraw-hill.
[47] Wei-Zang, C., 1947, "Large deflection of a circular clamped plate under uniform pressure."
[48] Plaut, R. H., 2014, "A generalized reissner theory for large axisymmetric deflections of circular plates," Journal of Applied Mechanics, 81(3), p. 034502.
[49] Freund, L. B., and Suresh, S., 2004, Thin film materials: stress, defect formation and surface evolution, Cambridge University Press.
[50] Foppl, A., 1909, "Vorlesungen uber technische Mechanik."
[51] Adamson, A. W., 1976, "Physical chemistry of surfaces," Physical chemistry of surfaces, John Wiley & Sons.
[52] Gelfand, I. M., and Silverman, R. A., 2000, Calculus of variations, Courier Corporation.
[53] Py, C., Reverdy, P., Doppler, L., Bico, J., Roman, B., and Baroud, C. N., 2007, "Capillary origami: spontaneous wrapping of a droplet with an elastic sheet," Physical review letters, 98(15), p. 156103.
[54] Roman, B., and Bico, J., 2010, "Elasto-capillarity: deforming an elastic structure with a liquid droplet," Journal of Physics: Condensed Matter, 22(49), p. 493101.
[55] De Langre, E., Baroud, C. N., and Reverdy, P., 2010, "Energy criteria for elasto-capillary wrapping," Journal of Fluids and Structures, 26(2), pp. 205-217.
[56] Antkowiak, A., Audoly, B., Josserand, C., Neukirch, S., and Rivetti, M., 2011, "Instant fabrication and selection of folded structures using drop impact," Proceedings of the National Academy of Sciences, 108(26), pp. 10400-10404.
[57] Chopin, J., Vella, D., and Boudaoud, A., "The liquid blister test," Proc. Proceedings of the Royal Society of London A: Mathematical, Physical and Engineering Sciences, The Royal Society, pp. 2887-2906.
[58] Huang, J., Juszkiewicz, M., De Jeu, W. H., Cerda, E., Emrick, T., Menon, N., and Russell, T. P., 2007, "Capillary wrinkling of floating thin polymer films," Science, 317(5838), pp. 650-653.
[59] Henann, D. L., and Bertoldi, K., 2014, "Modeling of elasto-capillary phenomena," Soft Matter, 10(5), pp. 709-717.
[60] Cao, Z., and Dobrynin, A. V., 2015, "Polymeric droplets on soft surfaces: from Neumann’s triangle to Young’s law," Macromolecules, 48(2), pp. 443-451.
[61] Shuttleworth, R., 1950, "The surface tension of solids," Proceedings of the physical society. Section A, 63(5), p. 444.
[62] de Gennes, P.-G., Brochard-Wyart, F., and Quere, D., 2013, Capillarity and Wetting Phenomena: Drops, Bubbles, Pearls, Waves, Springer Science & Business Media.
[63] Gurtin, M. E., and Murdoch, A. I., 1975, "A continuum theory of elastic material surfaces," Archive for Rational Mechanics and Analysis, 57(4), pp. 291-323.
[64] Steinmann, P., 2008, "On boundary potential energies in deformational and configurational mechanics," Journal of the Mechanics and Physics of Solids, 56(3), pp. 772-800.

[65] Henann, D. L., and Anand, L., 2010, "Surface tension-driven shape-recovery of micro/nanometer-scale surface features in a Pt57. 5Ni5. 3Cu14. 7P22. 5 metallic glass in the supercooled liquid region: A numerical modeling capability," Journal of the Mechanics and Physics of Solids, 58(11), pp. 1947-1962.

[66] Wang, G., and Li, Y., 2013, "Influence of surface tension on mode-I crack tip field," Engineering Fracture Mechanics, 109, pp. 290-301.

[67] Style, R. W., Jagota, A., Hui, C.-Y., and Dufresne, E. R., 2017, "Elastocapillarity: surface tension and the mechanics of soft solids," Annual Review of Condensed Matter Physics, 8, pp. 99-118.

[68] Xu, X., Jagota, A., and Hui, C.-Y., 2014, "Effects of surface tension on the adhesive contact of a rigid sphere to a compliant substrate," Soft matter, 10(26), pp. 4625-4632.

[69] Jagota, A., Argento, C., and Mazur, S., 1998, "Growth of adhesive contacts for Maxwell viscoelastic spheres," Journal of applied physics, 83(1), pp. 250-259.

[70] Saksono, P., and Perić, D., 2006, "On finite element modelling of surface tension: Variational formulation and applications–Part II: Dynamic problems," Computational Mechanics, 38(3), pp. 251-263.

[71] Jerison, E. R., Xu, Y., Wilen, L. A., and Dufresne, E. R., 2011, "Deformation of an elastic substrate by a three-phase contact line," Physical review letters, 106(18), p. 186103.

[72] Pericet-Camara, R., Auernhammer, G. K., Koynov, K., Lorenzoni, S., Raiteri, R., and Bonaccurso, E., 2009, "Solid-supported thin elastomer films deformed by microdrops," Soft Matter, 5(19), pp. 3611-3617.

[73] Style, R. W., Boltyanskiy, R., Che, Y., Wettlaufer, J., Wilen, L. A., and Dufresne, E. R., 2013, "Universal deformation of soft substrates near a contact line and the direct measurement of solid surface stresses," Physical review letters, 110(6), p. 066103.

[74] Xu, Y., Engl, W. C., Jerison, E. R., Wallenstein, K. J., Hyland, C., Wilen, L. A., and Dufresne, E. R., 2010, "Imaging in-plane and normal stresses near an interface crack using traction force microscopy," Proceedings of the National Academy of Sciences, 107(34), pp. 14964-14967.

[75] He, L., and Lim, C., 2006, "Surface Green function for a soft elastic half-space: influence of surface stress," International Journal of Solids and Structures, 43(1), pp. 132-143.

[76] Style, R. W., and Dufresne, E. R., 2012, "Static wetting on deformable substrates, from liquids to soft solids," Soft Matter, 8(27), pp. 7177-7184.

[77] Hughes, T. J., 2012, The finite element method: linear static and dynamic finite element analysis, Courier Corporation.

[78] Ooura, T., and Mori, M., 1999, "A robust double exponential formula for Fourier-type integrals," Journal of computational and applied mathematics, 112(1-2), pp. 229-241.

[79] Pu, G., and Severtson, S. J., 2011, "Dependence of wetting behavior on the thickness of highly viscoelastic films," The Journal of Physical Chemistry C, 115(38), pp. 18729-18735.

[80] Park, S. J., Weon, B. M., San Lee, J., Lee, J., Kim, J., and Je, J. H., 2014, "Visualization of asymmetric wetting ridges on soft solids with X-ray microscopy," Nature communications, 5, p. 4369.

[81] Seo, S., Lee, J., Kim, K.-S., Ko, K. H., Lee, J. H., and Lee, J., 2014, "Anisotropic adhesion of micropillars with spatula pads," ACS applied materials & interfaces, 6(3), pp. 1345-1350.

[82] Chang, W.-Y., Wu, Y., and Chung, Y.-C., 2014, "Facile fabrication of ordered nanostructures from protruding nanoballs to recessional nanosuckers via solvent treatment on covered nanosphere assembled monolayers," Nano letters, 14(3), pp. 1546-1550.

[83] Lee, H., Um, D. S., Lee, Y., Lim, S., Kim, H. j., and Ko, H., 2016, "Octopus‐Inspired Smart Adhesive Pads for Transfer Printing of Semiconducting Nanomembranes," Advanced Materials, 28(34), pp. 7457-7465.

[84] Menon, C., Murphy, M., and Sitti, M., "Gecko inspired surface climbing robots," Proc. Robotics and Biomimetics, 2004. ROBIO 2004. IEEE International Conference on, IEEE, pp. 431-436.

[85] Kim, S., Spenko, M., Trujillo, S., Heyneman, B., Santos, D., and Cutkosky, M. R., 2008, "Smooth vertical surface climbing with directional adhesion," IEEE Transactions on robotics, 24(1), pp. 65-74.

[86] Chen, Y.-C., and Yang, H., 2017, "Octopus-inspired assembly of nanosucker arrays for dry/wet adhesion," ACS nano, 11(6), pp. 5332-5338.

[87] Autumn, K., Liang, Y. A., Hsieh, S. T., Zesch, W., Chan, W. P., Kenny, T. W., Fearing, R., and Full, R. J., 2000, "Adhesive force of a single gecko foot-hair," Nature, 405(6787), pp. 681-685.

[88] Irschick, D. J., Austin, C. C., Petren, K., Fisher, R. N., Losos, J. B., and Ellers, O., 1996, "A comparative analysis of clinging ability among pad‐bearing lizards," Biological journal of the Linnean Society, 59(1), pp. 21-35.

[89] Autumn, K., Sitti, M., Liang, Y. A., Peattie, A. M., Hansen, W. R., Sponberg, S., Kenny, T. W., Fearing, R., Israelachvili, J. N., and Full, R. J., 2002, "Evidence for van der Waals adhesion in gecko setae," Proceedings of the National Academy of Sciences, 99(19), pp. 12252-12256.

[90] Arzt, E., Gorb, S., and Spolenak, R., 2003, "From micro to nano contacts in biological attachment devices," Proceedings of the National Academy of Sciences, 100(19), pp. 10603-10606.

[91] Spolenak, R., Gorb, S., Gao, H., and Arzt, E., "Effects of contact shape on the scaling of biological attachments," Proc. Proceedings of the Royal Society of London A: Mathematical, Physical and Engineering Sciences, The Royal Society, pp. 305-319.

[92] Murphy, M. P., Kim, S., and Sitti, M., 2009, "Enhanced adhesion by gecko-inspired hierarchical fibrillar adhesives," ACS applied materials & interfaces, 1(4), pp. 849-855.

[93] Jin, K., Tian, Y., Erickson, J. S., Puthoff, J., Autumn, K., and Pesika, N. S., 2012, "Design and fabrication of gecko-inspired adhesives," Langmuir, 28(13), pp. 5737-5742.

[94] Lee, H., Lee, B. P., and Messersmith, P. B., 2007, "A reversible wet/dry adhesive inspired by mussels and geckos," Nature, 448(7151), p. 338.

[95] Murphy, M. P., Aksak, B., and Sitti, M., 2009, "Gecko‐Inspired Directional and Controllable Adhesion," Small, 5(2), pp. 170-175.

[96] Mengüç, Y., Yang, S. Y., Kim, S., Rogers, J. A., and Sitti, M., 2012, "Gecko‐Inspired Controllable Adhesive Structures Applied to Micromanipulation," Advanced Functional Materials, 22(6), pp. 1246-1254.

[97] Chary, S., Tamelier, J., and Turner, K., 2013, "A microfabricated gecko-inspired controllable and reusable dry adhesive," Smart Materials and Structures, 22(2), p. 025013.

[98] Buhl, S., Greiner, C., Campo, A. d., and Arzt, E., 2009, "Humidity influence on the adhesion of biomimetic fibrillar surfaces," International Journal of Materials Research, 100(8), pp. 1119-1126.

[99] Cadirov, N., Booth, J. A., Turner, K. L., and Israelachvili, J. N., 2017, "Influence of Humidity on Grip and Release Adhesion Mechanisms for Gecko-Inspired Microfibrillar Surfaces," ACS Applied Materials & Interfaces, 9(16), pp. 14497-14505.

[100] Pesika, N. S., Zeng, H., Kristiansen, K., Zhao, B., Tian, Y., Autumn, K., and Israelachvili, J., 2009, "Gecko adhesion pad: a smart surface?," Journal of Physics: Condensed Matter, 21(46), p. 464132.

[101] del Campo, A., Greiner, C., Álvarez, I., and Arzt, E., 2007, "Patterned surfaces with pillars with controlled 3D tip geometry mimicking bioattachment devices," Advanced Materials, 19(15), pp. 1973-1977.

[102] Heepe, L., Varenberg, M., Itovich, Y., and Gorb, S. N., 2010, "Suction component in adhesion of mushroom-shaped microstructure," Journal of the Royal Society Interface, p. rsif20100420.

[103] Jeong, H. E., and Suh, K. Y., 2009, "Nanohairs and nanotubes: efficient structural elements for gecko-inspired artificial dry adhesives," Nano Today, 4(4), pp. 335-346.

[104] Gao, H., and Yao, H., 2004, "Shape insensitive optimal adhesion of nanoscale fibrillar structures," Proceedings of the National Academy of Sciences of the United States of America, 101(21), pp. 7851-7856.

[105] Gao, H., Wang, X., Yao, H., Gorb, S., and Arzt, E., 2005, "Mechanics of hierarchical adhesion structures of geckos," Mechanics of Materials, 37(2-3), pp. 275-285.

[106] Yao, H., and Gao, H., 2006, "Mechanics of robust and releasable adhesion in biology: Bottom–up designed hierarchical structures of gecko," Journal of the Mechanics and Physics of Solids, 54(6), pp. 1120-1146.

[107] Mantriota, G., and Messina, A., 2011, "Theoretical and experimental study of the performance of flat suction cups in the presence of tangential loads," Mechanism and machine theory, 46(5), pp. 607-617.

[108] Liu, J., Tanaka, K., Bao, L., and Yamaura, I., 2006, "Analytical modelling of suction cups used for window-cleaning robots," Vacuum, 80(6), pp. 593-598.

[109] Akerboom, S., Appel, J., Labonte, D., Federle, W., Sprakel, J., and Kamperman, M., 2015, "Enhanced adhesion of bioinspired nanopatterned elastomers via colloidal surface assembly," Journal of The Royal Society Interface, 12(102).

[110] Afferrante, L., Carbone, G., Demelio, G., and Pugno, N., 2013, "Adhesion of elastic thin films: double peeling of tapes versus axisymmetric peeling of membranes," Tribology Letters, 52(3), pp. 439-447.

[111] Tramacere, F., Pugno, N. M., Kuba, M. J., and Mazzolai, B., 2015, "Unveiling the morphology of the acetabulum in octopus suckers and its role in attachment," Interface focus, 5(1), p. 20140050.

[112] Tramacere, F., Beccai, L., Kuba, M., Gozzi, A., Bifone, A., and Mazzolai, B., 2013, "The morphology and adhesion mechanism of Octopus vulgaris suckers," PLoS One, 8(6), p. e65074.

[113] Lötters, J., Olthuis, W., Veltink, P., and Bergveld, P., 1997, "The mechanical properties of the rubber elastic polymer polydimethylsiloxane for sensor applications," Journal of Micromechanics and Microengineering, 7(3), p. 145.

[114] Brandrup, J., Immergut, E. H., Grulke, E. A., Abe, A., and Bloch, D. R., 1989, Polymer handbook, Wiley New York etc.

[115] Eshelby, J. D., 1957, "The Determination of the Elastic Field of an Ellipsoidal Inclusion, and Related Problems," Proceedings of the Royal Society of London. Series A. Mathematical and Physical Sciences, 241(1226), pp. 376-396.

[116] Cai, S., Bertoldi, K., Wang, H., and Suo, Z., 2010, "Osmotic collapse of a void in an elastomer: breathing, buckling and creasing," Soft Matter, 6(22), pp. 5770-5777.

[117] Hong, W., Zhao, X., and Suo, Z., 2009, "Formation of creases on the surfaces of elastomers and gels," Applied Physics Letters, 95(11), p. 111901.

[118] Yu, Y., Sanchez, D., and Lu, N., 2015, "Work of adhesion/separation between soft elastomers of different mixing ratios," Journal of Materials Research, 30(18), pp. 2702-2712.

[119] Ismail, A. F., Khulbe, K. C., and Matsuura, T., 2015, Gas Separation Membranes, Springer.

[120] Firpo, G., Angeli, E., Repetto, L., and Valbusa, U., 2015, "Permeability thickness dependence of polydimethylsiloxane (PDMS) membranes," Journal of Membrane Science, 481, pp. 1-8.

[121] Merkel, T., Bondar, V., Nagai, K., Freeman, B., and Pinnau, I., 2000, "Gas sorption, diffusion, and permeation in poly (dimethylsiloxane)," Journal of Polymer Science Part B: Polymer Physics, 38(3), pp. 415-434.

[122] Lamberti, A., Marasso, S. L., and Cocuzza, M., 2014, "PDMS membranes with tunable gas permeability for microfluidic applications," Rsc Advances, 4(106), pp. 61415-61419.

[123] D Jr, C. W., 2007, "Materials science and engineering: an introduction," John Wiley & Sons. Inc.–New York, USA.